Abrupt deglacial changes in the properties of the Atlantic Water entering the Arctic

Allegra Alexandra Liltved

Master thesis in Geology

Department of Earth Science

University of Bergen

November 2021

Abstract

The Arctic Ocean and Barents Sea are currently experiencing rapid changes, with recent reductions in sea ice being linked to increased heat transport by warm Atlantic Water (AW) flowing into the Arctic Ocean. Knowledge of past ocean-climate-sea ice variability provides a crucial reference for understanding and contextualizing these ongoing changes. The last glaciation experienced numerous abrupt perturbations in the climate-ice-ocean system that can provide important exemplars for elucidating the coupling and sensitivity of this system. The most recent event being the Younger Dryas (YD) (12 900 – 11 700 cal yr BP). Despite this, the variability of AW properties inflowing to the Arctic and their relationship to ocean circulation and sea ice during the YD remains equivocal, due to there being few high-resolution proxy records covering this interval in the northern Barents Sea and Arctic Ocean.

Here I present high resolution stable isotope records (δ^{18}O and δ^{13}C) of planktic and benthic foraminifera, for the late Bølling-Allerød, Younger Dryas and early Holocene, from a sediment core (KH18-10-14-GC-1) from the Kvitøya Trough (80.69°N, 28.95°E). Subsurface properties at this location are influenced by, and thus provide a monitor of, the Svalbard Branch of AW inflowing to the Arctic. A rapid decrease in δ^{18}O of 1.28-2‰ occurs early in the Younger Dryas (YD) at 12 500 ± 280 cal yr BP in both the planktic and benthic records and persists for approximately 500 years. This isotope anomaly indicates that a large warming (or freshening) event of as much as 5 – 8 °C influenced both the near surface and bottom water through the first part of the YD. The magnitude of this inferred AW warming is consistent with models and proxy results investigating other millennial scale stadial cold periods.

The low δ^{18}O interval is concomitant with increased local sea ice cover and a weakened Atlantic Meridional Overturning Circulation. Variations in sea ice extent during the YD may explain how these events are linked. Expanding sea ice limits AW's exposure to the atmosphere and heat (buoyancy) loss, reducing the density and formation of deep water. The subsequent decrease of sea ice and AW temperature at 12 000 cal yr BP is consistent with an increase in heat loss, suggesting deep water formation recovered through the latter portion of the YD. Thus, sea-ice, ocean-heat transport, and overturning circulation appear consistently coupled during abrupt climate change events. These natural perturbations appear different in pattern to that found for the current sea ice reduction, suggesting different underlying causes.

Acknowledgements

If I had to go three years back in time and imagine myself being involved in one of the biggest projects studying climate change in the Arctic, I would never have thought it possible. From never having seen snow before in 2018 to standing on the helipad of Kronprins Håkon under the midnight sun, I can only say that this Master's program has been an opportunity of a lifetime. I would first like to express my biggest gratitude to my main supervisor Ulysses Ninnemann for choosing me to do this exciting Master's project, suggesting me for the Paleoceanography Arctic cruise and for sharing his expertise in the field with me. It has been an honor working alongside such a high impact scientist. This Masters would also not have been possible without Nil Irvali, who has been available throughout my Masters to help me with laboratory methods, chat and provide me with very thorough feedback on my Masters. I would also like to thank Eystein Jansen for his support and very useful advice.

I am extremely grateful for all the time I got to spend in the FARLAB with the wonderful people who work there, who introduced me to the world of paleoclimate, taught me how to run the mass spectrometers and ignited my interest in the field when I originally came here to do an internship at the FARLAB in 2019. It has been a pleasure working with all of you and you have taught me so much. A good work-life balance has been essential during this Masters and for that I would like to thank my friends in Bergen who have been a family to me over the years, inspiring me and filling my life with adventure and fun. The biggest thank you goes to my parents, grandparents, and supportive friends in South Africa/around Europe for all the long lunch calls and for your unfailing support even though I am so far away. Lastly, my most enormous gratitude to Håkon Nesheim for being there for me every step of the way and assuring me that everything will always work out. Thank you for believing in me more than I believe in myself and for all the delicious dinners.

It has been the most incredible experience being a part of the Earth Science family at UiB and I am so lucky to have somehow ended up here. Although the building is not very aesthetically appealing from the outside, inside it is filled with smiles, warmth, and open doors. I am grateful for each and every person I have crossed paths with within those walls.

November 2021

Allegra Alexandra Liltved

Table of Contents

1. Introduction

This thesis was supervised by Professor Ulysses Ninnemann, Dr. Nil Irvali and Professor Eystein Jansen at the University of Bergen.

1.1 Nansen Legacy Project

This study contributes to the larger research aims of the Nansen Legacy project to understand and contextualize ongoing changes in the Barents Sea. The Nansen Legacy project is a 6-year (2018 - 2023) holistic research project uniting scientists nationally and internationally with the shared goal of investigating the past, present, and future climate and ecosystem of the Barents Sea and Arctic Basin (Husum et al., 2020). With the Arctic Ocean experiencing rapid changes, it is essential that strategic and sustainable management plans based on sound observations are put into place to cope with these changes. The Nansen Legacy Project consists of four different research foci (RF) groups investigating the physical drivers (RF1) human impacts (RF2) living Barents Sea and (RF3) and the future Barents Sea (RF4). This thesis contributes to RF1 as it elucidates the longer-term history of natural variations in water mass properties in the north-western Barents Sea and their relationship to large and abrupt changes in past climate and ocean circulation. This long-term history provides insights into the natural operation of the physical climate system necessary for 1) identification and attribution of potential anthropogenic influences, 2) understanding how the complex regional ice-ocean-atmosphere feedback mechanisms operated under dramatically different and varying climate states of the past.

1.2 Objective

The Barents Sea and Fram Strait are the gateways between the Arctic and Atlantic Ocean, where Atlantic Water (AW) is transported northward and Arctic Water southwards. Over 100 years ago Fridtjof Nansen identified the importance of the warm and salty AW on heat transport to the Arctic Ocean (Nansen, 1902 within Polyakov et al., 2017). Recent reductions in the Arctic sea ice have been linked to strengthened heat transport by AW into the Arctic

Ocean (Årthun et al., 2012). Not only is AW a transporter of heat, but it is also a major contributor to deep water formation. As it flows north AW loses heat and buoyancy until it sinks in the North Atlantic to form North Atlantic Deep Water, which is a major constituent of global ocean circulation (Lynch-Stieglitz et al., 2007). It is vital to know the history of AW inflow into the Artic Ocean to better understand the origin and consequences of the changes we are currently observing and to make more accurate predictions for the future. Numerous extreme, abrupt, global, climate events have punctuated the last glacial period (Cheng et al., 2020) which are often linked to changes in ocean circulation, (Broecker et al., 2010) the most recent being the Younger Dryas (YD). Despite its significance, there are only a few high-resolution records of water properties in the north-western Barents Sea covering the YD. The objective of this thesis is thus to reconstruct the natural variability in the properties of AW flowing into the Arctic Ocean during the last deglaciation, with a strong focus on the YD, using stable isotope analysis of oxygen and carbon (δ^{18}O and δ^{13}C).

In this thesis stable isotope analysis was performed on core KH18-10-14GC-1 obtained from northern Svalbard in the Kvitøya Trough, which is appropriately located within the northernmost reach of the West Spitsbergen Current transporting AW into the Arctic. Planktic and benthic foraminifera were picked from the interval of 400 – 550 cm of KH18-10-14GC-1, covering the last deglaciation (the late Bølling-Allerød, YD and early Holocene). This thesis aims to provide high resolution stable isotope records for both near surface and bottom water during the YD in order to constrain the variability in the properties of the upper and lower reaches of AW during this abrupt climate event. The main questions I set out to answer, in descending order of specificity, are:

1. How did the properties of AW inflow change during the last deglaciation (specifically during the YD) in northern Svalbard?
2. How is the variability of the properties of AW inflow coupled to changes in ice sheet coverage and overturning circulation during this abrupt climate event?
3. Is the large decrease in foraminiferal δ^{18}O, that has been observed in numerous foraminiferal records during the YD, a result of a melt water event or an increase in intermediate depth ocean temperatures?

In order to encompass these questions, I formed the following hypothesis: the relationship between sea-ice, ocean-heat transport and overturning circulation during the YD was similar to the relationships during abrupt climate change events (e.g., D-O events) during the last glacial period.

2. Background

The climate has been changing for as long as the history of the Earth with some of these changes being more rapid and abrupt than others. Climate models rely on accurate reconstructions of the past (paleoclimate reconstructions) as test scenarios in order to assess their ability to simulate climate states outside of the modern state that they are built and optimized for. As their ability to simulate these more different climate states, and the processes giving rise to them, improves so too does our confidence in their ability to predict the changes that will occur in the future. It is therefore important to understand the complex feedback mechanisms between the ocean, cryosphere, and climate. This thesis aims to reconstruct changes in AW inflow properties into the Arctic Ocean over a period of ~3000 years between the late B/A and the early Holocene. This is a significant period when major climate system components (ice-ocean-atmosphere) experienced large and rapid changes (Cheng et al., 2020). In order to contextualize the results of this thesis it is important to first understand how the global climate has changed on both long and short time scales, and the mechanisms involved in determining these changes.

2.1 Climate and Climate Change

Earth's climate consists of complex interactions between the atmosphere, oceans, biosphere, land surface and cryosphere. The climate is constantly changing on different time scales due to various forcings. The Quaternary, which spans the last 2.6 Ma, was a period which saw some of the greatest changes of the last 60 Ma (Bradley, 2015). Changes in the Earth's climate are a combination of changes in continental position, mountain building events, changes in the solar luminosity and the orbitally modulated distribution of this insolation, as well as changes in the greenhouse gas concentrations in the atmosphere (Bradley, 2015). Variations in Earth's orbital parameters determine the amount of radiation received at a given latitude and season, pacing the waxing and waning of continental ice sheets and thus glacial and interglacial periods (Ruddiman, 2001). The superposition of the changes in the shape of Earth's orbit (eccentricity), the tilt of Earth on its axis (obliquity) and the wobble of Earth's axis of rotation (precision), result in variability in solar radiation reaching Earth's atmosphere at a given season and location (Ruddiman, 2001). Large changes in ice sheet coverage, incoming insolation and greenhouse gases have led to cyclic cold and warm phases, called glacials and interglacials, which occur on timescales of 100 kyr (in the late Pleistocene). The Last Glacial Maximum (LGM) was the most recent, coldest period on Earth which occurred due to a combination of low incoming solar radiation (summer, high latitude) allowing the growth of large ice sheets combined with lower greenhouse gas concentrations in the atmosphere (Ruddiman, 2001). During this period global sea level was ca. 120 m lower than today (Fairbanks, 1989) and ice sheets were at a maximum, with the whole of the Barents Sea covered by a grounded ice sheet up to the shelf-break of Svalbard (Hogan et al., 2010; Ingólfsson and Landvik, 2013).

Climate change can also occur on shorter time scales punctuating these glacial-interglacial periods. These rapid changes are more significant and of greater magnitudes during glacial periods than during interglacial periods. An example of shorter scale climate change are the Dansgaard-Oeschger (D-O) oscillations, which are rapid oscillations between extremely cold periods 'stadials' and milder intervals 'interstadials' during glacial periods, where temperature can vary by 8-16°C (Ruddiman, 2001; Rahmstorf and Alley, 2002) (figure 2.1). D-O events are seen by large fluctuations in δ^{18}O and dust concentrations in ice cores from Greenland (Rasmussen and Thomsen, 2004) therefore sometimes being referred to as Greenland interstadials (GI) and Greenland stadials (GS). Stadial coolings are characterized by high abundances of polar foraminifera and Ice-rafted debris (IRD) in North Atlantic sediments, however some of these contain excessive amounts of IRD with a North American provenance and compositions of high detrital carbonate (Bond et al., 1992), called Heinrich stadials. Heinrich stadials are associated with a large fresh water supply coming from the Laurentide Ice Sheet, releasing large amounts of ice bergs into the North Atlantic leading to increased IRD, carbonate and gravel (Hemming, 2004). D-O events are hypothesized to be a result of, or at least involve, reorganization of thermohaline circulation (THC) in the North Atlantic (Broecker et al., 2010). Although no D-O events are covered in the record from this thesis, it is necessary to mention them as the mechanisms responsible for these abrupt climate changes could be similar to what occurred during the Younger Dryas; including THC changes and high latitude cooling (Boyle and Keigwin, 1987).

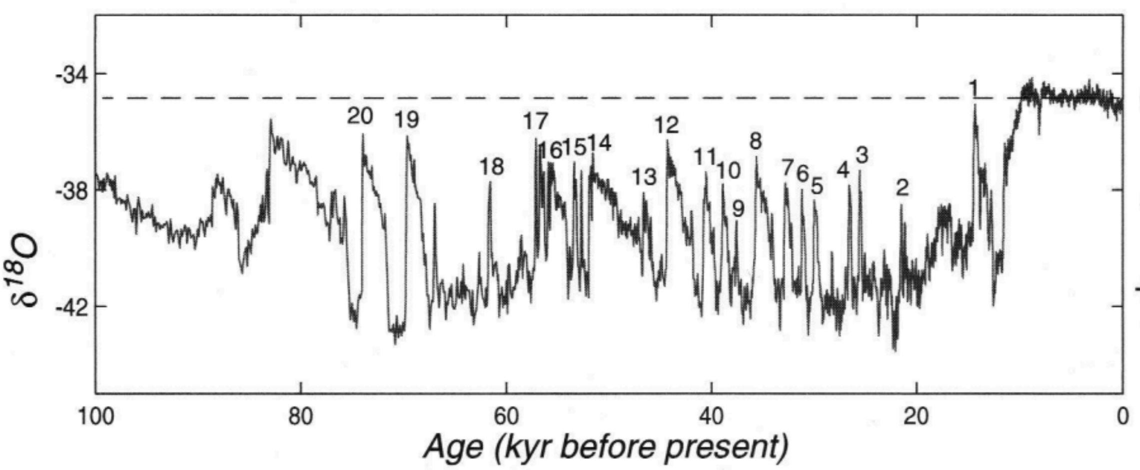

Figure 2.1 The δ^{18}O record of the Greenland Ice Core Project (GRIP) with the approximate temperature range relative to the Holocene average shown on the right. The δ^{18}O record shows low temperatures during the glacial period punctuated by D-O warming events (numbered from 1-20) and the warmer and more stable climate during the Holocene (the last 11 000 cal yr BP) (Rahmstorf and Alley, 2002).

2.2 Climate variability during the last deglaciation

This thesis will focus on millennial scale climate changes using high-resolution climate proxies during the deglaciation. During the interval between the LGM (~19 000 cal yr BP) and the early Holocene (~11 cal yr BP) there were rapid changes in all components of the climate system, as it changed from a glacial to an interglacial state. This period is known as the deglaciation. After the LGM, incoming summer solar radiation began to rise causing ice sheets to melt and triggering the deglaciation (figure 2.2). The sudden warming event evident in the Greenland Ice Sheet records and many regions of the North Atlantic and Northern Hemisphere during the late stages of the last glacial period, between ~14 700 and 12 900 cal yr BP (thousands of calendar years before AD 1950), is known as the Bølling – Allerød (B/A) (Thiagarajan et al., 2014). In the North Atlantic it is characterized by increased temperatures and decreasing sea ice (Thiagarajan et al., 2014). This rapid melting of ice and transition to warm interglacial conditions was punctuated by an abrupt return to cold conditions, called the Younger Dryas (YD).

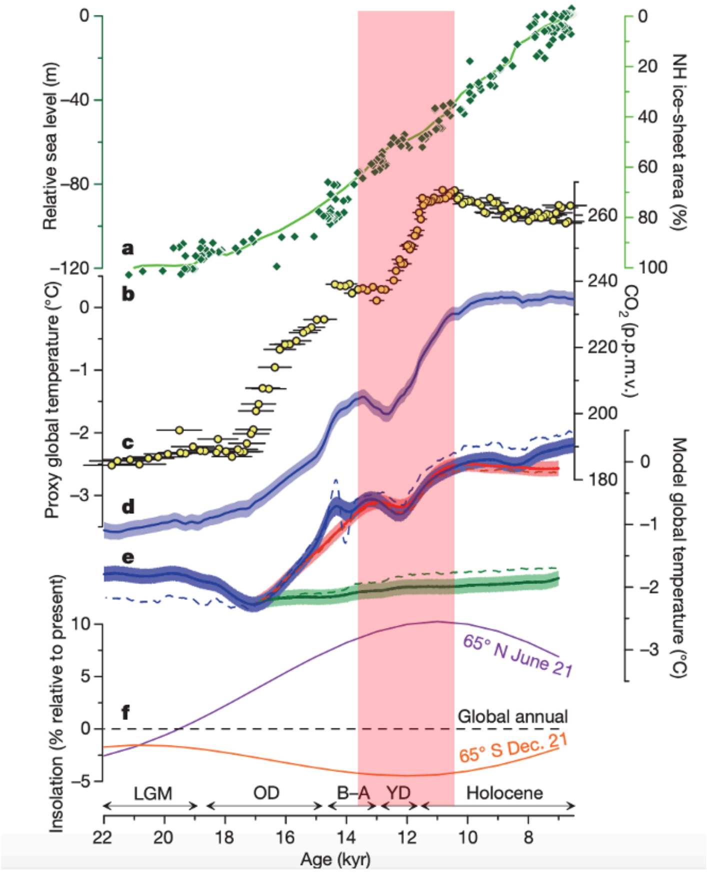

Figure 2.2 Global temperature and climate forcings since the LGM a) Relative Sea level b) Northern Hemisphere ice sheet area c) Atmospheric CO_2 concentration d) Global proxy temperature stack e) modelled global temperature stacks f) Insolation forcing at 65°N (purple) and 65°S (orange) at the local summer solstice. Error bars are 1 standard deviation. The red bar is highlighting the interval focused on in this thesis (Shakun et al., 2012 and references therein).

Younger Dryas

The Younger Dryas (YD) was a period with a return to cold conditions during the deglaciation, between 12 900 and 11 700 cal yr BP, named after the *Dryas octopetala* flower first described by Hartz in 1912 (Hartz, 1912 in Mangerud, 2021). This is a highly studied and significant period as it demonstrates that climate is capable of large and abrupt changes over short intervals (Ruddiman, 2001). A number of possible causes have been suggested for the YD (Broecker et al., 2010) including an extraterrestrial impact (Firestone et al., 2007) and/or a combination of weakened AMOC with anomalous atmospheric circulation and radiative cooling due to increase dust load, and/or decreased CH_4 and NO in the atmosphere (Renssen et al., 2015). It is suggested that the YD can be attributed to a change in Atlantic Meridional Overturning Circulation (AMOC) (subchapter 2.3) due to a freshwater event, but there is still no consensus as to the trigger and termination of this brief event (Bakke et al., 2009; Pearce et al., 2013; Cheng et al., 2020). Many papers discuss the YD being a result of a large freshwater release from Lake Agassiz, which capped the North Atlantic, thus reducing convection and deep water formation (Broecker et al., 2010). The freshwater could have forced reduction of AMOC leading to a decrease in northward heat transport and thus resulting in a cooling event. According to Broecker et al. (2010) this theory has lost favor due to a lack of geomorphic evidence for a path of the flood water.

The YD terminated abruptly approximately 11 700 cal yr BP. The trigger for this termination remains unknown but it has been proposed that it was initiated in the southern hemisphere or tropics, with proxy evidence of the termination in the south leading the northern hemisphere (Cheng et al., 2020). Proxy studies from the North Atlantic have shown that there was destabilization and loss of strength in the cold reversal towards the late YD leading to a breakup of sea ice and changing of wind patterns, eventually resulting in the final shift to the stadial state (Bakke et al., 2009). Towards the end of the YD there was a rapid increase in AMOC, increasing heat transport and causing temperatures to rise (Pearce et al., 2013).

A better understanding of the feedback mechanisms and the effects of this rapid cooling event are needed in order to understand abrupt climate changes. It has been shown that the YD first occurred in the Northern Hemisphere but propagated rapidly southward to Antarctica, with a lag time of approximately 100 years (Cheng et al., 2020). The global influence of the YD further emphases the significance of abrupt climate events. It has recently been proposed that the B/A – YD is no different than a regular D-O event and thus the processes used to explain this climate event could also be useful for understanding the origin of the D-O events (Mangerud, 2021).

Holocene

After the brief return to cold conditions during the YD the Holocene began ~11 700 cal yr BP. Our current geological epoch, the Holocene, marked the start of the interglacial period. As is usually the case with interglacials, the Holocene has displayed relatively ‘muted’ temperature fluctuations in comparison to the last glacial period. This epoch is however very important to study as it has had the most similar conditions to those we have today and is therefore important for testing climatological models. Summer insolation reached a maximum approximately at 10 000 cal yr BP called the Holocene Thermal Maximum (HTM) , and by 7 000 cal yr BP CO_2 levels and sea ice coverage were close to full interglacial levels

(Ruddiman, 2001). After the HTM, the gradually declining incoming summer insolation was the main factor controlling the climate, leading to a gradual cooling trend (Ruddiman, 2001; Wanner et al., 2015) . This cooling trend has been overprinted with multi-decadal to century-scale cold periods which are likely a result of meltwater reducing overturning circulation, as well as volcanic and solar forcing in the later Holocene (Wanner et al., 2015).

2.3 Thermohaline circulation

The oceans are a major transporter of heat around the globe and a vital redistributor of heat. In the Atlantic Ocean high latitude cooling results in the sinking of surface water to form the North Atlantic Deep Water (NADW) which travels at great depths to the Southern Ocean (Rahmstorf, 2006). Thermohaline circulation (THC) is a physical concept of the mixing of the heat and salt in the ocean, which is driven by fluxes of heat and freshwater across the surface layers of the ocean (Rahmstorf, 2006) (figure 2.3). Another term which is often used to describe large scale ocean circulation is the Atlantic Meridional Overturning Circulation (AMOC) and is often used interchangeably with THC. Although both are used to describe specific aspects of deep ocean circulation, they are not completely interchangeable. According to Rahmstorf et al. (2006) AMOC is the wind-driven north-south flow of water as a function of latitude and depth and should only be used to describe a meridional flow field, for example the total volume flux (in Sverdrups) of the N-S overturning cell in a model. THC on the other hand defines the buoyancy (temperature and salinity) related driving mechanism behind this circulation (Kuhlbrodt et al., 2007). In this thesis since both the north-south flow (AMOC) and buoyancy related driving mechanisms for deep circulation (THC) are discussed, the terms AMOC and THC will both be used.

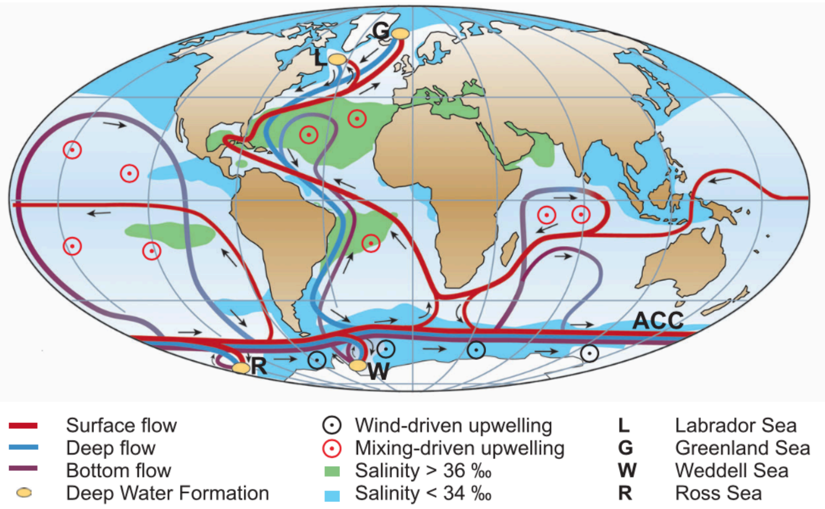

Figure 2.3 A simplified schematic representation of global thermohaline circulation. What is thought to be the deep water formation sites are shown in yellow. Surface currents are shown in red, the flow of deep waters in light blue and bottom waters in dark blue (Rahmstorf, 2006).

Thermohaline circulation consists of various components resulting in deep global oceanic overturning including cooling of water (buoyancy loss) in the northern high latitudes forming deep water, spreading of deep waters, and upwelling in the ocean interior (Talley, 2013) and return to the surface by upwelling and buoyancy gain (warming/freshening) in the Antarctic circumpolar region (Rahmstorf, 2006; Kuhlbrodt et al., 2007). In the subtropics of the North Atlantic, surface AW becomes salty due to high evaporation. This salty water is transported northward by the Gulf Stream losing heat along the way. The AW therefore becomes dense and sinks below the surface water masses to form NADW which moves southward (Ruddiman, 2001). NADW in the modern day Atlantic Ocean can be seen as a tongue of low nutrient, high δ^{13}C (explained in subchapter 4.3.2) water which extends all the way to the southern ocean (Lynch-Stieglitz et al., 2007) (figure 2.4). In the Southern Ocean, Antarctic Bottom Water and Antarctic Intermediate Water form, which have high nutrient and low δ^{13}C and have only been in contact with the atmosphere for a short period of time (Yu et al., 2008). Strong westerly winds in the Southern Ocean play an important role in THC by inducing Ekman transport and thus upwelling, bringing dense abyssal water to the surface where insolation and precipitation increase its buoyancy (Kuhlbrodt et al., 2007).

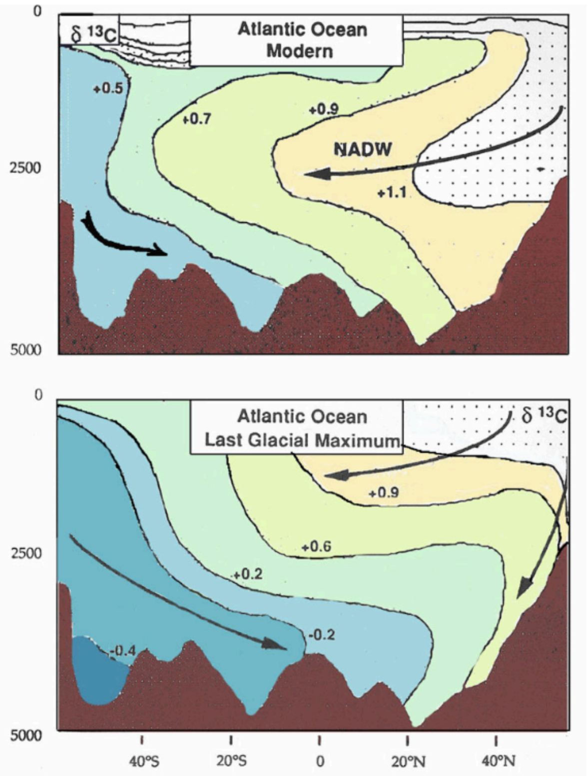

Figure 2.4 The distribution of δ^{13}C in the modern western Atlantic Ocean (top) versus during the LGM (bottom). During the LGM, NADW is shallower and southern sourced water occupies the deep North Atlantic (Rahmstorf, 2006).

There is often a strong emphasis on the fact that deep convection in the North Atlantic occurs in a few localized regions such as the Greenland-Norwegian Sea, and the Labrador and Irminger Seas (Ruddiman, 2001; Rahmstorf, 2006). While these regions are certainly important for water mass conversion and ventilation of the interior, it is important to remember that the major site of dense water formation (buoyancy loss) is in the northward flowing Norwegian Atlantic Current (Mauritzen, 1996; Furevik et al., 2007) with particularly strong heat loss as it extends northward at the surface all the way until the Fram Strait/Barents Sea (Zhang and Thomas, 2021). The northern terminus for deep water formation is therefore in fact not the Nordic Seas, or more generally "convection sites", but the Arctic Ocean where AW subducts under the sea ice and its related halocline air-sea interactions are terminated. Consistent with this circulation scheme, Zhang and Thomas (2021) have shown that a reduction in open ocean deep convection in the Labrador or Greenland Seas would thus not have a large effect on the strength of AMOC.

Changes in AMOC are closely linked to changes in the climate. Various proxies are used to estimate the strength of AMOC in the past including radiocarbon (^{14}C), grainsize and

^{231}Pa/^{230}Th. Radiocarbon ages of marine material are affected by the reservoir age, which is the offset between the radiocarbon content of the ocean and the atmosphere (subchapter 5.1.1). Reservoir ages are affected by ocean-atmosphere mixing (Stern and Lisiecki, 2013) e.g., a higher reservoir age can be due to decreased ventilation. High latitude North Atlantic radiocarbon reservoir ages can thus be used as a proxy for AMOC strength e.g., the current reservoir ages of the North Atlantic (400 – 500 ^{14}C yr) indicate strong AMOC whereas significantly higher reservoir ages can represent weakened AMOC and a southward shift of the Polar Front, due to these factors both increasing the influence of old polar waters (Stern and Lisiecki, 2013). Pa/Th is also a proxy of AMOC strength with higher values indicating reduced transport/export of deep water in/from the Atlantic and thus weaker AMOC (McManus, 2004; Ng et al., 2018). Reservoir ages and Pa/Th ratios are therefore useful proxies for reconstructing past changes in AMOC.

Three major modes of thermohaline circulation for the Quaternary period have been suggested based on proxy data and models: a ‘warm mode’ similar to the modern Atlantic, a ‘cold mode’ where NADW is at shallower depths, and a mode were NADW formation is ‘switched-off’ (Rahmstorf, 2006; Böhm et al., 2015) (figure 2.5). During the ‘warm mode’ there is deep ventilation of NADW while during the ‘switched-off mode’ NADW formation is close to shut down and water from the south dominates (Böhm et al., 2015). δ^{13}C values from benthic foraminifera indicate that NADW shoaled during the LGM in the North Atlantic (often referred to as Glacial North Atlantic Intermediate Water (GNAIW)) and was replaced by a water mass with higher nutrient contents for the Southern Atlantic called Antarctic Bottom Water (AABW) (Curry and Oppo, 2005; Lynch-Stieglitz et al., 2007) (figure 2.4). The shallower location of the GNAIW was interpreted to be a result of a different deep water formation mechanism in the North Atlantic (Curry and Oppo, 2005). Although AMOC was not the same structure or strength during the LGM as it is today, according to Lynch-Stieglitz et al. (2007) it was not completely sluggish.

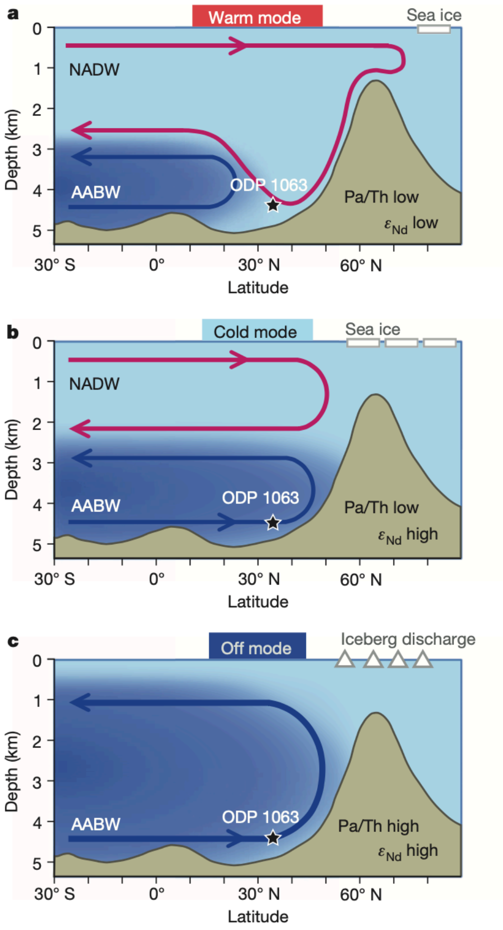

Figure 2.5 The three conceptual modes of AMOC during the last glacial period. a) The ‘warm mode’ b) the ‘cold mode’ and c) the ‘off mode’. ODP 1063 is a core from the Böhm et al. (2015) paper. The red arrow represents the flow of NADW and the blue arrow represents AABW (Böhm et al., 2015).

Abrupt climate variations are thought to be connected to changes in THC which regulate the heat transport from the tropics to the high latitudes (Pearce et al., 2013). THC has often also shut down during abrupt climate events due to major inputs of freshwater from melt water or ice sheets e.g., during Heinrich Events and perhaps also the YD (Rahmstorf, 2006). Proxy data has provided evidence that during Heinrich events there was a shutdown of AMOC, ‘off mode’, due to large fresh water forcing during these periods (Rahmstorf, 2006; Böhm et al., 2015). It is argued by Böhm et al. (2015) that only for Heinrich events close to glacial maxima was the ‘shut off’ mode reached and that AMOC weakened during the YD but did not shut down completely. D-O events are likely to be a result of shifts between the ‘warm’ and ‘cold modes’ of THC (Rahmstorf, 2006). The ocean changes during abrupt climate events are also likely to be strongly affected by ice cover and the thickness of the halocline in Nordic Seas. An increase in both sea ice cover and halocline thickness reduces convection (Sessford et al., 2019) and acts as a barrier for heat loss of the inflowing AW during stadial periods (Rasmussen and Thomsen, 2004; Dokken et al., 2013). It has been hypothesized that increased ice coverage and a thick halocline during stadial periods resulted in insulation of intermediate AW, increased intermediate ocean temperatures, and therefore could have impacted deep water formation (Ezat et al., 2014). It is thus known that the strength of AMOC is highly sensitive to changes in sea ice and freshwater inputs. AMOC has a direct impact on global heat transport as well as the deep ocean CO_2 storage and therefore a change in this deep ocean circulation would have a significant effect on the global climate (Kuhlbrodt et al., 2007).

2.4 Past and future ocean circulation changes

During the Holocene there has been active deep water formation with NADW occupying a depth of down to 5000 m in the Atlantic known as the 'warm mode' (Böhm et al., 2015). However, the abrupt climate shifts in the past have demonstrated how sensitive the Arctic Ocean is to freshwater inputs. The recent ice retreat in the Arctic is concurrent with an increased heat transport from AW inflow, referred to as 'Atlantification' of the Arctic (Årthun et al., 2012). A model for the Barents Sea shows that future increases in AW heat transport are a result of warmer AW but not necessarily increased current strength (Årthun et al., 2019). Warming of the high northern latitudes is likely to result in increased sea surface temperatures and freshwater events which could potentially lead to a shift in modes of deep water formation and thus thermohaline circulation. It is *very likely* that AMOC will weaken during the 21st century by between 11% and 34% (Pachauri et al., 2014). Models have predicted that a shutdown of THC would lead to cooling of the Northern Hemisphere and warming of the Southern Hemisphere due to decreased heat transport to the North Atlantic (Rahmstorf, 2006). The cooling of salty AW flowing through the Fram Strait into the Arctic Ocean is a major constituent of NADW formation (Mauritzen, 1996; Furevik et al., 2007), and thus the strength of AMOC (Falardeau et al., 2018), making its past variability of utmost importance for future climate predictions.

Despite its importance, a limited number of paleo-oceanographic studies investigating AW property changes have been done on the last deglacial period using sediment cores from northern Svalbard (Ślubowska et al., 2005; Ślubowska-Woldengen et al., 2007; Chauhan et al., 2016) and in particular the Kvitøya Trough (Kristensen et al., 2013; Ivanova et al., 2019). Additionally, high dissolution of $CaCO_3$ in these locations means that not many high resolution, well-dated records exist (Ivanova et al., 2019). It is generally agreed that following the disintegration of the Barents Sea Ice Sheet (BSIS) there was an increase in subsurface AW inflow marking the onset of the B/A (Ślubowska et al., 2005; Ivanova et al., 2008) or even as early as 15 500 cal yr BP (Chauhan et al., 2016). This increase in AW flow is mainly supported by high *C. neoteretis* abundances (Kristensen et al., 2013; Ivanova et al., 2019) in cores in the Kvitøya Trough as well as cores from a parallel trough called the Hinlopen Strait (Ślubowska et al., 2005). Thereafter the AW inflow gradually decreased up until the YD (Kristensen et al., 2013). There is discrepancy as to how AW inflow/properties via the Fram Strait varied during the last abrupt climate event of the deglaciation – the YD. A few studies done in close proximity to the Kvitøya Trough suggest a diminished AW inflow during the YD due to the absence of planktic foraminifera (Kristensen et al., 2013) and low abundance of *C. neoteretis* (Ślubowska et al., 2005). In contrast, Ivanova et al. (2008) concluded that there was increased AW inflow during the YD in the Kvitøya Trough, supported by foraminiferal assemblages and a decrease in δ^{18}O values (interpreted to be due to melt water at the surface) (Ivanova et al., 2008; Chauhan et al., 2016).

Low benthic and planktic δ^{18}O values have been found during the YD stadial, generally being attributed to a freshwater event during this period (Chauhan et al., 2016; Ivanova et al., 2019) and sinking of low δ^{18}O brines (Dokken and Jansen, 1999). Although it has been speculated for over 20 years that decreases in benthic δ^{18}O values during stadial periods in the northern Barents Sea and Nordic Seas could be due to increased AW temperatures due to reduced convection (Rasmussen et al., 1996; Rasmussen and Thomsen, 2004; Ezat et al., 2014; Sessford et al., 2018; El bani Altuna et al., 2021), the possibility of the low δ^{18}O values during the YD being due to increased AW temperatures has not been thoroughly considered.

All in all, there is a lack of consensus as to how the properties of AW changed during the YD in north-eastern Svalbard, an important site for deep water formation. Since AW is a major heat transporter into the Arctic Ocean, it is vital to understand how its properties have varied since the deglaciation and especially during abrupt climate events - like the YD. The high resolution stable isotope δ^{18}O record from this thesis therefore plays an essential role in filling the gap of how AW properties varied through the YD, providing an analogue for other stadial periods as well as allowing for a better understanding of the relationship of AW properties to sea ice coverage and AMOC during the most recent of the large millennial scale abrupt climate events.

3. Study Area

3.1 Location and morphology

The sediment core used for this study, KH18-10-14GC-1, was obtained from the Kvitøya Trough (80.69° N, 28.95° E) at a depth of 552 m onboard RV Kronprins Håkon, in 2018. This core was obtained at Paleo Station 14 (NPAL14) which is located on the continental shelf on the side of the Kvitøya Trough (figure 3.1). This exact site location was chosen using multibeam and sub-bottom profilers to ensure continuous sedimentation with well-defined layering (Husum et al., 2020). This site is appropriately located for this study as it lies within the reach of the West Spitsbergen Current (Figure 3.4) and therefore should be sensitive to changes in advection of AW (Ślubowska-Woldengen et al., 2007). As can be seen in figure 3.2 b NPAL14 has a thick layer of Holocene sediments above glacial sediment and bedrock, making this site useful for reconstructing changes in AW inflow into the Artic since the last deglaciation.

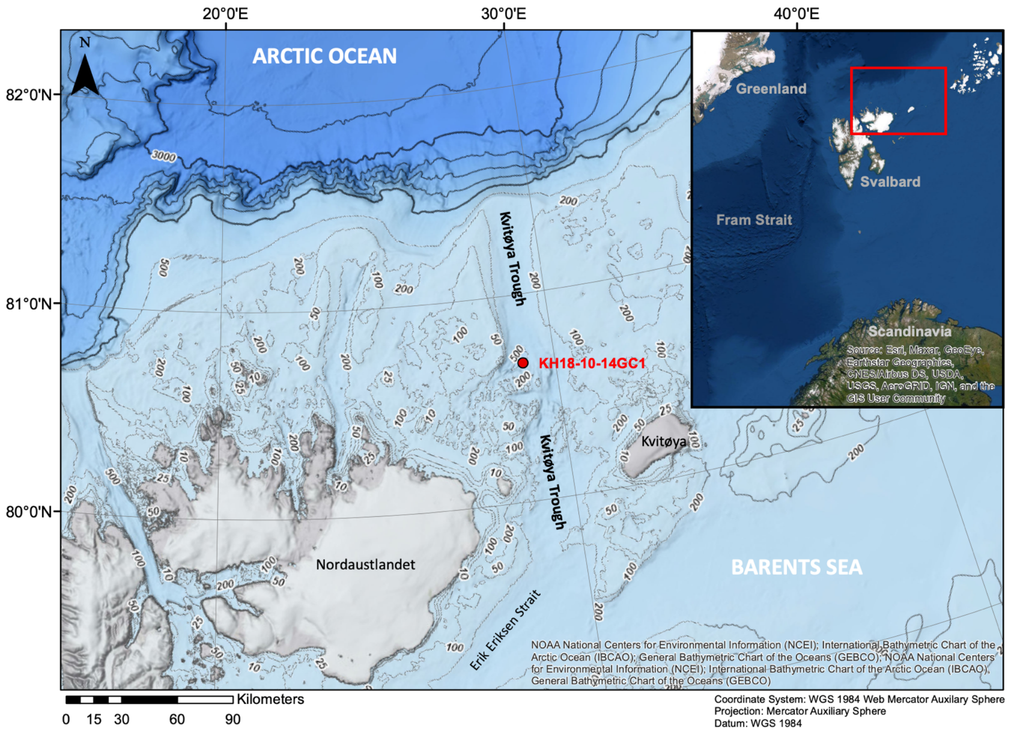

Figure 3.1 Map showing the location and bathymetry of the Kvitøya Trough and surrounding area. The location of core KH18-10-14GC-1 is indicated as a red dot. The area of the map is demarcated by the red square on the location map (left) (Map made on ArcMap by Allegra Liltved).

This chapter will discuss the bathymetry, geology, and oceanography of the Kvitøya Trough as well as the deglaciation history and paleoceanography relevant for this thesis.

3.1.1 Kvitøya Trough bathymetry

The Kvitøya Trough is located in northern Svalbard, which is an archipelago in the northwestern Barents Sea between 76°- 80°N and 10° – 33°E (Ślubowska et al., 2005) forming a boundary between the Barents Sea and the Artic Ocean (Figure 3.1). There are many troughs and fjords in Northern Svalbard as a result of the drainage of the Svalbard-Barents Sea Ice-Sheet (SBIS) that covered the Barents Sea and Svalbard during the last glaciation (Dowdeswell et al., 2010; Hogan et al., 2010; Hughes et al., 2015). The Kvitøya Trough is a U-shaped, 190 km long, <30 km wide trough running between two islands in Northern Svalbard called Nordaustlandet and Kvitøya (Hogan et al., 2010) (Figure 3.1). This trough lies at the northern margin of the Barents Sea trending in a northerly direction where it meets the shelf break leading into the Nansen Basin, a deep basin of the Artic Ocean (Hogan et al., 2010). The widest part of the trough is at the northern end where it is 30 km in width. The southern end of the trough is bounded by a small sill which cuts the trough off from the deeper Erik Erikson Strait (Hogan et al., 2010).

Bathymetric mapping and sub bottom profiling on the cruise was done using four different acoustic acquisition systems onboard Kronprins Håkon. This included two multibeam profilers EM710 and EM302 used to map the topography of the sea floor and two sub-bottom profilers, Topas PS40 and Sub-bottom profiler 300 (Husum et al., 2020). This allowed for the acquisition of a bathymetric profile attained along the ship's track as well as a 50 m deep sediment profile of site NPAL14. The Kvitøya Trough has a variable depth with the edges being between 50 – 100 m (Hogan et al., 2010) and a maximum depth in the center of 600 m (figure 3.2 A). At the bottom of the trough, ridges can be found which have been interpreted as glacial lineations that formed during the last glaciation when the Kvitøya Trough was an active ice stream (Husum et al., 2020), this will be discussed further in subchapter 3.3. The Holocene sediments covering this deformed bedrock will be the focus of this Master thesis.

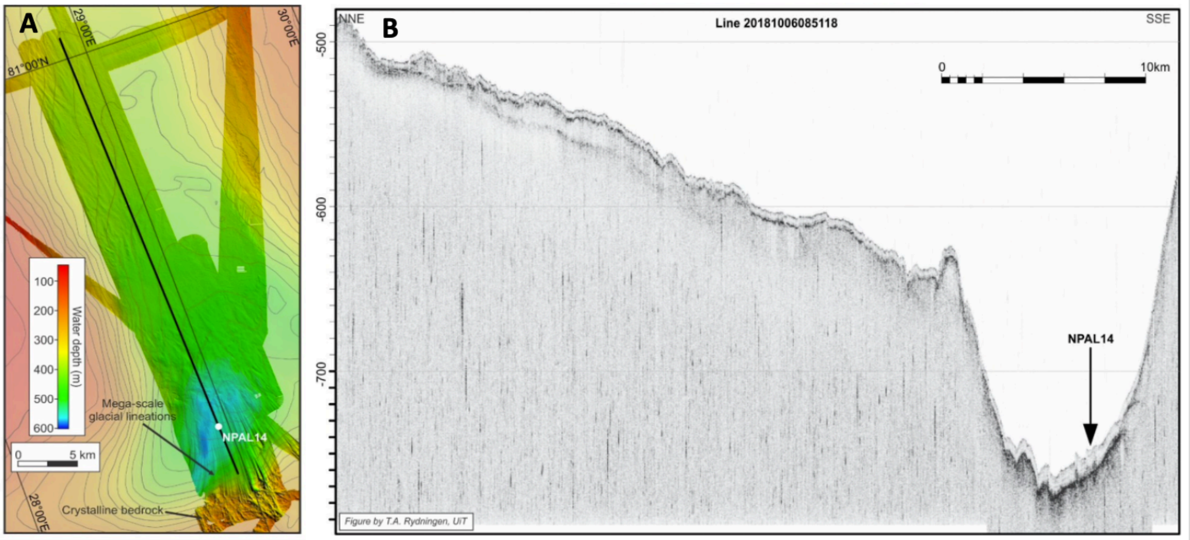

Figure 3.2 A) The multibeam bathymetry from the Kvitøya Trough. NPAL14 is shown as a white dot and glacial lineations can be seen to the south of the site B) Seismic profile of NPAL14 showing the Holocene sediments above the bedrock (Husum et al., 2020).

3.2 Geology

3.2.1 Bedrock geology

The seafloor geology of the Kvitøya Trough has not been well mapped, but the geology has been inferred by the lithology of the quaternary sediments found above the bedrock (Elverhøi and Lauritzen, 1984). Precambrian and lower Paleozoic granitic rocks known as the Hekla Hoek formation dominate the geology in Nordauslandet and Kvitøya. These older rocks extend to the south of the Kvitøya Trough where they meet younger Permian and Triassic-Lower Jurassic sandstones and limestones (Elverhøi and Lauritzen, 1984; Hogan et al., 2010).

3.2.2 Quaternary Geology

Quaternary sediments are found overlying the bedrock in the Kvitøya Trough. The two major lithofacies found in the Kvitøya Trough are massive, fine-grained mudstone and diamicton (Hogan et al., 2010; Ivanova et al., 2019). Studies from the Kvitøya Trough have hypothesized that the massive, fine-grained mud is a result of accretion of suspended sediment (Hogan et al., 2010). Hogan et al. (2010) terms the mud layer as Holocene glaciomarine sediments. Ivanova et al. (2019) identifies two separate units of mud in their cores taken from the Kvitøya Trough; the upper being hemipelagic mud deposited during the Holocene and the lower being fine grained glaciomarine sediments with occasional laminations which were deposited during the YD and B/A. Hogan et al. (2010) also found two mud sub facies both being massive muds but one having larger clasts. These hemipelagic deposits lie on top of the diamicton.

The diamicton is interpreted to be a proximal glaciomarine sediment deposited during the early deglaciation period when there was high IRD. This material has poorly sorted, angular, coarse material in a fine-grained matrix, with a high $CaCO_3$ content (Ivanova et al., 2019). According to Hogan et al. (2010) the diamicton has been highly deformed by sub-glacial processes and is interpreted to be thin sub-glacial deformation till (Hogan et al., 2010). The transition from subglacial to post-glacial sediments without deglacial deposits suggests that the ice sheet retreat was rapid and likely progressed through iceberg calving (Hogan et al., 2010). A brief deglaciation history of the northeastern Barents Sea will be given below.

3.3 Deglaciation history

During the LGM the northwestern Barents Sea was completely covered in grounded ice called the Barents Sea Ice Sheet (BSIS) (Hughes et al., 2015). The Kvitøya Trough is a result of the calving of ice streams during the deglaciation. During the late Weichselian (~20 000 cal yr BP) an ice dome was present to the west of Kong Karls Land from which many large ice streams flowed (Dowdeswell et al., 2010) (figure 3.3). The movement of ice has been inferred from the submarine landforms indicating ice flow directions in the northwestern Barents Sea (Dowdeswell et al., 2010). Streamlined landforms, meltwater channels and cavities, and iceberg scours on the floor of the Kvitøya Trough provide evidence of this form of mass loss (Hogan et al., 2010). These streamlined features are interpreted to have formed during the LGM since they only have a thin layer of post-glacial sediment covering them (Hogan et al., 2010). They provide evidence of the northwards ice flow through the Kvitøya Trough for approximately 135 km reaching at least 81°N (Hogan et al., 2010). Although ice did flow through the Kvitøya Trough, this trough is not thought to have been one of the major ice streams during the last glaciation (Dowdeswell et al., 2010).

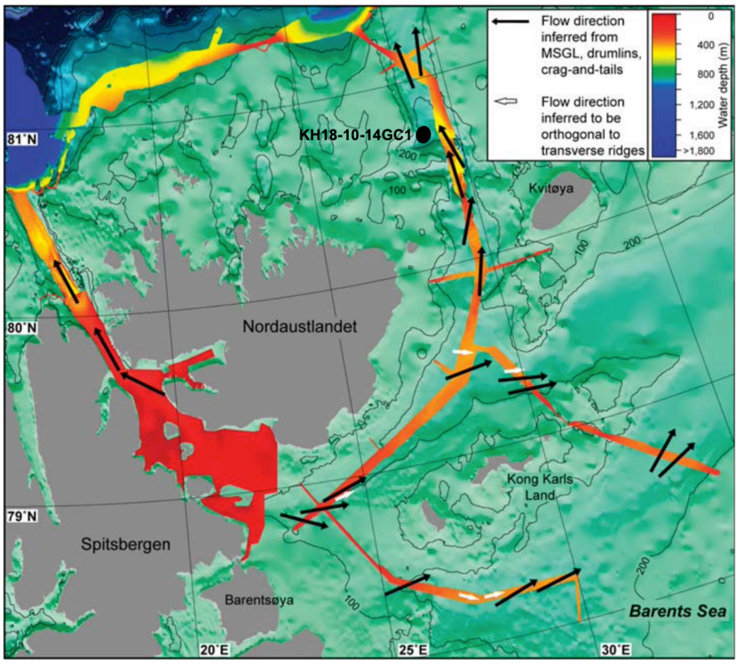

Figure 3.3 A map showing inferred ice flow direction (marked by black arrows) in eastern Svalbard and the northwestern Barents Sea. The northwards ice flow in the Kvitøya Trough has been inferred from submarine landforms such as mega scale glacial lineations (Dowdeswell et al., 2010). The location of core KH18-10-14GC-1 is marked with a black dot.

There is a debate with regards to the onset of the deglaciation in this area, with some studies suggesting the ice sheet retreat began as early as 19 000 – 18 000 cal yr BP (Hughes et al., 2015) and others suggesting a later retreat (Hogan et al., 2010). According to Chauhan et al. (2016) the deglaciation is seen as the freshening of the surface water around 18 500 cal yr BP (Chauhan et al., 2016). At 15 600 cal yr BP there was the major disintegration of the BSIS (Chauhan et al., 2016) which is clearly seen as an IRD peak at sites on the continental shelf north of the Franz Victoria Trough (Kleiber et al., 2000) and northern Svalbard margin (Chauhan et al., 2016). Although the onset of the deglaciation is debated, diamicton found in the Kvitøya trough dating 15 700 cal yr BP suggests that the onset was not later that Heinrich Stadial 1 (18 000 – 15 000 cal yr BP) (Ivanova et al., 2019).

The breaking apart of the ice sheet was fueled by geothermal activity below the ice, inflow of warm AW and sea level rise causing it to detach from the ground (Ivanova et al., 2019). Pulses in IRD show that the ice sheet disintegrated in a stepwise manner (Kleiber et al., 2000). The disintegration of the BSIS in the Kvitøya Trough is inferred to have occurred relatively rapidly between 14 000 – 13 500 cal yr BP due to the lack of landforms formed by stillstands as well as the lack of ice proximal deglacial sediments (Hogan et al., 2010). Between 16 000 cal yr BP and 14 860 cal yr BP glaciomarine sedimentation took place on the eastern shelf of Svalbard and after 14 000 cal yr BP the ice sheet had moved further to the west (Kristensen et al., 2013). During the YD, eastern Svalbard had near-perennial sea ice cover but the north and west of Svalbard had seasonal sea ice cover (Kristensen et al., 2013). The occurrence of sea-ice biomarkers in the northern Barents Sea provide evidence for seasonal sea ice during the YD until ~9.1 cal yr BP, after which sea ice concentrations start to decline (Pieńkowski et al., 2021).

3.4 Oceanography

3.4.1 Local ocean currents

The movement of warm and saline AW from the Gulf Stream into the Arctic is a very important mechanism for regulating global climate. The Fram Strait, located between Greenland and Svalbard, is the major conduit for the exchange of water and heat between the Northern Atlantic and Artic Ocean, via the Norwegian Sea (figure 3.4). This passage, being the only deep passage to the Artic Ocean (2 600 m), advects the most sensible heat into the Artic and serves as the main exit for sea ice from the Arctic (Rudels et al., 2012). AW also enters the Artic Ocean through the broad and shallow (200 - 300 m) Barents Sea (Rudels et al., 2012) passing through the Kara Sea and St. Anna Trough (Rudels, 2009).

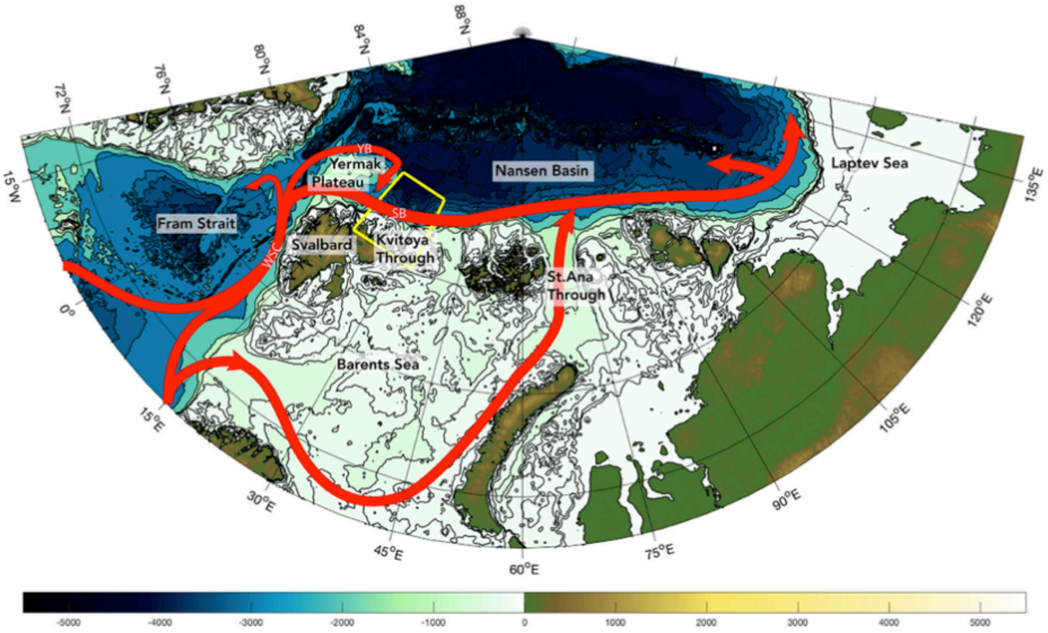

Figure 3.4 Bathymetric map showing the transport of AW by the Western Spitsbergen Current into the Arctic Ocean via the Fram Strait. The WSC splits into the Yermak Branch (YB) and the Svalbard Branch (SB) which bathes the Kvitøya Trough (indicated by the yellow block). AW inflow is indicated by red arrows. The colour bar indicates the bathymetry (Pérez-Hernández et al., 2017).

Warm, saline AW from the North Atlantic is transported to the Artic via the North Atlantic Current (NAC). This current splits into two branches south of Svalbard where one branch enters the Barents Sea via the North Cape Current and the other becomes the Western Spitsbergen Current (WSC) (figure 3.5). The WSC travels along the eastern side of the Fram Strait transporting warm and salty AW northwards (Ślubowska et al., 2005). At approximately 78°N the WSC cools and sinks below the cold, fresh, surface Polar Water to form the Intermediate Atlantic Water (Rudels et al., 2012) flowing at a depth of between 100 and 600 m, based on CTD data (Chauhan et al., 2016). At the north-western shelf break of Spitsbergen, around 80°N, the WSC splits into two branches; the Svalbard Branch (SB) and the Yermak Branch (YB). The SB flows eastward into the Artic Ocean over the Svalbard slope, circulating cyclonically, while the YB travels northward over the Yermak Plateau (Bartels et al., 2017). It has been proposed that these two branches merge again to the east of the Yermak plateau (Pérez-Hernández et al., 2017). A large portion of the western branch of AW is recirculated back to the Atlantic Ocean via the Return Atlantic Current (RAC) (Walczowski and Piechura, 2011). The East Greenland Current (EGC) flows southward on the western side of the Fram Strait (Rudels, 2009) transporting polar and arctic water from the Siberian shelves back to the North Atlantic (Chauhan et al., 2016). The EGC transports cold, low salinity water which lies above the Return Atlantic Water (RAW) (El bani Altuna et al., 2021).

The extent to which AW transported by the SB flows into the Kvitøya Trough is largely unknown, as this area has not been well studied. At the opening of the trough, the eastward flowing AW from the SB meets the shelf water coming from the west (Menze et al., 2020). Hydrographic data show that there is a surface to bottom AW flow through the Kvitøya Trough into the Barents Sea (Ivanova et al., 2008). Hydrodynamical models have also shown a strong southward flow of water on the western side of the Kvitøya Trough comprising AW and water flowing in from the eastern shelf, with a small portion of water being recirculated within the trough (Menze et al., 2020). This southward flow mainly occurs at the isobaths between 100 - 200 m. Another study, which took transects across the Kvitøya Trough found that there was only a small AW signal on the western side of the trough and that this signal was lost towards the south of the trough, due to the water losing its warm and salty signal (Pérez-Hernández et al., 2017). Pérez-Hernández et al. (2017) used velocity vectors to show that majority of the boundary current moves past the trough and only a small part of the current bends to enter the trough. They concluded that the Kvitøya Trough is not highly affected by AW inflow, but it must be kept in mind that this information is inferred from a single study and more water mass measurements need to be done in this area. The CTD cast from the Nansen Legacy Cruise in 2018 (figure 3.7) shows that AW/mAW is present in the Kvitøya Trough below 100 m in the water column.

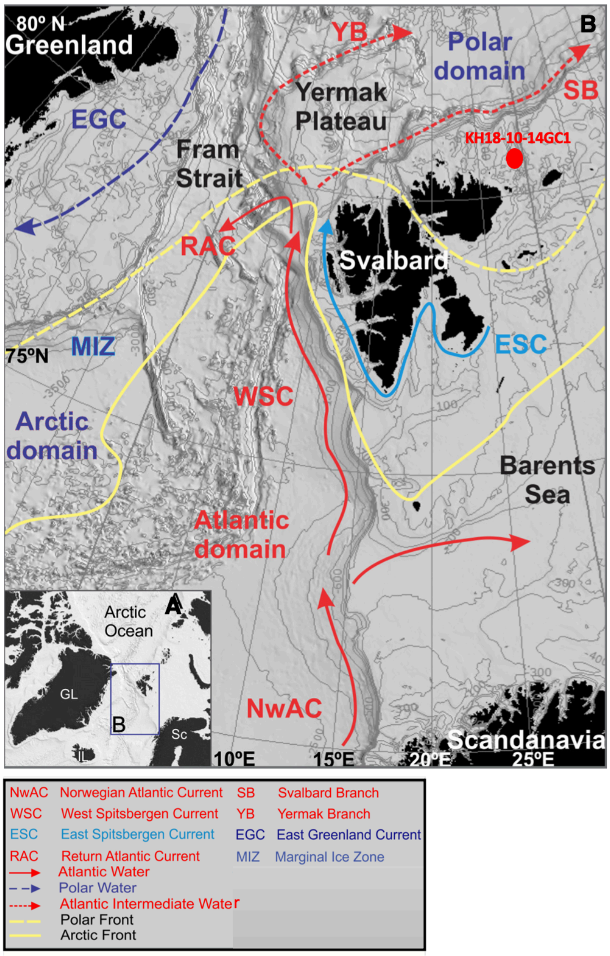

Figure 3.5 A map of the Nordic Seas and Arctic Ocean showing the main water masses, surface currents and fronts in the area. The position of core KH18-10-14GC-1 in relation to the ocean currents is shown. Modified from Chauhan et al. (2016).

It is important to consider if changes in sea level could have affected the water masses and ocean currents influencing the core location through for the interval of this thesis. On a local scale, changes in sea level are very variable but in general there was a decrease in sea level during the deglaciation, in Scandinavia, due to glacio-isostatic rebound during this period (Lohne et al., 2007; Schomacker et al., 2019). In western Norway sea level was approximately 40 m higher during the YD (Lohne et al., 2007). In Nordauslandet the marine limit was ~ 55 m a.s.l at approximately 11 500 cal yr BP (Schomacker et al., 2019). During the interval studied in this thesis sea level could therefore have been between 30-60 m higher (Schomacker et al., 2019) but this would not have had a significant impact on the water masses affecting our core site since today, as it is modified Atlantic Water filling the entire water column. If anything, a higher local sea level might have allowed AW better access to the Kvitøya Trough by deepening the opening.

Both the return flow and inflow of warm AW into the Arctic are very important factors for global THC (Walczowski and Piechura, 2011) (discussed in section 2.3). The WSC sinks to form deep water therefore being a vital component of THC. The melting of ice and transfer of heat via the NAC in the Nordic seas and Arctic effects local climate drastically (Walczowski and Piechura, 2011). It is therefore very important to understand how it has varied in the past.

3.4.2 The Polar Front

The Polar Front (PF) is a water mass boundary where Atlantic and Arctic Water meet (figure 3.5). Since the PF is a water mass boundary it is defined by SST and density. The location of the PF has not been well defined with changes in both temperature and surface salinity having an effect on its location (Barton et al., 2018). Barton et al. (2018) described the PF as a bathemetrically driven front which follows the Spitbergen Bank splitting into two branches at the Central Bank. The nothern branch devides the Arctic water masses from the Barents Sea water masses. The southern branch travels southwards along the western rise of the Central Bank and defines the boundary between cold Barents Sea Water and warmer AW. This front is a shelf slope current which follows the 220 m isobath controlled by potential vorticity constraints (Barton et al., 2018).

The movement of the PF is linked to changes in currents and water masses in the area. For example during the Younger Dryas it is hypothesised that the PF was located in close proximity to the Hinlopen Trough, while at the end of the YD it retreated northwards (Koç et al., 2002; Ślubowska et al., 2005).

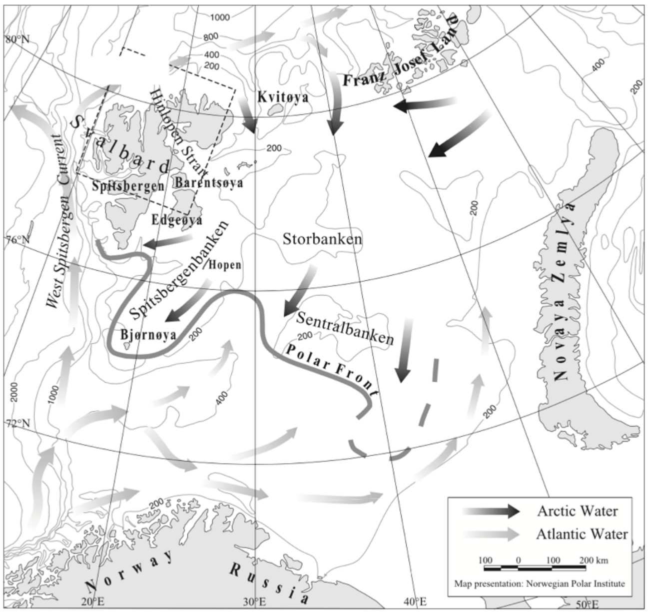

Figure 3.6 Map showing the location of the Polar Front (Koç et al., 2002)

3.4.3 Water masses

The AW flowing into the Arctic Ocean cools and becomes less salty when it meets the sea ice and melt water from the sea ice (Rudels, 2009). The Artic Ocean is highly stratified and can therefore be separated into different layers, from the surface down these include: the polar mixed layer, the halocline, the AW layer, the intermediate water below the Atlantic layer and the deep and bottom waters (Rudels, 2009). In the Artic Ocean the mixed layer is approximately 50 m thick consisting of cold, low salinity Polar Water from the Arctic and below this there is a thick halocline in which temperatures remain low but salinity changes rapidly (between 34.5 and 32) (Rudels, 2009). Some studies also mention another surface water mass which is slightly saltier and is referred to as Arctic Water (Chauhan et al., 2016) (Ślubowska-Woldengen et al., 2007). Below the halocline there is a thick layer of relatively warm, saline AW found between 100 – 600 m (Chauhan et al., 2016). AW has many different definitions in the Arctic Ocean and Barents Sea. It is sometimes defined as water with a temperature above 2°C (Chauhan et al., 2016) but has often been more broadly defined as a water mass with a temperature above 0°C (Pérez-Hernández et al., 2017). Occasionally AW is divided into subcategories including Modified AW (mAW) , which is AW that has lost some of its heat (Sundfjord et al., 2020).

Below the AW in the deep Arctic Ocean cold Intermediate Water and deep bottom waters are found. The Arctic Intermediate Water is found below the AW and typically has colder temperatures and lower salinity (Sundfjord et al., 2020). The Deep Water found in the north of the Barents Sea, below 500 m, is called Eurasian Basin Deep Water (EBDW). This is however not of much importance for our site which is situated at 552 m.

As discussed above there are many overlapping water mass definitions between the northern Barents Sea and Arctic Ocean (Chauhan et al., 2016; Sundfjord et al., 2020). New water mass definitions were defined and tabulated at the Nansen Legacy Workshop in 2020 to provide broader water mass definitions for the Nansen Legacy study area, which is mainly the Barents Sea (Sundfjord et al., 2020). For this study the new definitions are used and related back to the definitions from Chauhan et al. (2016) and Ivanova et al. (2019) (two recent studies with core locations close to NPAL14) to describe the water masses found at NPAL 14.

Table 3.1. Water mass definitions of the 6 main water masses used to describe water masses in the Barents Sea and the Arctic Ocean. In accordance with the Nansen legacy the Sundfjord et al., 2020 definitions are utilized, and previous regional definitions are included for reference. CT stands for conservative temperature, T for temperature, S for salinity and σ_0 for density.

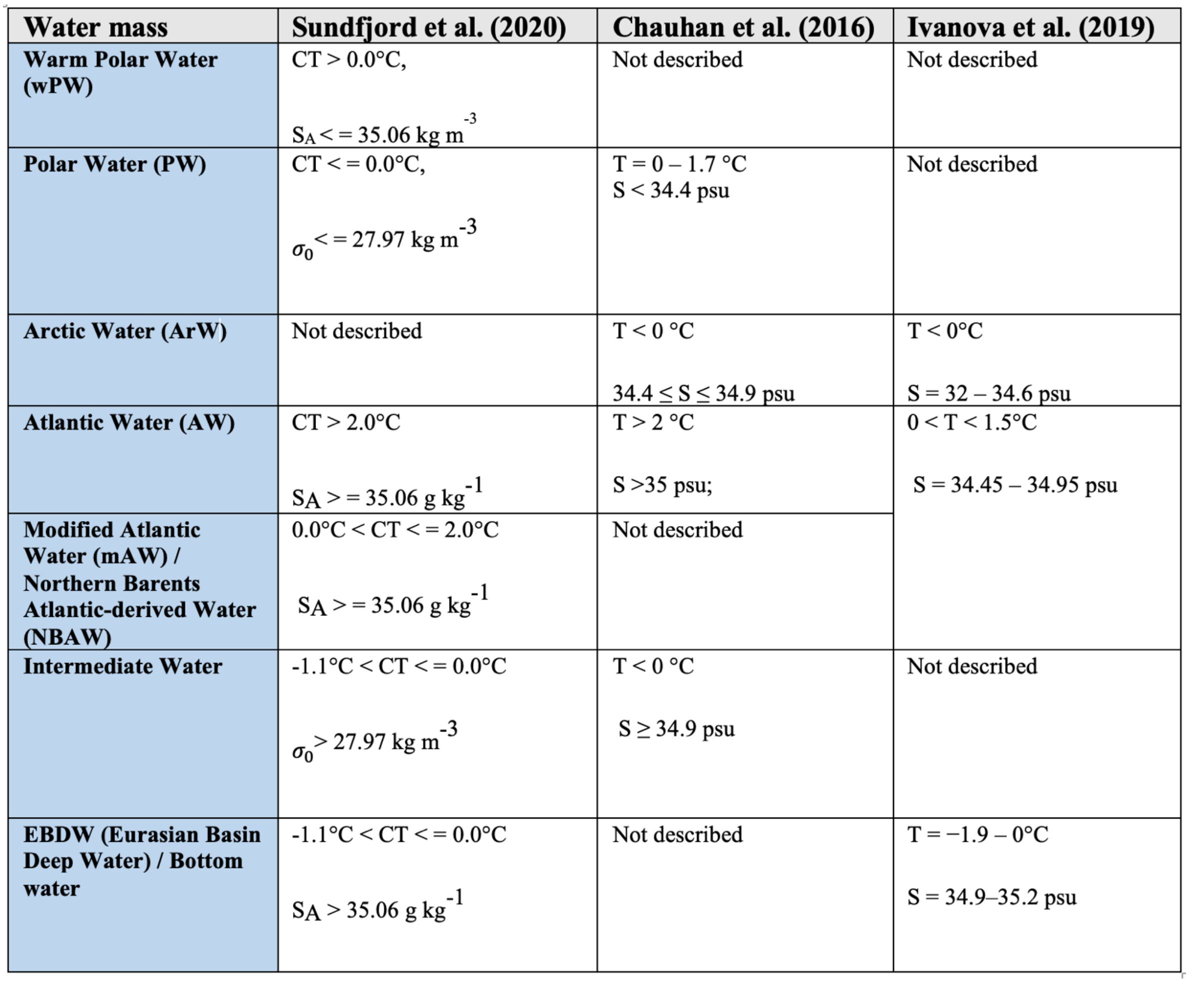

Water mass	Sundfjord et al. (2020)	Chauhan et al. (2016)	Ivanova et al. (2019)
Warm Polar Water (wPW)	CT > 0.0°C, $S_A <= 35.06$ kg m^{-3}	Not described	Not described
Polar Water (PW)	CT < = 0.0°C, $\sigma_0 <= 27.97$ kg m^{-3}	T = 0 – 1.7 °C S < 34.4 psu	Not described
Arctic Water (ArW)	Not described	T < 0 °C $34.4 \leq S \leq 34.9$ psu	T < 0°C S = 32 – 34.6 psu
Atlantic Water (AW)	CT > 2.0°C $S_A >= 35.06$ g kg^{-1}	T > 2 °C S >35 psu;	0 < T < 1.5°C S = 34.45 – 34.95 psu
Modified Atlantic Water (mAW) / Northern Barents Atlantic-derived Water (NBAW)	0.0°C < CT < = 2.0°C $S_A >= 35.06$ g kg^{-1}	Not described	
Intermediate Water	-1.1°C < CT < = 0.0°C $\sigma_0 > 27.97$ kg m^{-3}	T < 0 °C $S \geq 34.9$ psu	Not described
EBDW (Eurasian Basin Deep Water) / Bottom water	-1.1°C < CT < = 0.0°C $S_A > 35.06$ g kg^{-1}	Not described	T = −1.9 – 0°C S = 34.9–35.2 psu

3.4.4 Modern day oceanography

A CTD was deployed at NPAL14 on the 7th of October 2018 to obtain the physical properties of the water column at the site. The CTD Carousel has 12 Niskin bottles used to collect water samples at different depths in the water column. The CTD is released into the water and as it moves up through the water column an electromagnetic lanyard system is used to close the bottles and capture the water samples. The CTD also has various sensors which provide real time measurements of conductivity, temperature, pressure, and oxygen through the water column. CTD data can be used to obtain information about the water profile at a site.

The water profile for NPAL14 has a mixed layer of approximately 35 m with a water temperature of 1.31°C and a salinity of 34.4 (figure 3.7). This is warm Polar Water (wPW) after Sundfjord et al. (2020) but has previously been considered cold polar water by Chauhan et al. (2016) due to its relatively cold and fresh properties locally. Below the mixed layer there is a halocline from 35 to 100 m, where salinity increases from 34.4 to 34.8 and temperature fluctuates between 1.3 and 1.9 °C. Below the halocline at a depth of approximately 116 m the maximum AW influence is found. It is seen as a bulge in temperature with temperatures reaching between 2°C and 2.78°C and salinity reaching a maximum of 34.9 . This is warm enough to be classified as pure AW (≥ 2°C, table 3.1) , however it is slightly too fresh (AW ≥ 35.06, table 3.1) suggesting slight modification through mixing or precipitation. Below 180m in the water column salinity remains constant (~34.85) with depth while temperature continues to decrease with depth down to 0.86 °C—all falling within the range of mAW of Sundfjord et al. (2020). From approximately 300 m to the bottom, there is a water mass with near constant salinity (~34.85) ranging in temperature from 0.86 to 1.09 °C. This water mass also falls within the range of mAW, although with slightly different properties than the one overlying it, suggesting a slightly different, more modified AW (mainly through heat loss). The depth range and influence of AW found in my study agrees with Ivanova et al. (2019) who also noted the influence of AW (also called Atlantic modified water or Northern Barents Atlantic-derived Water) below the pycnocline in the Kvitøya Trough. Chauhan et al. (2016) also identified a thick layer of AW between 110 and 488 m (S= 35.05 and 2.2 < T< 3.6 °C) using CTD data taken in September slightly to the north of our core site (81°16°N, 26°13° E).

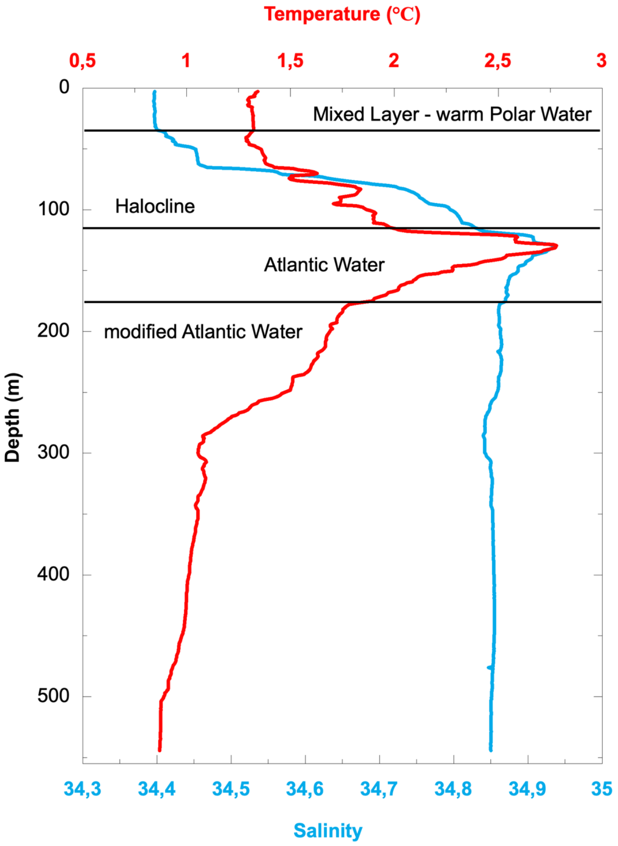

Figure 3.7 CTD profile at NPAL14 in the Kvitøya Trough.

4. Methods and Theory

The material used in this thesis was collected on the Nansen Legacy paleo cruise which took place from the 26th of September to the 20th of October 2018 onboard the research vessel Kronprins Håkon. The material and data used for this thesis were obtained from paleo station 14 (NPAL14) (80.69° N, 28.95° E) which is located in the Kvitøya trough.

4.1 Field methods

4.1.1 Gravity core - KH18-10-14GC-1

Multiple cores were obtained at Station NPAL14; three sets of multicores, two calypso cores and three gravity cores. The gravity core, KH18-10-14GC-1, length 591cm, obtained at a water depth of 552 m was used for analysis in this Master thesis. KH18-10-14GC-1 was taken using a gravity corer, which is a steal barrel loaded with weights that is lowered through the water column. Once the core is 20 – 30 m above the ground it is stopped and stabilized before being released into the sediment. It penetrates through the sediment due to its gravitational force. A 'core catcher' at the end of the core prevents the sediment from coming out the bottom of the barrel (Husum et al., 2020).

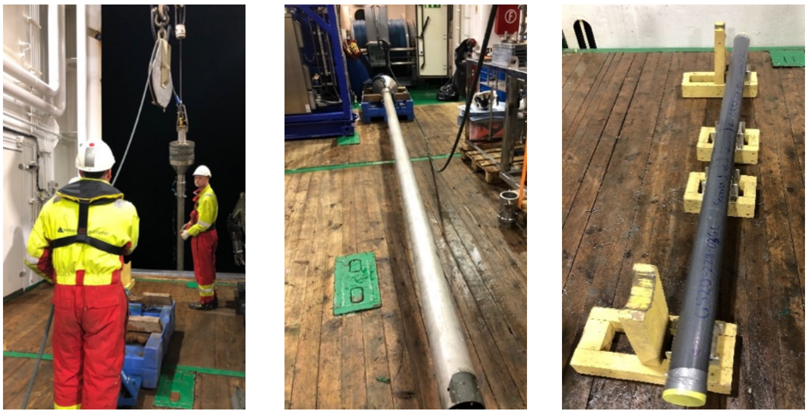

Figure 4.1 A gravity corer (not KH18-10-14GC-1) being lowered from the hull into the ocean (left). A gravity corer with a 5 m steel barrel (middle). A gravity core after being capped and sealed (right) (photos: Allegra Liltved).

4.2 Laboratory methods

In the EARTHLAB at the University of Bergen members of the Nansen Legacy paleo group CT scanned the core. The core was split longitudinally and divided into the working half and the archive half. Thereafter the Nansen Legacy paleo group and I, sampled the working half every cm, bagged the samples, and froze them immediately at - 40°C to avoid respiration of organic matter, pH drop, and carbonate dissolution. After which the samples were freeze dried. I wet sieved the freeze-dried samples and thereafter picked and prepared foraminifera for stable isotope and Mg/Ca analysis. The Nansen Legacy paleo group also performed XRF and MST analysis on the archive half of the core, sampled it in 2cm intervals and stored the samples in the freezer at -40°C. In this section the methods used for sample preparation and analysis will be explained, along with a brief background on the instruments used.

4.2.1 CT scan

X-ray computed tomography is a method which uses the attenuation of X-rays by a material in order to obtain the internal structures of objects (van der Bilt et al., 2021). The CT scanner was originally invented for medical purposes but is becoming increasingly useful for sedimentology studies. The ProCon CT-ALPHA CORE at the EARTHLAB at the University of Bergen was used to obtain x-ray images of core KH18-10-14GC-1. The core is placed upright inside the CT scanner and is rotated while it is scanned by a 240 kV microfocus X-Ray source source. The X-ray beam passes through the core and is collected by multiple detectors that move vertically while the core is being scanned (van der Bilt et al., 2021). For each rotation many X-ray slices of the core are produced which are joined together to construct a 3D visualization of the core (Støren et al., 2010). In CT scans, less dense regions of the core are often seen as darker areas while denser sections are lighter, due to more radiation being absorbed (Støren et al., 2010).

4.2.2 X-Ray Fluorescence analysis

X-Ray Fluorescence (XRF) analysis is a technique which makes use of x-rays to excite atoms in a core. The characteristic emission spectra depending on the atomic number of the element makes it possible to obtain elemental profiles of the core (Rothwell and Croudace, 2015). ITRAX is a multifunctional and non-destructive X-ray core scanner which can record optical and radiographic images, as well as elemental profiles of sediment cores (Croudace et al., 2006). This automated core scanner is made up of a measuring tower containing an optical camera, laser triangulating system, motorized XRF detector, an X-ray focusing unit, an X-ray camera and a radioactive X-ray source (figure 4.2). The X-ray source emits a beam which is focused through a flat capillary wave guide and irradiates the core (Croudace et al., 2006).

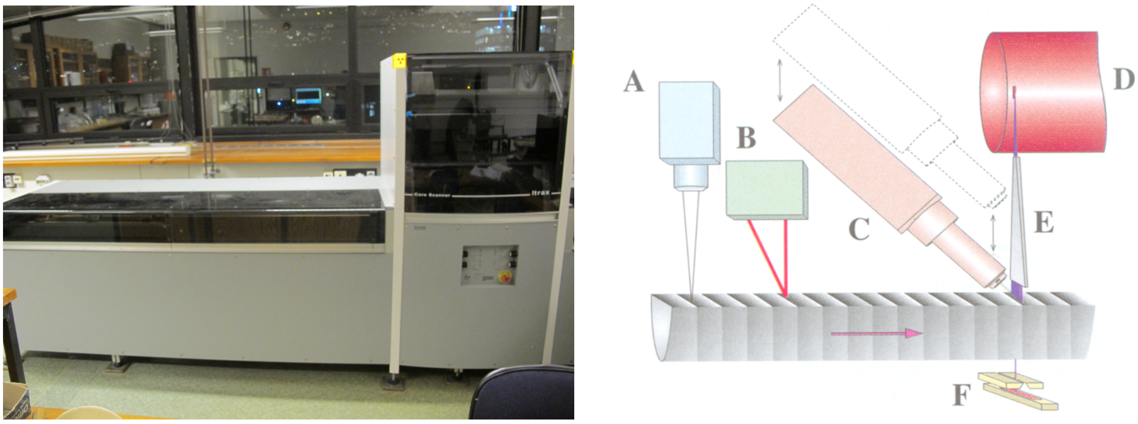

Figure 4.2 Photograph of the ITRAX core scanner at UiB (photograph: Allegra Liltved) (left). The components of the ITRAX system including the (A) optical line camera, (B) laser triangulation system, (C) motorized XRF Si-drift chamber detector, (D) X-ray tube, (E) flat beam X-ray waveguide and (F) X-ray line camera. The arrow indicating the direction of movement of the core past the sensors (right) (Croudace et al., 2006).

The split sediment core is smoothed with a spatula and put on the motorized track and a surface scan is done. The core is first scanned to determine core length and surface topography in order to avoid collisions between the core and detector, and voltage of the x-ray source is determined (Thomson et al., 2006) The likely elemental composition of the core is defined. The optical camera obtains high quality digital images of the core. The core is covered in a thin foil and as it moves incrementally along the motorized track the 3kW X-ray source emits a voltage current that obtains optimum excitation of the biggest range of elements in the core (Croudace et al., 2006). The X-rays are focused through the flat beam optical device and the X-ray camera records the X-rays transmitted through the core obtaining 2 cm X-radiographs (Thomson et al., 2006). In these images the darker areas are higher density areas in the core and vice versa. The XRF detector obtains the elemental profiles along the core. The core was scanned at 0.1 cm intervals. Thereafter the Q-spec software is used to determine the individual elemental composition of the core and the elemental readings are given as ratios.

4.2.3 Multi Sensor Track Logger

The multi sensor track (MST) is a non-destructive measurement device that is used to recover physical properties of a split or whole sediment core including the P-wave velocity, bulk density, and magnetic susceptibility. The components of the MST include a conveyor system, a central sensor array, microprocessor, and PC – computer (Gunn and Best, 1998) (figure 4.3).

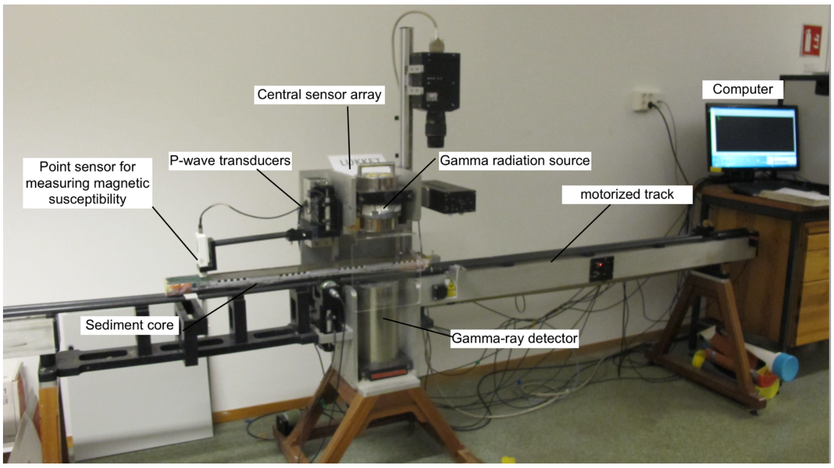

Figure 4.3 A labeled photograph of the multi sensor track at UiB in the Earth Lab showing the central sensor array, motorized tack and measuring systems (photograph: Allegra Liltved).

The core is covered in a thin film and placed on the right hand side-track and then moved along on the conveyor system past the sensors. The central unit assembly has a gamma ray attenuation logger, a p-wave logger and a magnetic susceptibility loop/point sensor. The gamma ray attenuation logger has a radioactive source from which gamma rays are emitted. The gamma rays pass through the core and are picked up by the detector on the other side. The magnetic susceptibility of the core is obtained simultaneously from a point sensor which is moved in and out of contact with the core producing an alternating magnetic field (Gunn and Best, 1998). The magnetic susceptibility was measured at a resolution of 0.2 cm and is given as a relative number in SI units (10^{-5}) which provides us with information about the relative magnetism of the core. The computer automatically correlates the data obtained from the three sensors.

4.2.4 Sampling

Core KH18-10-14GC-1 was sampled in 1 cm intervals which were placed in plastic bags and frozen at - 40°C immediately after sampling. Samples were then freeze-dried using the ALPHA 1-4 LSC. Freeze drying the samples makes it easier for sieving the samples afterwards. The dry weight of the samples was measured. Each sample was then wet sieved using a sieve of 63μm and the fines and the larger fraction were both saved. The > 63μm samples were dried in the oven for a few days and then weighed and put into small glass vials, while the fines (<63μm) were stored in plastic bags.

4.2.5 Picking foraminifera

I picked foraminifera from the interval of 400 – 550 cm of KH18-10-14GC-1 to be used for stable isotope and Mg/Ca analysis. In order to pick the foraminifera, the > 63 μm samples were dry-sieved into three intervals: 150 - 212 μm, 212 - 250 μm and > 250 μm. Three species of foraminifera were picked under the microscope for stable isotope analysis: planktic *Neogloboquadrina pachyderma* (hereinafter *N. pachyderma*) and two benthic species *Nonionellina labradorica* (hereinafter *N. labradorica*) and *Cassidulina neoteretis* (hereinafter *C. neoteretis*). Two benthic species were selected to ensure the most continuous isotopic record possible in the event that intervals of decreased abundance occurred in a given species. The benthic species were picked from all the size fractions above 150 µm, while *N. pachyderma* was picked from a narrower size range of 150 – 212 μm. In order to reduce ontogenic effects (explained further in subchapter 4.4.1) the larger fraction of *N. pachyderma* (212-250 µm) was only used for analysis when there were not enough foraminifera in the smaller fraction. For the stable isotope analysis foraminifera were picked continuously at 2 cm resolution from 400 to 550 cm, which was increased to every 1 cm for the interval between 440 cm and 520 cm. 33 samples, with masses between 87-525 μg, were later picked from 18 depths in the core for Mg/Ca analysis (Appendix D).

N. pachyderma and *C. neoteretis* varied in abundance throughout the core but were for the most part continuous except for a few samples not containing enough material to use for isotope analysis. *N. labradorica,* on the other hand was absent between 523 – 488 cm. In the interval spanning 505 – 501 cm all foraminifera were absent.

4.2.6 Preparation for stable isotope analysis

In order to perform stable isotope analysis on the MAT253 in the FARLAB 30 – 60 µg of foraminifera was needed, which is approximately 1-3 *N.* labradorica, 7-10 *C. neoteretis* and 7-11 *N. pachyderma* . The foraminifera were weighed and lightly cleaned to ensure removal of any unwanted material attached to the shells. The cleaning was done by adding 2-3 drops of methanol to each vial and putting the vial in the ultrasonic bath for 5-10 seconds. The methanol, together with any suspended contaminants, was then carefully removed with a syringe to ensure that no sample material was lost. Post cleaning, the vials were placed in a 50°C oven over night to dry.

4.3 Climate proxies

This section will explain how stable isotope ratios of foraminifera can be used as a climate proxy before explaining how the stable isotope analysis is performed.

Stable isotopes

Stable isotope analysis of carbon and oxygen in biogenic calcite is one of the most established and applied proxies in paleoclimatology and paleoceanography. Stable isotopes are non-radioactive elements with the same atomic number (number of protons) but a different number of neutrons in the nucleus, therefore giving them a different atomic mass number. The ratio of the different isotopes of an element in many geological systems is dependent on a process called fractionation. One way in which fractionation can be described is the partitioning of isotopes between different substances leading to an enrichment or depletion in the heavy or light isotope (Rohling and Cooke, 2003). This partitioning of isotopes is mainly because molecules containing heavier isotopes have higher dissociation energy, greater bond strength and lower vibrational frequency thus making them less reactive than lighter isotopes (Pearson, 2012; White, 2013). Fractionation occurs according to a fraction factor where R_A and R_B are the ratios of the heavy isotope to the light isotope in two different phases: A and B (Mackensen and Schmiedl, 2019).

$$\boxed{\alpha_{A\text{-}B} = R_A/R_B}$$

Equation 4.1 (Rohling and Cooke, 2003)

There are two main types of fractionation that occur in nature: equilibrium and kinetic fractionation. Equilibrium isotopic fractionation is the two-way temperature dependent exchange of isotopes of an element in a system in order to minimize the total energy (White, 2013; Mackensen and Schmiedl, 2019). Kinetic fractionation involves fast or unidirectional reactions where equilibrium is not achieved and arises due to the different reaction rates and/or velocities of the heavy versus the light isotope (Rohling and Cooke, 2003; White, 2013).

The oxygen and carbon isotopic ratios in foraminifera preserved in the sediment provide vital information about past ocean temperatures, global ice coverage, ocean circulation and ocean productivity, allowing scientists to make paleoclimatic and palaeoceanographic reconstructions.

4.3.1 Oxygen isotopes

Oxygen has three naturally occurring stable isotopes: ^{16}O and ^{18}O, which make up 99.76% and 0.20% of oxygen on Earth, and one rarer isotope, ^{17}O, with a relative natural abundance of 0.04% (Rohling and Cooke, 2003). Since the fractionation of oxygen isotopes is quite small the ratio of the heavy ^{18}O to light ^{16}O is expressed using delta notation for convenience's sake, where $\delta^{18}O$ is the per mille (‰) deviation from the standard Vienna Pee Dee Belemite (VPDB). More positive $\delta^{18}O$ values are said to be enriched in the ^{18}O while more negative values are depleted.

$$\boxed{\delta^{18}\mathrm{O} = \left(\frac{\left(\frac{^{18}\mathrm{O}}{^{16}\mathrm{O}}\right)_{\text{sample}}}{\left(\frac{^{18}\mathrm{O}}{^{16}\mathrm{O}}\right)_{\text{standard}}} - 1 \right) \times 1000\ ‰}$$

Equation 4.2

The use of stable oxygen isotopes in geochemistry began in the 1950's with the work of Urey (1947), McCrea (1950) and Epstein et al. (1953) only 20 years after the discovery of the neutron (White, 2013). Harald Urey was the first to propose that the ratio of ^{18}O to ^{16}O in biogenic carbonate of seashells was a function of temperature and could therefore be used to determine oceanic paleotemperatures (Epstein et al., 1951; Pearson, 2012). A paleothermometer equation for the temperature dependent fractionation between calcite and water was defined and was later modified numerous times e.g., it was modified by Emiliani (1955) in order to account for the changing isotopic composition of seawater between glacials and interglacials (Emiliani, 1955) . The equation by O'Neil et al. (1969) was modified for greater accuracy at lower temperatures by Shackleton (1974) as per equation 4.3 below where $\delta^{18}O_{cc}$ is the $\delta^{18}O$ of the carbonate shell and $\delta^{18}O_{sw}$ is the value in equilibrium with sea water:

$$T\ (^{O}C) = 16.9 - 4.38\ (\delta\ ^{18}O_{CC} - \delta\ ^{18}O_{SW}) + 0.10(\delta\ ^{18}O_{CC} - \delta\ ^{18}O_{SW})^{2}$$

Offset value of VSMOW to VPDB = -0.2

Equation 4.3

Through the work of Emiliani (1955) it was discovered that the $\delta^{18}O$ of seawater is primarily affected by global ice sheet coverage, and therefore the $\delta^{18}O$ of foraminiferal calcite (hereafter referred to as $\delta^{18}O_c$) is primarily affected by global ice sheet coverage and secondly by the ocean temperature (Pearson, 2012). According to this equation they found that an increase in $\delta^{18}O_c$ of 1‰ corresponds to a change in ocean temperature of ~ - 4.3°C. In other words, $\delta^{18}O_c$ increases as ocean water temperature decreases and vice versa. This is partly due to the equilibrium fractionation that occurs when $CaCO_3$ depositing marine invertebrates precipitate carbonate. When ocean temperatures are lower fractionation is stronger resulting in more of the heavy ^{18}O isotope being incorporated into the shell because the heavier isotopes have lower energy and make stronger bonds. However, when ocean temperatures are higher, the total energy of the system is higher and therefore the fractionation factor and preferential incorporation of the heavy ^{18}O isotope decreases (Emiliani, 1955). This is however not a linear equation due to there being a decrease in fractionation with increased temperature (Pearson, 2012).

To use paleo-temperature equation, the $\delta^{18}O$ of seawater (hereafter referred to as $\delta^{18}O_{sw}$) in which the foraminifera calcify needs to be known since the temperature calculation is based on the difference between $\delta^{18}O_{sw}$ and $\delta^{18}O_c$ (Epstein et al., 1951; White, 2013). It is therefore important to discuss the processes which govern the $\delta^{18}O_{sw}$. The different mass numbers of the ^{16}O and ^{18}O isotopes result in their fractionation as they move through the hydrological cycle. During evaporation lighter ^{16}O isotope is preferentially evaporated due to its higher vapor pressure (Epstein et al., 1951; Rohling and Cooke, 2003). When clouds precipitate the heavy isotopes leave the clouds first, resulting in the clouds becoming more enriched in the lighter isotope. Clouds which are transported to higher latitudes have successive condensations resulting in precipitation becoming more depleted in the heavy isotope (Rohling and Cooke, 2003). Therefore, precipitation in the high latitudes will be isotopically lighter than precipitation in the tropics due to this cumulative (Rayleigh) distillative loss of ^{18}O. The sequestration of ^{16}O in ice sheets results in an enrichment in global $\delta^{18}O_{sw}$ (Rohling and Cooke, 2003). An increase in ice volume during colder periods will therefore lead to an increase in global $\delta^{18}O_{sw}$. In short, the global ice volume at the time when the foraminifera precipitates has a major effect on $\delta^{18}O_{sw}$ and therefore $\delta^{18}O_c$, with glacial periods having ~1‰ more positive $\delta^{18}O_{sw}$ values (Shackleton and Opdyke, 1973).

Processes which affect regional salinity, such as evaporation and precipitation, similarly have an effect on $\delta^{18}O_{sw}$ meaning that these two variables often have a linear relationship (Epstein et al., 1951). The strength of this linear relationship between salinity and $\delta^{18}O_{sw}$ can vary regionally and temporally due to certain processes, such as fractionation and sea ice formation, causing deviations from the linear relationship (LeGrande and Schmidt, 2006). In the middle to high latitudes the $\delta^{18}O$ to salinity relationship has a steeper slope ($\delta^{18}O$ changes more for a given change in salinity) than in the tropics. This is due to the lower isotopic value of precipitation in high latitudes relative to the tropics where precipitation is similar to seawater values and drives very small changes in $\delta^{18}O$ (leGrande and Schmidt, 2006). For the northwestern Barents Sea, $\delta^{18}O$ and salinity data have been collected and plotted (AeN Paleo Cruise, Ninnemann, unpublished results) (figure 4.4). A linear regression of the whole dataset gives a 0.26 change in $\delta^{18}O_{sw}$ for every 1 unit change in salinity. However, for the more saline part of the record (S >34,6) there is a higher slope of 0.55‰ per 1 change in salinity. This is more appropriate for the study area in this thesis which is affected by AW and agrees with the global database values of LeGrande and Schmidt (2006) showing a slope of 0.5‰ per 1 change in salinity for the mid-latitudes. On a local scale seasonal melting of sea ice or sea ice formation can have a large influence on $\delta^{18}O_{sw}$ (Rohling and Cooke, 2003) tending to shallow the slope (LeGrande and Schmidt, 2006) as is observed in the fresher portions of the Nansen Legacy data (figure 4.4).

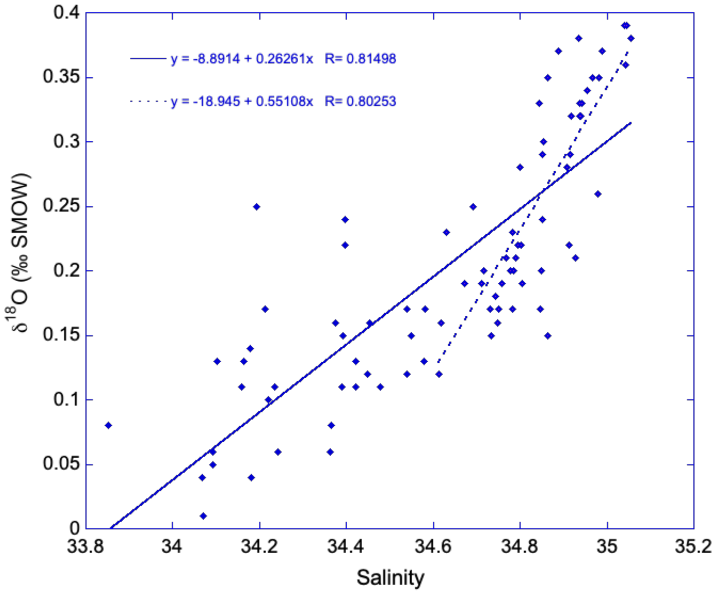

Figure 4.4 The $\delta^{18}O_{sw}$ and salinity relationship in the NW Barents Sea. The shallower slope represents a linear regression of the whole data while the steeper slope shows the relationship under higher salinities (AeN Paleo Cruise, Ninnemann, unpublished results).

Vital effects

Using equation 4.3 it is possible to reconstruct paleotemperatures of the ocean using $\delta^{18}O_c$, however it assumes that foraminifera precipitate in equilibrium with sea water which is not often the case. There are various factors which can be responsible for deviations from this expected equilibrium. Both planktic and benthic foraminifera can show species specific offsets from equilibrium often called ‘vital effects’ (Pearson, 2012). These effects are not well quantified and can be difficult to separate from one another. Planktic foraminifera can be symbiont bearing which means that they host a cloud of photosynthetic symbionts that can affect the pH and carbonate ion concentration of the water, locally, thus affecting $\delta^{18}O$ values (Pearson, 2012). Many planktic foraminifera, including N. pachyderma, also secrete an outer crust of calcite in the later stages of their lives called gametogenic calcite, which is usually enriched in $\delta^{18}O$, thus causing intra-shell variations in $\delta^{18}O$ (Bé, 1980; Kohfeld et al., 1996). For deep water benthic species, symbiont photosynthesis should not be of concern, but benthic foraminifera also show offsets from equilibrium and interspecies differences. A possible reason, called the ontogenic effect, explains that the metabolic rate of juvenile foraminifera may be higher than that of mature species leading to a greater incorporation of metabolic CO_2 during calcification (Rohling and Cooke, 2003). Another complicating factor is that foraminifera may migrate to deeper waters resulting in variable $\delta^{18}O$ values acquired throughout their lifespan or live at different depths in the sediment thus being affected by pore water compositions (Pearson, 2012). It is also important to consider that foraminifera buried in the sediment undergo diageneses which can affect their $\delta^{18}O$ values (Pearson, 2012). The low pH of deep waters and areas of high organic mineralization can result in dissolution of foraminifera whereas post burial crystallization can cause an outer crust of either enriched or depleted $\delta^{18}O$ depending on the conditions of burial (Pearson, 2012).

Apart from the small deviations from equilibrium, $\delta^{18}O$ of foraminifera is nonetheless an extremely useful palaeoceanographic proxy but the complexities should still be acknowledged. Various precautions can be taken to reduce offsets such as using a constrained size fraction, knowing the habitat of the species you are studying and using multi-proxy analysis.

4.3.2 Carbon isotopes

Carbon has two stable isotopes ^{12}C and ^{13}C, which make up 98.89 % and 1.11% of the stable carbon on Earth, respectively (Rohling and Cooke, 2003). $\delta^{13}C$ notation, much like for stable oxygen isotopes, is a way of expressing the ratio of the heavy ^{13}C to the light ^{12}C, normalized by a standard called Vienna Pee Dee Belemnite (VPDB). The ratio of these two stable isotopes of carbon preserved in fossilized foraminifera provides us with insight into past ocean circulation, deep water ventilation and productivity (Mackensen and Schmiedl, 2019).

$$\delta^{13}C = \left[\frac{\left({}^{13}C/{}^{12}C\right)_{sample}}{\left({}^{13}C/{}^{12}C\right)_{VPDB}} - 1 \right] \times 1000$$

Equation 4.4

Dissolved inorganic carbon (DIC) in the ocean exists as three main forms namely carbon dioxide (CO_2), bicarbonate (HCO_{3-}) and carbonate (CO_{3-}), with 90% of DIC being in the form of bicarbonate. Therefore, the $\delta^{13}C$ of DIC (hereinafter referred to as $\delta^{13}C_{DIC}$) in the ocean primarily reflects the $\delta^{13}C$ of bicarbonate (Mackensen and Schmiedl, 2019). Although $\delta^{13}C$ is obtained simultaneously to $\delta^{18}O$ during stable isotope analysis, it was not until the late 1970's that the usefulness of $\delta^{13}C$ for stratigraphic correlation and reconstructing past ocean circulation was recognized (Wagner and Herrle, 2016; Mackensen and Schmiedl, 2019).

The distribution of $\delta^{13}C_{DIC}$ in the ocean is predominantly determined by fractionation processes that occur during photosynthesis and remineralization of organic matter as well as mixing of different water masses (Curry et al., 1988). Phytoplankton in the euphotic zone fix dissolved nutrients, such as nitrate and phosphate, as they photosynthesize and produce organic matter. Due to the pathway through which phytoplankton fix carbon, they preferentially extract ^{12}C from DIC leaving the surface ocean with a high $\delta^{13}C_{DIC}$ values (Eide et al., 2017). This kinetic fractionation results in a mean surface ocean $\delta^{13}C_{DIC}$ of 2.0‰ (PBD) (Curry et al., 1988). As the organic matter sinks through the water column it is remineralized by microbes and the light ^{12}C isotope is released back into the ocean thus forming a gradient of decreasing $\delta^{13}C_{DIC}$ values from the surface to greater depths (Eide et al., 2017). This is why $\delta^{13}C_{DIC}$ values and nutrient concentrations in the ocean are usually inversely coupled. The difference between $\delta^{13}C_{DIC}$ of the surface water and deep water can tell us about the productivity at the surface and the strength of the biological pump (Wagner and Herrle, 2016).

Deep water acquires the $\delta^{13}C_{DIC}$ value of the surface water source from which it forms, known as the preformed value, which is indicative of the amount of photosynthesis that occurred during its residence time in the euphotic zone (Curry et al., 1988). For example, North Atlantic Deep Water forming in the northern hemisphere is formed from surface waters where most of the nutrients have been used for photosynthesis therefore giving it high $\delta^{13}C_{DIC}$ value of ~1.11‰ (PDB) and a low nutrient content (Yu et al., 2008). After a water mass sinks below the thermocline it is only altered by the remineralization of organic matter and mixing of different water masses, and therefore $\delta^{13}C_{DIC}$ can be used as a water mass tracer (Curry et al., 1988). The $\delta^{13}C_{DIC}$ value of water mass decreases as it moves away from where it was ventilated by accumulating the products of organic matter remineralization (Duplessy et al., 1988).

On a more global scale it is important to note that the mean $\delta^{13}C_{DIC}$ of the ocean can also be affected by changes in the global carbon cycle (e.g., increases in the size of the terrestrial biosphere) or perturbations in a source or sink of carbon (e.g., volcanic outgassing, increased weathering) (Ravelo and Hillaire-Marcel, 2007). However, for the purpose of this study local changes in $\delta^{13}C_{DIC}$ will be of greater importance due to the long timescale over which whole ocean changes occur. Although photosynthesis and respiration are the major factors affecting $\delta^{13}C_{DIC}$ distribution locally, thermodynamic fractionation which is the temperature dependent fractionation that takes place when CO_2 is exchanged across the sea-air interface, can also affect $\delta^{13}C_{DIC}$ (Broecker and Maier-Reimer, 1992). Surface water increases in $\delta^{13}C$ by 0.1‰ per 1°C decrease in temperature (Broecker and Maier-Reimer, 1992). Since the time needed for equilibrium between atmospheric CO_2 and the surface ocean to be reached (circa a decade) is longer than the residence time of most water masses at the surface, thermodynamic fractionation does not lead to major issues for $\delta^{13}C_{DIC}$ palaeoceanographic reconstructions (Broecker and Maier-Reimer, 1992; Mackensen and Schmiedl, 2019). It should, however, still be considered in very cold regions (high latitudes) where thermodynamic fractionation can override biological fractionation (Mackensen and Schmiedl, 2019).

Carbon isotopes in foraminiferal calcite

The $\delta^{13}C$ value of carbonate shells is relatively close to $\delta^{13}C_{DIC}$ and therefore fossilized foraminifera can provide us with vital clues about past $\delta^{13}C_{DIC}$ values and processes influencing them such as ocean circulation. However, the $\delta^{13}C$ of foraminiferal tests is for the most part not in equilibrium with the ambient water $\delta^{13}C_{DIC}$ (Wagner and Herrle, 2016). Foraminifera fractionate $\delta^{13}C$ by approximately 1.0 ± 0.2‰ when they calcify but since this value is constant over a wide range of temperatures and precipitation rates it can be corrected for (Ravelo and Hillaire-Marcel, 2007). On the other hand, vital effects can result in an offset of the $\delta^{13}C$ of foraminiferal calcite from ambient water which can vary significantly depending on species and ontogenetic stage (Ravelo and Hillaire-Marcel, 2007; Mackensen and Schmiedl, 2019). These vital effects are due to changes in the internal carbon pool, which is used for shell precipitation, due to photosynthesis and respiration (Ravelo and Hillaire-Marcel, 2007). The $\delta^{13}C$ can therefore be impacted by the rate of photosynthesis, respiration, and calcite precipitation in comparison to the rate at which the DIC of the internal pool is exchanged with the ambient seawater (Ravelo and Hillaire-Marcel, 2007). The foraminiferal $\delta^{13}C$ can also be affected by the rate of carbonate precipitation relative to the time it takes the shell to reestablish equilibrium with internal pool DIC (McConnaughey et al. (1997) as cited Mackensen and Schmiedl (2019)) which is known as the kinetic effect. The habitat preference of foraminifera can also greatly affect their carbon isotopic ratios. For example, the $\delta^{13}C$ of deep infaunal species can be much lower due to high rates of decomposition of organic matter (and associated light carbon) in the pore waters (Rohling and Cooke, 2003).

The interpretation of the benthic δ^{13}C records is more complicated than for planktic δ^{13}C, as the environmental controls on benthic δ^{13}C are not well understood (Lubinski et al., 2001) and it is affected by the degradation of organic matter in the sediment. The two benthic species used in this thesis, *C. neoteretis* and *N. labradorica*, reside near the sediment-water interface (epifaunal to shallow infaunal (Consolaro et al., 2018) and deeper infaunal), respectively. This means that their δ^{13}C values are highly affected by organic matter degradation and calcite dissolution in the sediment and therefore can differ significantly from the bottom water masses (McCorkle et al., 1985). Therefore, instead of looking at the absolute values, the δ^{13}C gradient in the sediment can provide useful information about the productivity in the water column, with a higher organic carbon flux corresponding to a steeper $\delta^{13}C_{DIC}$ gradient in the sediment (McCorkle et al., 1985; Schmiedl and Mackensen, 2006). The δ^{13}C of pore water is also directly related to oxygen content in the water as the decomposition of organic matter consumes oxygen (McCorkle and Emerson, 1988)

In summary, the δ^{13}C distribution in the ocean is affected by the balance of photosynthesis and respiration, thermodynamic fractionation at the surface, as well as the mixing of different water masses (Wagner and Herrle, 2016). In order to ensure the most accurate reconstructions of the δ^{13}C of sea water using foraminiferal tests it is preferable to use species with known habitats and vital effects, as well as make use of other proxies in conjunction with δ^{13}C (Ravelo and Hillaire-Marcel, 2007).

4.4 Foraminifera

Foraminifera are singled celled, eukaryotic, heterotrophic organisms which secrete calcium carbonate shells called tests. Foraminifera feed on organic matter but some species are ‘symbiont bearing’ which means that they harbor photosynthetic algae for various advantages (Sen Gupta, 1999; Mackensen and Schmiedl, 2019). These ancient organisms use HCO_3 ions from the ocean to precipitate their $CaCO_3$ tests and therefore the tests have δ^{18}O and δ^{13}C values closely related to that of the ocean at the time of precipitation. Hence fossilized foraminiferal tests in the sediment can inform us about the temperature and chemistry of the sea water at the time is precipitation. Due to their abundance and long existence on planet Earth, with the oldest fossils dating back to the Cambrian, they provide excellent records of past ocean temperatures and circulation patterns. Foraminifera have variable habitats with some species living at the top of the water column in or near the euphotic zone, called planktic foraminifera, and others living on or within the ocean floor sediment, called benthic foraminifera. During their life cycle (ontogeny), which ranges from weeks to months, and sometimes even years, foraminifera build a first chamber called a proloculus and they then continue to add new chambers to the proloculus (Pearson, 2012).

4.4.1 Planktic foraminifera

Neogloboquadrina pachyderma

Planktic foraminifera live in the photic zone of the ocean and their living depth depends on many factors including temperature and food availability. The species of planktic foraminifera that was used for this study is *Neogloboquadrina pachyderma* (previously *N. pachyderm*, (Darling et al., 2006)). *N. pachyderma* is a polar to subpolar species which dominates polar foraminifera assemblages by making up 90% of the population in the northern high-latitudes (Greco et al., 2019). *N. pachyderma* generally prefers fresher, colder conditions (Carstens and Wefer, 1992) and is associated with polar surface water (Kohfeld et al., 1996). *N. pachyderma* abundances and chemistry have long been used in Artic Ocean research for monitoring changes in water mass geometry and connecting these observations to changes in THC and atmospheric fluctuations (Kohfeld et al., 1996).

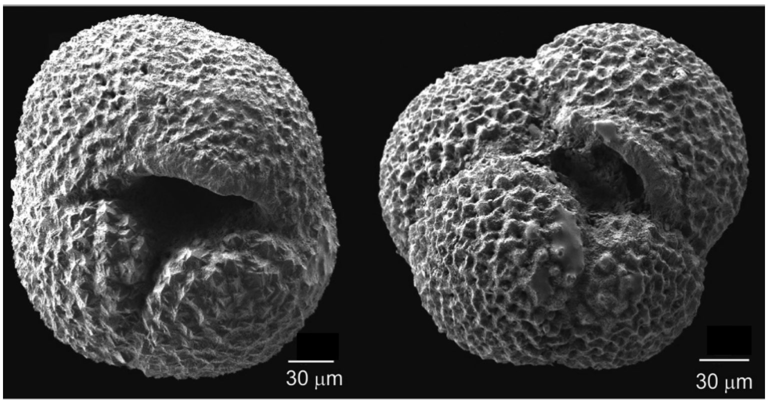

Figure 4.5 Two scanning electron microscope images of *N. pachyderma* (s.) (Chauhan et al., 2016).

It is important to know the depth habitat in which *N. pachyderma* (s.) calcifies in order to use the stable isotope ratios from its tests as palaeoceanographic proxies. Studies have shown that *N. pachyderma's* habitat in the water column can vary quite significantly depending on a variety of factors such as temperature, density stratification of the water column as well as chlorophyll maximum (Kohfeld et al., 1996). The first study using plankton tows to determine the depth habitat of *N. pachyderma* found that south of 83°N the highest concentration of *N. pachyderma* occurred just below the pycnocline at ~100 m (Carstens and Wefer, 1992). While north of 83°N the maximum abundance of this species was found shallower than 50 m in the fresher and colder water (Carstens and Wefer, 1992). Greco et al. (2019), also found that the highest concentration of *N. pachyderma* was found in the sub surface ocean between 25 – 280 m but that it showed no specific relationship to temperature, density or salinity. In this study it was found that the depth preference had a relationship with chlorophyll at the surface and sea ice cover; with *N. pachyderma* mainly living at a depth of 50 -100 m, when there was high chlorophyll and sea ice cover but deepening slightly (74 – 150 m) if sea ice coverage and chlorophyll concentration decreased (Greco et al., 2019). Another study done off the coast of eastern Greenland also found that peak abundance of *N. pachyderma* corresponds to chlorophyll maximum zones between 20 - 80 m water depth (Kohfeld et al., 1996). In summary, *N. pachyderma* in the Northern Atlantic and Arctic Ocean is usually found residing between 25 – 280 m with an average depth of 100 m (Carstens and Wefer, 1992; Greco et al., 2019) and gametogenic encrustation usually occurs in the main pycnocline (100-200 depth) (Kohfeld et al., 1996).

One advantage of using *N. pachyderma* for stable isotope analysis is that it is not symbiont bearing which means that photosynthesis of symbionts does not contribute to its offset from $\delta^{18}O_{sw}$ (Livsey et al., 2020). However, *N. pachyderma* can secrete an additional layer of calcite towards the end of its life span which is called 'gametogenic calcite'. This encrusting process can occur at greater depths then where the ontogenetic calcite was precipitated causing up to 3.3‰ intra-shell variability in $\delta^{18}O$ (Kozdon et al., 2008; Livsey et al., 2020). Since the technique used for stable isotope analysis dissolves the whole shell the $\delta^{18}O$ values are averaged within the shell but this can still contribute significantly to the vital effects. $\delta^{18}O$ values for *N. pachyderma* in the Arctic Ocean have been found to have a consistent offset from $\delta^{18}O$ of equilibrium calcite of 1 ‰ (Duplessy et al., 2001).

4.4.2 Benthic foraminifera

Benthic foraminifera are useful indicators of nutrient concentrations in the sediment, and they can also provide reliable δ^{18}O records. Some benthic foraminifera prefer to live at the sediment water boundary (called epifaunal) and infaunal foraminifera prefer to live within the sediment (Sen Gupta, 1999). The depth at which infaunal foraminifera live within the sediment can have a significant impact on their isotope ratios due to large differences in pore water isotopic gradients. Some deep infaunal foraminifera can live up to several centimeters deep in the sediment (Ivanova et al., 2008). The abundance and depth of foraminifera in the sediment is controlled by organic matter flux, oxygen concentration and ice cover which can affect productivity at the surface and therefore organic matter flux (Hunt and Corliss, 1993). The habitat of benthic foraminifera is not as affected by changing water masses as planktic foraminifera (Wollenburg and Mackensen, 1998). For this thesis two benthic foraminifera species, *C. neoteretis* and *N. labradorica*, were picked.

Cassidulina neoteretis

C. neoteretis is an Arctic epifaunal to shallow infaunal species (Consolaro et al., 2018) which has been used for many years in foraminiferal assemblage and isotope chemistry studies in the Nordic seas and Artic Ocean. There is a morphotype of *C. neoteretis* found in the Arctic Ocean and cold boreal regions called *C.teretis*. According to Seidenkrantz (1995) *C. neoteretis* replaced *C.teretis* between 2.3 - 2 Ma in the North Atlantic. *C. neoteretis* differs only slightly from *C. teretis* being smaller in size and having a slightly smoother, broader apertural plate than *C. teretis* (Seidenkrantz, 1995). These minor morphological differences can only be identified using a scanning electron microscope and the distinctions between the two types were only made in order to use this morphological change as a bio stratigraphical marker (Lazar et al., 2016). Lazar et al. (2016) found these morphotypes coexisting in the sediment with a gradual time-transgressive transition from *C. teretis* to *C. neoteretis*, mentioning that they could in fact be ecophenotypes. Lubinski et al. (2001) also considers them as one species. Since *C. neoteretis* and *C. teretis* only have slightly variable morphologies which cannot be identified using the microscope that was used for this thesis, they will be treated as one species in this thesis and referred to as the most recent version: *C. neoteretis*.

C. neoteretis in the modern ocean is mainly found in water temperatures ranging from 0.5 - 3°C and depths ranging from 200 m to 1400 m (Wollenburg and Mackensen, 1998). Its depth preference is mainly affected by AW depth, food supply, productivity at the surface and sea ice cover (Cronin et al., 2019). This species is usually found in areas with seasonal sea ice cover (Wollenburg and Mackensen, 1998). *C. neoteretis* is a prominent species in AW and can therefore be used as an indicator of chilled intermediate depth AW (Chauhan et al., 2016; Cronin et al., 2019). *C. neoteretis* can be found in Polar Surface Water but this is not very common and is not usually associated with Artic Ocean deep water masses (Cronin et al., 2019).

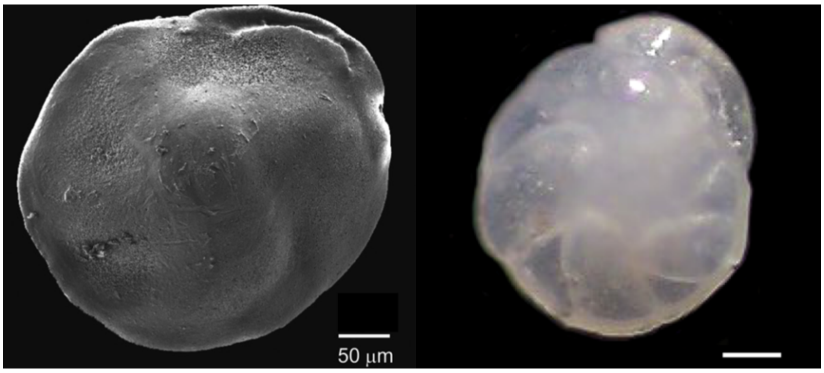

Figure 4.6 Scanning electron image of *C. neoteretis* (left) (Chauhan et al., 2016) and a light microscope image of *C. neoteretis* (right) (Cage et al., 2021).

It is still debated to what extent the $\delta^{18}O$ values of *C. neoteretis* deviate from $\delta^{18}O_{sw}$ (Cronin et al., 2019). Most studies using *C. neoteretis* find that they excrete shells close to equilibrium with surrounding water with an offset between 0.16‰ (Chauhan et al., 2016) and 0.504‰ (Lubinski et al., 2001) with respect to sea water. *C. neoteretis* populations have seen large variations in abundance since the last deglaciation which means that they can be used as a bio stratigraphic markers and they are also very useful for stable isotope analysis if the disequilibrium offset is known (Cronin et al., 2019) .

Nonionellina labradorica

N. labradorica is a deep infaunal species which feeds on phytoplankton detritus in the sediment (Hunt and Corliss, 1993). *N. labradorica* is a species found in water masses with cold, polar conditions and high productivity and is often associated with frontal zones (Chauhan et al., 2016). According to some studies *N. labradorica* is associated with Transformed AW (Hald and Korsun, 1997). In a study done in the Canadian Archipelago this species was found to prefer a depth of 1.0 – 2.5 cm in sediment (Hunt and Corliss, 1993) but it has been found as deep as 8 -10 cm in the sediment on the western shelf of Spitzbergen

(Ivanova et al., 2008). This may be due to a search for food, fear of predation or possibly bioturbation in the core (Ivanova et al., 2008). *N. labradorica* has been estimated to have a positive offset from equilibrium of 0.28‰ (Ivanova et al., 2008).

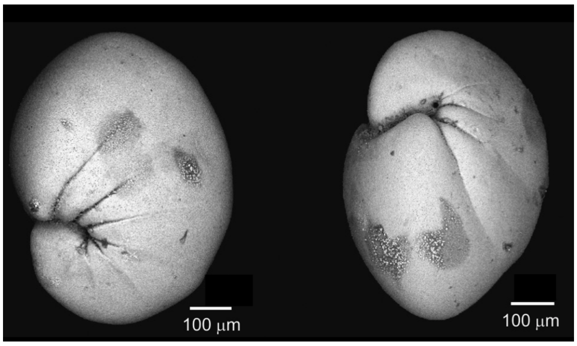

Figure 4.7. Scanning electron microscope images of two *N. labradorica* tests (Chauhan et al., 2016)

4.5 Mass spectrometry

In order to obtain δ^{13}C and δ^{18}O records for KH18-10-14-GC1, the benthic and planktic foraminifera were run on the Thermo Finnigan MAT253 in the FARLAB (figure 4.8) at the University of Bergen. The MAT253 provides sensitive and precise isotopic measurements of different stable isotopes using Isotope Ratio Mass Spectrometry (IRMS). IRMS is a classical technique which separates an ionized beam of molecules based on the mass to charge ratio of the different molecules (m/z).

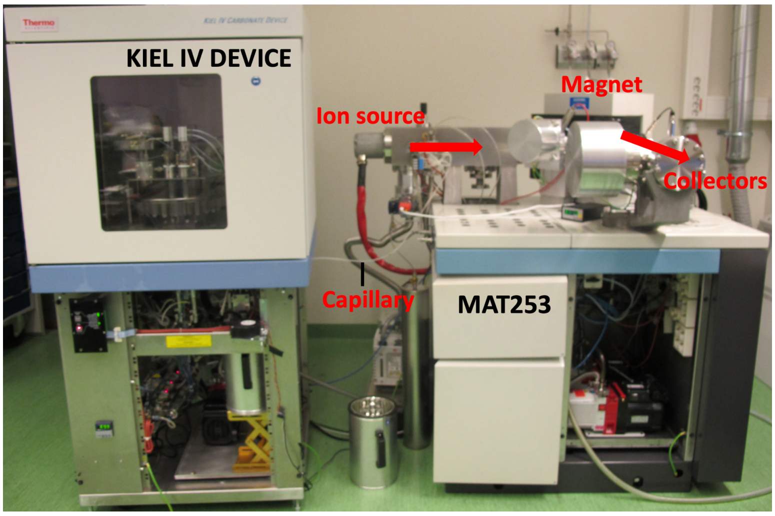

Figure 4.8 Photograph of the MAT253 connected to the KIEL IV automated carbonate device. The samples are acidified in the KIEL device and the gas passes through the capillary into the ion source of the MAT253 (photo: Allegra Liltved)

The MAT253 mass spectrometer is coupled to a Kiel Device in which the 30 - 60 µg carbonate samples (this study) are acidified to form CO_2. This is done through the addition of three drops of phosphoric acid to each sample while the samples are kept at a constant temperature of 70°C. The gas is sent through cooling traps where it is frozen and then heated in order to isolate CO_2 from other the gases, contaminants, and water. The purified and concentrated CO_2 is transferred via a capillary to the ion source of the MAT253. The MAT253 has three components namely, the source, mass analyzer and collector. The source of this mass spectrometer is an Electron Ionization (EI) source where the CO_2 molecules are ionized in a high vacuum chamber by electron impact ionization, to form a beam of high energy ions. The ion beam is focused through lenses and accelerated under a high voltage gradient (10KV) through a magnetic field at an angel of 26.5°(ThermoFinnigan, 2002). In the magnetic field the light ions are deflected more than the heavier ions therefore separating the ions according to their mass/charge ratio. The separated beams are focused, collected, and amplified in 3 Faraday cups (ThermoFinnigan, 2002). The mass spectrometer measures two ratios: mass 45/44 which is primarily the ratio of $^{13}C^{16}O^{16}O/^{12}C^{16}O^{16}O$ and 46/44 which is primarily the ratio of $^{12}C^{18}O^{16}O/^{12}C^{16}O^{16}O$ (Rohling and Cooke, 2003).

The MAT253 has a 'Dual Inlet System' allowing for a reference gas with a known isotopic value to be measured alternately with the samples, thereby providing a means of accounting for instrumental effects such as temperature drift and changes in sensitivity (Werner and Brand, 2001), as well as correcting for fractionation which occurs during gas ionization. This system, developed by Urey and McKinny in the 1950s, is accomplished in practice through the use of a 'change over valve' which switches the inflow of gas between the reference gas and sample gas, pumping the gas either into the waste line or into the mass spectrometer for measurement (Werner and Brand, 2001).

Standards and corrections

The MAT253 provides $\delta^{18}O$ and $\delta^{13}C$ reported in per mille (‰) deviations from the international scale known as Vienna Pee Dee Belemnite (VPDB) (Curry et al., 1988). This is done with the use of the reference gas with a known isotopic composition. Using the standard gas, the mass spectrometer internally corrects for the fractionation of $\delta^{18}O$ when carbonate is converted to CO_2 gas as well as small contribution of the rare isotope ^{17}O (Rohling and Cooke, 2003). VPDB standard is based on an older standard (PDB) which was taken from a belemnite fossil found in a rock formation from South Carolina called the Cretaceous Pee Dee, but this source has now been exhausted (Rohling and Cooke, 2003).These floating values then need to be corrected using internal carbonate standards with known values on the VPDB scale. Standards are weighed out with similar weights as the samples and are run along with the samples. In the FARLAB the repeated measurements of the working standards Carrara Marble 12 (CM12) and RIEDEL are used to calculate the long term precision of the machine. The inhouse standards are then calibrated to the VPDB scale using the international reference standard National Bureau of Standards-19 (NBS19) which is limestone with a fixed value on the VPDB scale of $\delta^{13}C_{VPDB}$ = 1.95 and $\delta^{18}O_{VPDB}$ = - 2.2, as well as NBS-18 which is carbonatite with a fixed value relative to VPDB of $\delta^{13}C_{VPDB}$ = -5.01 and $\delta^{18}O_{VPDB}$ = -23.2. The analytical precision of the machine, based on the long-term reproducibility of in-house standards (CM12 and RIEDEL) run with the samples, was equal to or better than 0.06 and 0.03 (in‰, 1σ SD) for oxygen and carbon isotopes respectively at the time of analyses.

5. Chronology

Accurate dating of a core is essential to inform us about the timing of events. The findings in this thesis would be of little significance without a good age model. Choosing the correct calibration curve and reservoir age for this core was not simple due to the core's polar origin. In this section the radiocarbon dating technique and method used to create the age model will be discussed.

5.1 Dating method

Benthic and planktic foraminifera tests from cores KH18-10-14-GC-1 and KH18-10-14-GC-3 were sent to LARA lab (the Laboratory for the Analysis of Radiocarbon with AMS) at the University of Bern, Switzerland. Using ^{14}C accelerator mass spectrometry (AMS) dating, a total of 16 AMS dates were obtained from KH18-10-14-GC-1 and 14 AMS dates from the neighboring core, KH18-10-14-GC-3. The process of how these 30 dates were used to create an age model for our core will be outlined below.

5.1.1 AMS radiocarbon dating

The three isotopes of carbon, ^{14}C, ^{13}C and ^{12}C, are continuously cycled between the atmosphere, ocean, and terrestrial biosphere. ^{14}C, often referred to as radiocarbon due to its radioactive nature, has proven very useful as a dating method due to this element having a known half-life ~5700 ± 30 years (Bella et al., 1968; Quarta et al., 2021). Radiocarbon is constantly formed in the upper atmosphere when secondary neutrons interact with nitrogen. Thereafter it joins with oxygen to form 'heavy' carbon dioxide molecules ($^{14}CO_2$) (Bowman, 1990). As these 'heavy' carbon dioxide molecules move through the carbon cycle they are taken up by terrestrial organisms through photosynthesis and are also exchanged between the atmosphere and the ocean, and incorporated into biota in the ocean (Alves et al., 2018).

Radiocarbon is constantly exchanged between living organisms and their carbon sources until the organism dies and becomes a closed system (Alves et al., 2018). From the time of death, the radiocarbon in the organism is no longer replenished by the source and therefore the known rate of decay of radiocarbon can be used to determine the age of the material/organism. This is referred to as radiocarbon dating. Equation 5.1 below (Quarta et al., 2021) shows the decay of carbon to nitrogen releasing one electron (e^-) and one electron antineutrino ($\bar{v}$).

$$^{14}_{6}C \rightarrow {}^{14}_{7}N + e^- + \bar{\nu}$$

Equation 5.1

$$\left(\frac{^{14}_{6}C}{^{12}_{6}C}\right)_t = \left(\frac{^{14}_{6}C}{^{12}_{6}C}\right)_0 e^{-\frac{(\ln 2)\times t}{t_{1/2}}}$$

Equation 5.2

The age of the sample can be determined by the above exponential decay equation (equation 5.2) (Quarta et al., 2021) which assumes that the ^{14}C concentration of the carbon reservoir from which the organism formed remains constant over time (Alves et al., 2018). The ^{14}C concentration of the atmosphere is however not constant and fluctuates over time due to changes in the cosmic ray flux, solar activity, and Earth's magnetic field strength, therefore giving samples a radiocarbon age that differs from their true calendar age. This discordance requires calibration methods using carbon records with known ages (Alves et al., 2019). Radiocarbon dates from terrestrial samples are calibrated using the IntCal20 calibration curve which was constructed by measuring ^{14}C concentrations from absolutely dated records such as tree rings (Reimer et al., 2020). Calibration curves like IntCal20 enable efficient conversion from ^{14}C years to calendar years.

Calibration is more complicated for marine samples, as the ocean has a heterogenous ^{14}C concentration due to variable oceanic mixing, radioactive decay and air-sea exchange all playing a role in local ^{14}C concentrations (Butzin et al., 2017). Marine samples have a lower radiocarbon content then the atmosphere because of their large carbon concentrations and the slow mixing rates between the atmosphere, where ^{14}C is produced, and the ocean. This depletion is expressed as the Marine Reservoir Age (MRA) (e.g., Heaton et al. (2020)). The MRA is defined as the ^{14}C age difference between a sample in the ocean and a sample on land which obtained its carbon at the same time. The MRA is highly variable in the oceans making calibration of marine samples not very straightforward. North Atlantic surface water currently has an age of between 400 – 500 years but this could have changed by several hundreds of years or more during the last deglaciation (Bard, 1988). Marine20 is the latest global ocean calibration curve used to calibrate ^{14}C dates of marine samples (Heaton et al., 2020). It provides an MRA average of the non-polar oceanic regions from 0 – 55 000 cal BP (Heaton et al., 2020). Marine20 estimates a significantly older (by approximately 150 - 200 years) global average MRA than its predecessor Marine13. As MRA is not the same around the globe for each region a *ΔR* needs to be found (Mangerud et al., 2006), which is the difference between the MRA at a particular location and the globally-averaged mixed-layer reservoir age (Heaton et al., 2020). The local *ΔR* correction needs to be made in addition to using a known calibration curve such as Marine20.

For this thesis a total of 30 foraminifera samples from KH18-10-14-GC-1 and KH18-10-14-GC-3 were sent for accelerator mass spectrometry (AMS) dating at the LARA lab (table 5.1). AMS dating is a technique which accelerates ions to very high speeds to separate ^{14}C from ^{12}C and ^{13}C isotopes (Alves et al., 2018). In AMS dating samples are usually converted to graphite using graphitization equipment but since many of our samples were small, they were measured in the form of CO_2 gas. Using the ratio of the heavy to the light isotope in equation 5.2 the radiocarbon ages were calculated. To improve the accuracy and resolution of the age model, dates from KH18-10-14-GC-1 (80.69° N, 28.95° E) and the neighboring core KH18-10-14-GC-3 (80.69° N, 28.95° E) were combined. Both cores were obtained at paleo station 14 and display similar Ca/Fe profiles (figure 5.1) although KH18-10-14-GC-3 (510 cm) is 81 cm shorter than KH18-10-14-GC-1 (591 cm). Assuming the same depth profiles between the two core sites, ages obtained from KH18-10-14-GC-3 can be assigned to same depth levels as KH18-10-14-GC-1 and the ages of the cores can be combined to make the age model.

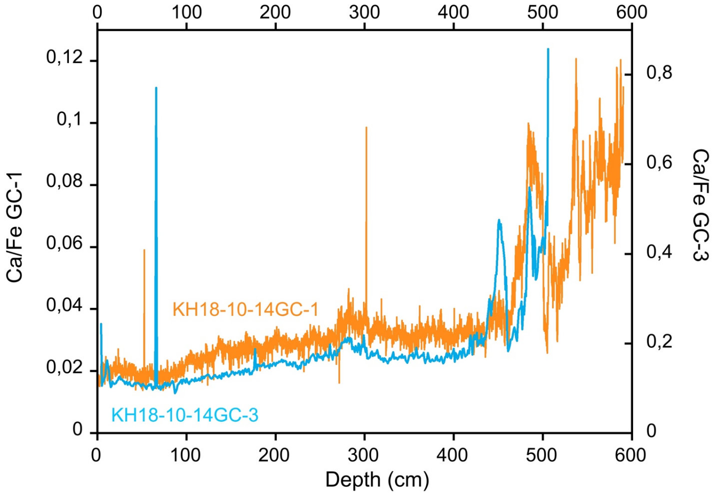

Figure 5.1 Ca/Fe profiles of KH18-10-14-GC-1 (orange) and KH18-10-14-GC-3 (blue). Each profile is plotted on their own respective depth scales without any adjustments. The XRF data for KH18-10-14-GC-1 was measured in the EARTHLAB, UiB and for KH18-10-14-GC-3 was measured at UiT.

Table 5.1 Sample list of the foraminifera sent for AMS dating from KH18-10-14-GC-1 and KH18-10-14-GC-3 with sample details and the AMS ^{14}C dates.

Core name	Lab ID	Depth (cm)	Material used	Species	Method	Uncalibrated AMS 14C (y BP)	Std (1σ) (y)
KH18-10-14-GC1	BE-14212.1.1	5	Benthic foraminifera	Mixed benthics	Gas	871	83
KH18-10-14-GC3	BE-11425.1.1	5	Benthic foraminifera	Mixed benthics	Gas	972	73
KH18-10-14-GC3	BE-11426.1.1	54	Benthic foraminifera	Mixed benthics	Gas	2 292	74
KH18-10-14-GC3	BE-11427.1.1	70	Benthic foraminifera	*Elphidium excavatum*	Gas	2 630	77
KH18-10-14-GC3	BE-11428.1.1	119	Benthic foraminifera	Mixed benthics	Gas	4 269	83
KH18-10-14-GC3	BE-11429.1.1	169	Benthic foraminifera	*Elphidium excavatum*	Gas	5 991	91
KH18-10-14-GC3	BE-11430.1.1	176	Benthic foraminifera	Mixed benthics	Gas	6 284	92
KH18-10-14-GC1	BE-14213.1.1	220	Benthic foraminifera	*Elphidium* spp.	Gas	7 414	105
KH18-10-14-GC3	BE-11431.1.1	227	Benthic foraminifera	*Nonionella labradorica*	Gas	8 128	104
KH18-10-14-GC1	BE-14214.1.1	241	Benthic foraminifera	*Nonionella labradorica*	Graphite	8 282	36
KH18-10-14-GC1	BE-14215.1.1	250	Benthic foraminifera	*Nonionella labradorica*	Graphite	8 456	41
KH18-10-14-GC1	BE-14216.1.1	265	Benthic foraminifera	*Nonionella labradorica*	Graphite	8 675	33
KH18-10-14-GC3	BE-11432.1.1	277	Benthic foraminifera	*Nonionella labradorica*	Graphite	8 859	34
KH18-10-14-GC3	BE-11433.1.1	290	Benthic foraminifera	*Nonionella labradorica*	Graphite	9 030	38
KH18-10-14-GC3	BE-11434.1.1	340	Benthic foraminifera	*Nonionella labradorica*	Graphite	9 603	38
KH18-10-14-GC3	BE-11435.1.1	389	Benthic foraminifera	*Elphidium excavatum*	Gas	10 140	84
KH18-10-14-GC3	BE-11436.1.1	406	Benthic foraminifera	*Elphidium excavatum*	Gas	10 135	117
KH18-10-14-GC1	BE-14217.1.1	420	Benthic foraminifera	*Elphidium* spp.	Gas	10 050	119
KH18-10-14-GC1	BE-14218.1.1	440	Benthic foraminifera	Cibicidoides spp.	Gas	11 088	129
KH18-10-14-GC3	BE-11437.1.1	454	Benthic foraminifera	*Cassidulina neoteretis*	Gas	11 335	139
KH18-10-14-GC1	BE-14219.1.1	462	Benthic foraminifera	*Nonionella labradorica*	Gas	10 682	123
KH18-10-14-GC1	BE-14220.1.1	482	Benthic foraminifera	*Cassidulina neoteretis*	Gas	10 979	125
KH18-10-14-GC1	BE-14221.1.1	488	Benthic foraminifera	*Cassidulina neoteretis*	Gas	11 030	124
KH18-10-14-GC3	BE-11438.1.1	493	Benthic foraminifera	*Elphidium excavatum*	Gas	13 486	109
KH18-10-14-GC1	BE-14222.1.1	500	Benthic foraminifera	Mixed benthics	Gas	12 174	158
KH18-10-14-GC1	BE-14223.1.1	520	Planktic foraminifera	*N. pachyderma* (s)	Gas	12 193	134
KH18-10-14-GC1	BE-14224.1.1	520	Benthic foraminifera	*Pullenia bulloides*	Gas	11 897	134
KH18-10-14-GC1	BE-14225.1.1	537	Planktic foraminifera	*N. pachyderma* (s)	Gas	12 456	141
KH18-10-14-GC1	BE-14226.1.1	537	Benthic foraminifera	*Cassidulina neoteretis*	Gas	12 375	142
KH18-10-14-GC1	BE-14227.1.1	590	Benthic foraminifera	Elphidium excavatum	Gas	13 861	152

5.2 Age model

Age-depth models produce estimated rates of sediment accumulation in a core. For KH18-10-14-GC-1, an age-depth modelling software called ‘Bacon’ version 2.5.2 (Blaauw and Christen, 2011) was used to build a depth-age relationship, which makes use of Bayesian statistics to work out the most accurate accumulation history of a core. ‘Bacon’ can be run through the program ‘R’. ‘Bacon’ divides the core into numerous thin slices and calculates the accumulation rate of these slices using Markov Chain Monte Carlo (MCMC) iterations. The known starting date for each section and the accumulation rates form the age model (Blaauw and Christen, 2013).

The uncalibrated ^{14}C dates obtained from the Lara Lab with their associated depths and uncertainties were used as an input in ‘Bacon’. A suitable local calibration curve had to be chosen to calibrate the age-depth model. Four different calibration methods were investigated in this thesis in order to quantify the uncertainty related to different assumptions: Marine20 using two different reservoir ages for before the Holocene, as well as two local calibration curves. The four age models (figure 5.3) using the respective calibration curves (figure 5.2) produced using Bacon were evaluated and will be discussed below.

Calibration using Marine20

Samples in the ocean need to be corrected for the reservoir effect, which as mentioned above is highly variable throughout the ocean. The Marine20 curve averages the MRA of the surface ocean in the low latitudes, but the local MRA also needs to be known for the specific area of interest. The only available *ΔR* estimate for this region is based on four mollusk shells collected off the coast of west Spitzbergen (table 5.2.; Mangerud and Gulliksen, 1975), and calculated by Bondevik and Gulliksen (in Mangerud et al., 2006) as 105 ± 24. However, the *ΔR* value calculated by Bondevik and Gulliksen (in Mangerud et al., 2006) was determined based on the Marine04 Curve, and cannot be used with the most recent Marine20 curve, where the global marine reservoir ages changed significantly. Therefore, first, the *ΔR* of 105 ± 24 (Marine04) needs to be corrected for Marine20. To do this, the ^{14}C age, ^{14}C age uncertainty (σ), and the collection year (AD) info of the four mollusk shells for the west Spitzbergen, as given in Mangerud et al. (2006) were used (table 5.2).

Table 5.2 Radiocarbon dates obtained from Spitsbergen, Northern Svalbard (Mangerud and Gulliksen, 1975) used to obtain the *ΔR*.

Lab. No	***Species.***	**Locality**	**Lat. N**	**Long. E**	**Depth (m)**	**Year of collection**	**$\delta^{13}C$**	**^{14}C age**	**Mollusc ΔR. Yr of collection relative to Marine04**	**Mollusc ΔR. Yr of collection relative to Marine20**
T-1538	*Chlamys islandica*	Bellsund	c. 77°40’	14-16°	120-190	1926	+0.8	539 ± 37	88 ± 44	-65 ± 37
T-1539	*Chlamys islandica*	Isfjorden	78°07’	14°08’	150-165	1925	+0.5	517 ± 37	66 ± 44	-87 ± 37
T-1540	*Astarte borealis*	Adventbukta	78°15’	15°36’	<20	1878	-0.1	612 ± 50	138 ± 55	-22 ± 50
T-1541	*Astarte borealis*	Magdalenafjorden	79°34’	10°40’	40-80	1878	-0.1	625 ± 45	151 ± 51	-9 ± 45

In this thesis, the application *"deltar"* was used to calculate the *ΔR* and the uncertainty, which is an online program, available through CALIB (http://calib.org/deltar) (Reimer and Reimer, 2017). The *ΔR* for each sample was calculated by subtracting the ^{14}C-age from Marine20 from the radiocarbon age of the sample, using the equation below:

$$\Delta R(t) = {}^{14}C_m - \text{Marine20}C(t) \qquad \text{Equation 5.3}$$

Where $^{14}C_m$ is the measured ^{14}C age of the known-age sample and Marine20C*(t)* is the ^{14}C age of Marine20 at time t (after Reimer and Reimer, 2017). After, the *ΔR* for each sample is calculated relative to the Marine20 curve, the weighted mean of these four values is calculated using the equation 5.4. Then, the new *ΔR* value is calculated as 53 ± 36 based on the four mollusk samples (Mangerud and Gulliksen, 1975), using the latest marine curve, Marine20 (Heaton et al., 2020).

$$\text{weighted mean of } \Delta R = \mu = \frac{\sum_i \frac{\Delta R_i}{\sigma_i^2}}{\sum_i \frac{1}{\sigma_i^2}}$$

$$\text{where } \sigma_i = \text{uncertainty in } \Delta R_i$$

$$\text{weighted uncertainty in mean of } \Delta R = \frac{1}{\sum_i \frac{1}{\sigma_i^2}}$$

$$\text{variance of } \Delta R = \frac{\frac{1}{n-1} \cdot \sum_i \left(\frac{\Delta R_i - \mu}{\sigma_i} \right)^2}{\frac{1}{n} \cdot \sum_i \frac{1}{\sigma_i^2}}$$

$$\text{Standard Deviation of } \Delta R = \sqrt{\text{variance}}$$

Equation 5.4

Finally, to produce curve **A** (figure 5.3) the uncalibrated AMS dates (KH18-10-14-GC-1 & KH18-10-14-GC-3) were calibrated in Bacon using the Marine20 curve (figure 5.2) with the new *ΔR* = -53 ± 36.

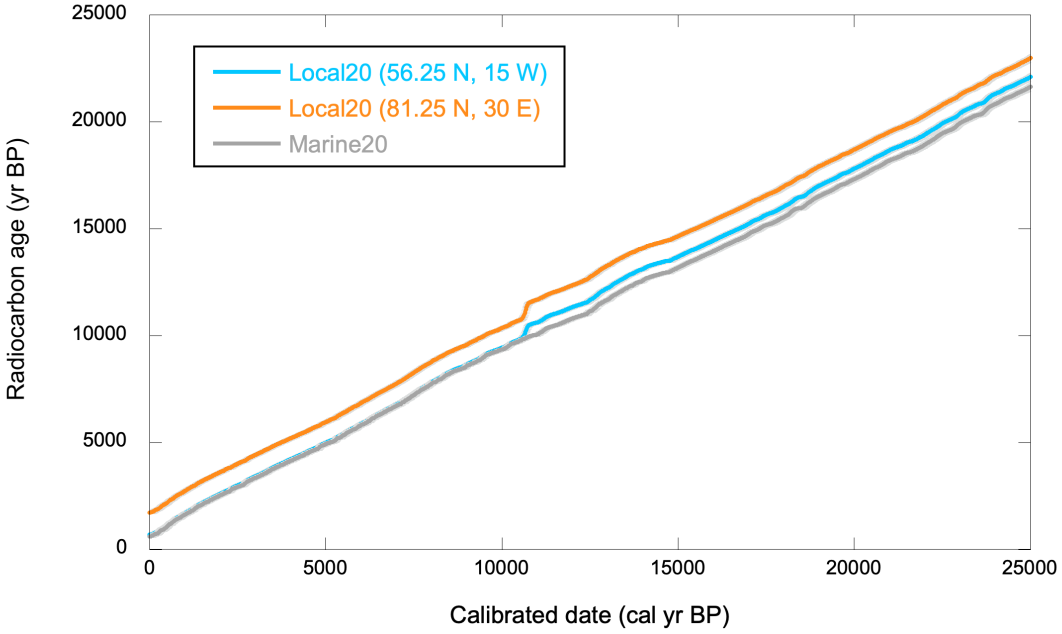

Figure 5.2 The calibration curves that were tested for calibration of the radiocarbon dates to produce age model A-D (figure 5.3). The upper 'local20' curves (orange and blue) were obtained from the LSG OGCM (discussed below). Marine20 is shown in grey. The error is indicated as a light grey border.

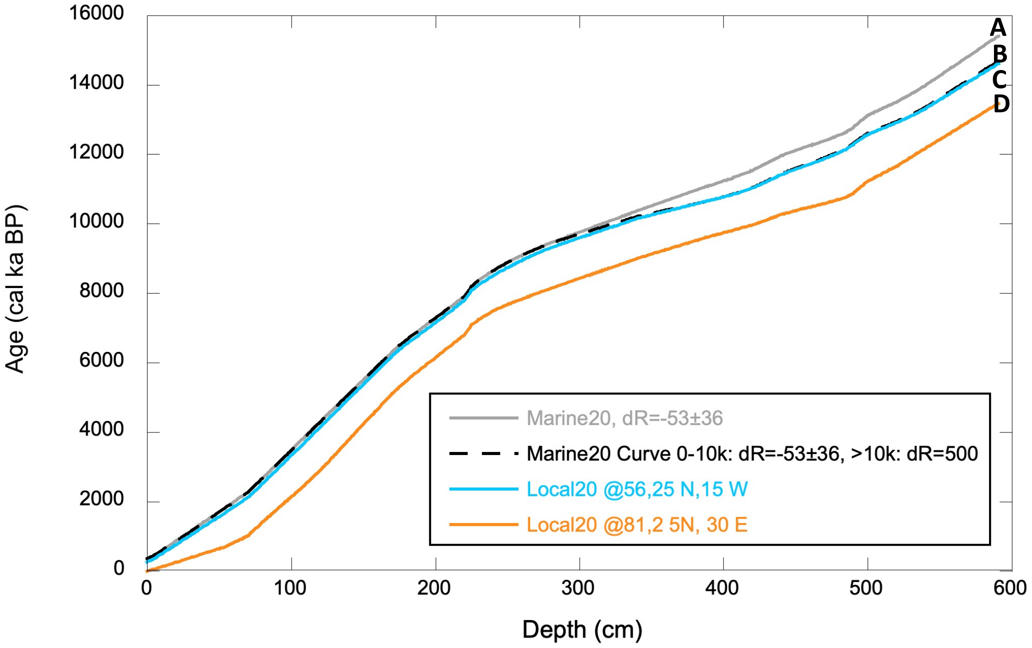

Figure 5.3 Age model comparison of the four age models produced using the respective calibration curves (figure 5.2) where age is the mean age output from Bacon. Curve **A** is the age model calibrated using Marine20 and ΔR =-53 ± 36 and curve **B** is also calibrated using Marine20 but the ΔR is increased to 500 before the Holocene. Plot **C** and **D** show the age models produced using the Local20 calibration curves obtained for two different coordinates using the LSG OGCM.

The lack of pre bomb radiocarbon dates from northern Svalbard means that the *ΔR* for this area is not very well established. Marine20 is also not adequate for calibration of samples from polar regions (Heaton et al., 2020). This is because ocean circulation, sea ice and wind patterns can cause higher variability of marine radiocarbon concentrations in the polar regions (Heaton et al., 2020). In the polar regions, high sea ice cover limits the uptake of $^{14}CO_2$ by the ocean leading to older reservoir ages meaning that MRA should be higher in the polar regions (Butzin et al., 2017). Studies also suggest an increase in MRA during the LGM as a result of increased ice cover and decreased ventilation. Butzin et al. (2017) suggest an increase in MRA to approximately 780 ^{14}C during the YD. It is therefore likely that this age model using Marine20 and a *ΔR* = -53 ±36 (figure 5.3 A) underpredicts *ΔR* values in the older (pre-Holocene) sections of the core.

In order to account for the potential increase in *ΔR* prior to the Holocene the Marine20 curve was combined with the local curve for AW (Local20, which will be discussed below) to produce age model B. This model uses the Marine20 calibration curve with *ΔR*= -53 ± 36 for the Holocene and increasing *ΔR* to 500 before 10 000 cal yr BP, to be consistent with higher MRA's found in the northern North Atlantic (Butzin et al., 2017) prior to the Holocene. However, since age model A and B both make use of Marine20 with a constant or single change in *ΔR* , they do not consider the spatial and temporal variability in local MRA and therefore another calibration method using local calibration curves recommended by Heaton et al. (2020) was investigated.

Calibration using Local20

In order to investigate a more objective local calibration method and account for sudden *ΔR* changes associated with climate, I used a method proposed by Alves et al. (2019). This method uses a REST application programming interface (API) to extract local calibration curves from the Hamburg 3-D Large Scale Global Ocean Circulation Model (LSG OGCM) created by Butzin et al. (2017). The model considers wind stress, atmospheric pCO_2 and uses IntCal13 as an input to calculate local ^{14}C values. This model reconstructs the spatial and temporal variability of surface MRAs over the past 50 000 years by considering three different climate scenarios: the present-day scenario representing the Holocene and interstadials and two scenarios based on boundary conditions from the LGM (the glacial scenario and glacial climate scenario) (Butzin et al., 2017). The data needed to run the API are IntCal3, Marine13 and the LSG OCM (with a temporal resolution of 50 years) but in this thesis I used an updated

API (Lefèvere, 2021) for the latest calibration curves, Marine20 and IntCal20. Using this API, a local calibration curve (hereafter referred to as Local20) was extracted from the LSG OGCM.

Initially the coordinates of KH18-10-14-GC-1 (81.25 ° N, 30° E) were used in the LSG OCM, but the coordinates gave an output with a reservoir age of 1500 yr BP for the Holocene (figure 5.4). The exchange of water between the Eurasian basin and the Norwegian and Greenland seas is relatively rapid (on timescales of 10 – 100 years) and it therefore does not make sense that water in the Arctic Ocean would be so old (Östlund et al., 1987). In addition, no dates have been obtained from the Svalbard area so far which are older than 500 ^{14}C years (Mangerud et al., 2006). This could indicate that the model did not accurately represent the influence of AW coming into the area.

KH18-10-14-GC-1 is in a location that is bathed in AW (discussed in section 3.4.3). It was therefore decided that coordinates from a lower latitude site highly influenced by AW would provide a representative local calibration curve. The downstream coordinates for AW (56 ° N, 15° W) were therefore used instead in the API to get the local calibration curve. The MRA for this downstream coordinate for the Holocene was indeed consistent with the dates (MRA) obtained by Mangerud et al. (2006) from the Svalbard area (table 5.2).

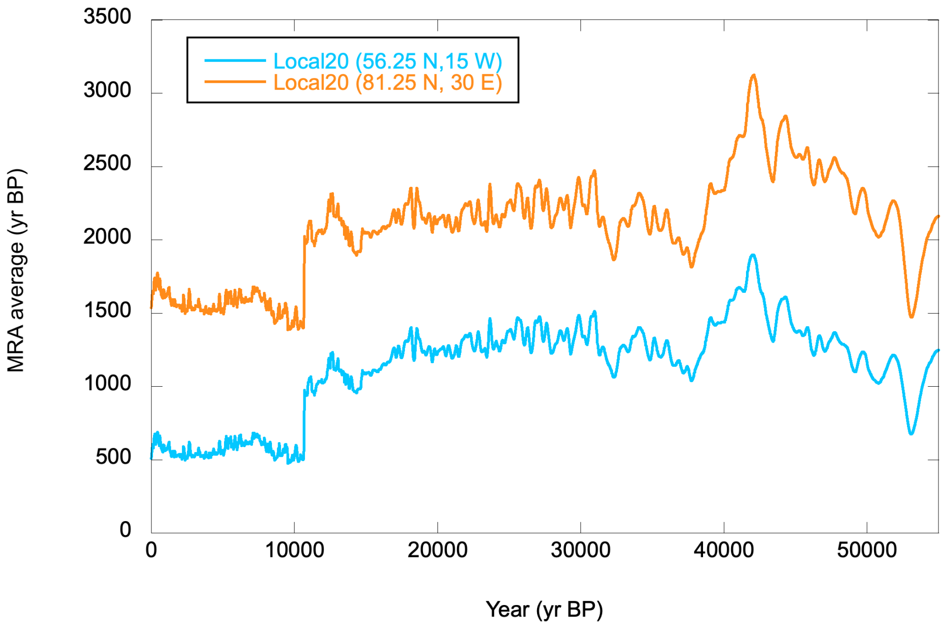

Figure 5.4 The local marine reservoir age average for site 81.25°N, 30°E displaying a very high MRA for the Holocene (orange curve). The local marine reservoir age average for site 56.25°N, 15°W showing a ~ 500 year increase from the Holocene to the Younger Dryas.

The calibration curve output (figure 5.2 Local20 curve for site 56.25°N, 15°W) obtained using the API were formatted appropriately as a text-delimited file so it could be used as a calibration curve in ‘Bacon’. It should be noted that the uncertainty of Marine20 is assumed for the output from the API as the LSG OCM does not output uncertainty (Alves et al., 2019). An age model was obtained for KH18-10-14-GC-1 using the Local20 calibration curve for 56.25°N, 15°W (figure 5.5 and 5.3 C). The average error for the interval of this thesis from the Bacon gaussian age model is ~ 280 years (2σ). The Local20 calibration curve approach gave an almost identical output to curve B which was calibrated using Marine20 and an increased *ΔR* before the Holocene. Local20 (figure 5.5) will be used throughout the rest of this thesis in order to plot variables against age.

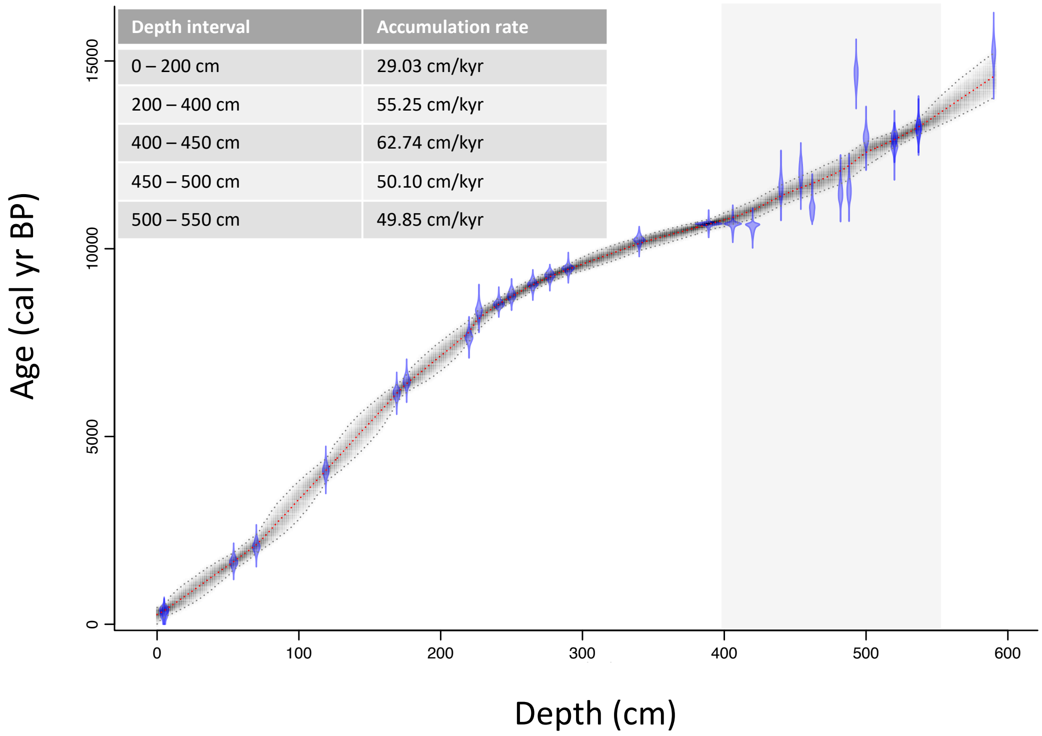

Depth interval	Accumulation rate
0 – 200 cm	29.03 cm/kyr
200 – 400 cm	55.25 cm/kyr
400 – 450 cm	62.74 cm/kyr
450 – 500 cm	50.10 cm/kyr
500 – 550 cm	49.85 cm/kyr

Figure 5.5 ‘Bacon’ age model for core KH18-10-14-GC-1 showing the optimal age-depth model based on the weighted mean age for each depth (red dashed line) and the 95% confidence interval (grey dashed lines). The calibrated ^{14}C dates are shown as transparent blue symbols. Sedimentation rates for important intervals are provided in the table (top left). The interval of the core studied in this thesis is highlighted in grey.

This age model shows lower sedimentation rates in the first 200 cm of the core between 0 – 7000 cal yr BP with an increase from 7000 – 10 000 cal yr BP, indicating overall higher sedimentation rates in the older sections of the core. Sedimentation rates reach a maximum between 400 – 450 cm (10 697 – 11 450 cal yr BP) in the core and then start to decrease slightly. The flattening of the calibrated depths around 400 cm in the core is most likely due to an increase in MRA around 10 000 cal yr BP in the Local20 curve from the LSG OCM, as well as the dates between 389 and 420 cm being very similar.

6. Results

In this section various parameters of core KH18-10-14GC-1, obtained from a depth of 552 m in the Kvitøya Trough, will be presented including: three XRF elemental profiles, magnetic susceptibility, and a brief core description. Thereafter, the high resolution benthic and planktic foraminiferal stable isotope (δ^{18}O and δ^{13}C) records from this core will be presented and described versus depth and age.

6.1 Core description, physical parameters and XRF results

Much of core KH18-10-14GC-1 is relatively homogenous but clear laminations are present towards the deepest part of the core. In figure 6.2 color and x-ray CT images, along with XRF elemental plots are shown for the whole core (0 - 591 cm) to provide context for the observations seen in the core interval used in this thesis (400 - 550 cm). KH18-10-14GC-1 ranges in color from dark grey, to dark and light brown. KH18-10-14GC-1 is light brown-grey between 400 and 420 cm and becomes slightly darker brown/grey between 420 - 510 cm with black patches. From 510 – 550 cm the colors are more variable showing distinct banding of darker and lighter layers. The CT scans do not show any significant features such as burrowing, sedimentary structures, or disturbances apart from small scale bioturbation and shell fragments. What may appear to be lineations in the CT scans are in fact reflections from a part of the core holder. The magnetic susceptibility of KH18-10-14GC-1 varies between 0 and 78 SI x 10^{-5}. Values mainly lie between 0 and 30 SI x 10^{-5} with the exception for two peaks in magnetic susceptibility of 49 SI x 10^{-5} at 582 cm and 78 SI x 10^{-5} at 545 cm. At 509 cm there is a smaller peak of 33 SI x 10^{-5}, after which magnetic susceptibility decreases to a value of 7 at 500cm, the minimum value for this section . For the rest of the study interval, magnetic susceptibility is relatively constant.

XRF core scanning can be used in determining the origin of sediments in a core, with certain elements being indicative of terrigenous origins while others point to biological sources (Rothwell and Croudace, 2015). The XRF elemental profiles of KH18-10-14GC-1 (figure 6.2) show the highest amplitude variability in the interval between 590 and 460 cm. Calcium (Ca), which can be biogenic or detrital in origin, has been normalized by iron (Fe) a typical indicator of terrigenous sediment supply (Rothwell and Croudace, 2015). The Ca/Fe ratio typically represents the biogenic carbonate to detrital clay ratio (Rothwell and Croudace, 2015). Ca/Fe displays high amplitude oscillations between 590 and 537 cm ranging from 0.05 to 0.12. Ca/Fe then starts to decrease from a peak of 0.12 (at 537 cm) to 0.03 (at 504 cm) after which it increases rapidly reaching 0.08 by 499 cm. Ca/Fe remains high and gradually increases until 484 cm in the core. Subsequently, it decreases rapidly again until it stabilizes around 464 cm, remaining relatively constant throughout the rest of the core, displaying a gradually decreasing trend.

Potassium (K) which is an indicator of terrestrial sediment sources (in specific siliclastics) (Rothwell and Croudace, 2015), displays high variability between 590 and 560 cm. During the interval used for this thesis and for the remainder of the core, K exhibits a steadily decreasing trend (decreasing from ~3500 to 500) indicating a decrease in terrestrial sediment supply throughout this interval, with the highest terrestrial sedimentation at ~ 560 cm in the core. The presence of manganese (Mn) in sediments in the Arctic has been found to be a good climate or process indicator (Löwemark et al., 2016). In KH18-10-14GC-1, Mn displays one major peak where Mn increases rapidly from 508 cm reaching a maximum of 2186 at 499 cm and thereafter decreases rapidly back down to ~700 at 489 cm. This is seen in the core as a dominance of blue-grey, platy balls of material with very scarce foraminifera (figure 6.1). Apart from this peak, Mn displays a relatively constant profile throughout the core with values falling between 400 and 1000.

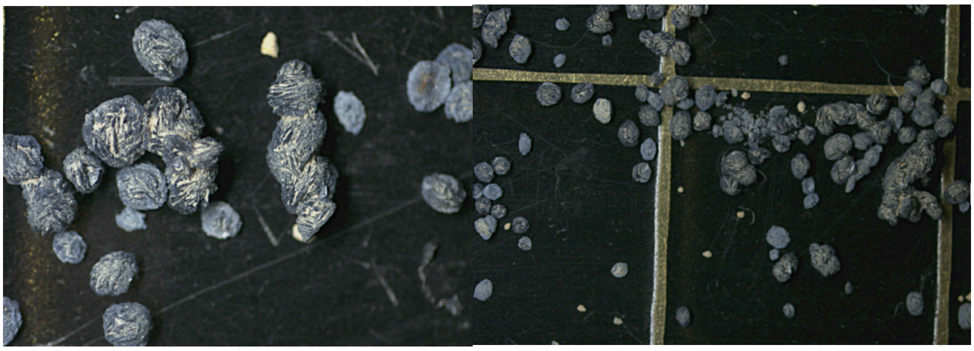

Figure 6.1 Blue-grey fragments of manganese > $150\mu g$ from the interval 501-502 cm in KH18-10-14GC-1 under higher magnification 4x (left) and lower magnification 2x (right)

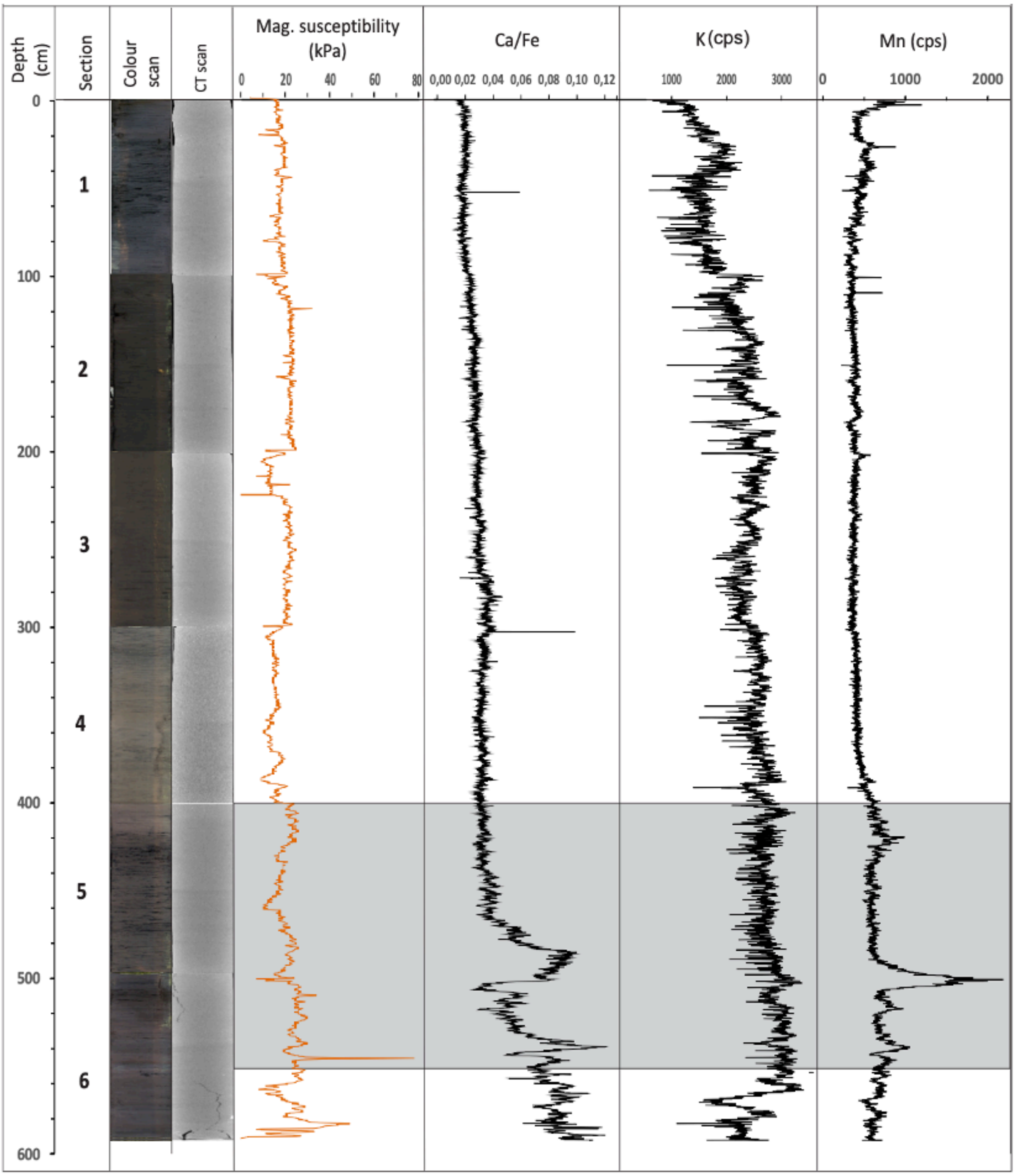

Figure 6.2 XRF and CT images of KH18-10-14GC-1 shown alongside the magnetitic susceptibility of core KH18-10-14-GC-1 and three XRF elemental profiles; Ca/Fe, K, and Mn. The section of the core that was used in this thesis is highlighted in grey.

6.2 Oxygen isotope results

As discussed in detail in section 4.3.1 the $\delta^{18}O$ of foraminiferal calcite is a function of both ocean temperature (1‰ corresponds to a ~ 4.3°C change in ocean temperature) and $\delta^{18}O$ of seawater ($\delta^{18}O_{sw}$) (Fairbanks, 1989) and is therefore very useful for reconstructing changes in past water masses. $\delta^{18}O_{sw}$ also has a regionally linear relationship with salinity due to evaporation and precipitation influences on both salinity and $\delta^{18}O_{sw}$. The regional relationship in the north-western Barents Sea is 0.55‰ per 1 change in salinity (LeGrande and Schmidt, 2006). The variability in $\delta^{18}O$ primarily reflects changes in ocean temperature and salinity but could also be affected to a smaller degree by global ice volume and vital effects.

In this thesis stable isotope analysis of oxygen and carbon isotopes was carried out on 371 foraminifera samples (including replicates) (152 *N. pachyderma* samples, 95 *N. labradorica* samples and 124 *C. neoteretis* samples) picked from KH18-10-14GC-1. Repeated measurements were done on every sample from 400 – 440 cm, and every 4cm between 440-550 cm, where foraminifera were abundant enough. In total 96 replicates were analyzed. Below, the planktic and benthic oxygen isotope results (see Appendix A for all isotope data) have been plotted versus depth and age, respectively. The ages are the mean ages obtained from ‘Bacon’ using the age model discussed in Chapter 5.

6.2.1 Planktic oxygen isotope results

The $\delta^{18}O$ of *N. pachyderma* represents changes in near surface water properties since these foraminifera generally live in the upper 25 – 280 m of the water column (Carstens and Wefer, 1992; Greco et al., 2019). In this thesis *N. pachyderma* has not been corrected for vital effects because this species calcifies close to equilibrium with sea water (Ivanova et al., 2008; Kristensen et al., 2013; Chauhan et al., 2016). In figure 6.3A the replicate $\delta^{18}O$ values of *N. pachyderma* show close agreement with the original results obtained from the first runs. The overall standard deviation calculated for the replicates is ± 0.11‰ (see Appendix B for statistics) which is higher than the internal precision of the machine of 0.06‰ for $\delta^{18}O$. The *N. pachyderma* $\delta^{18}O$ record shows high variability, well above the uncertainty, with $\delta^{18}O$ fluctuating by almost 2‰. The major feature in this record is a low $\delta^{18}O$ interval spanning 500 – 478 cm in the core. It is unlikely that such a large feature (over 20 cm in the core) would have been majorly disrupted by bioturbation. To uncover what this event of lowest $\delta^{18}O$ may mean and when it occurred, δ^{18}O is plotted versus age below (figure 6.3B). This record will be discussed from the oldest to youngest section.

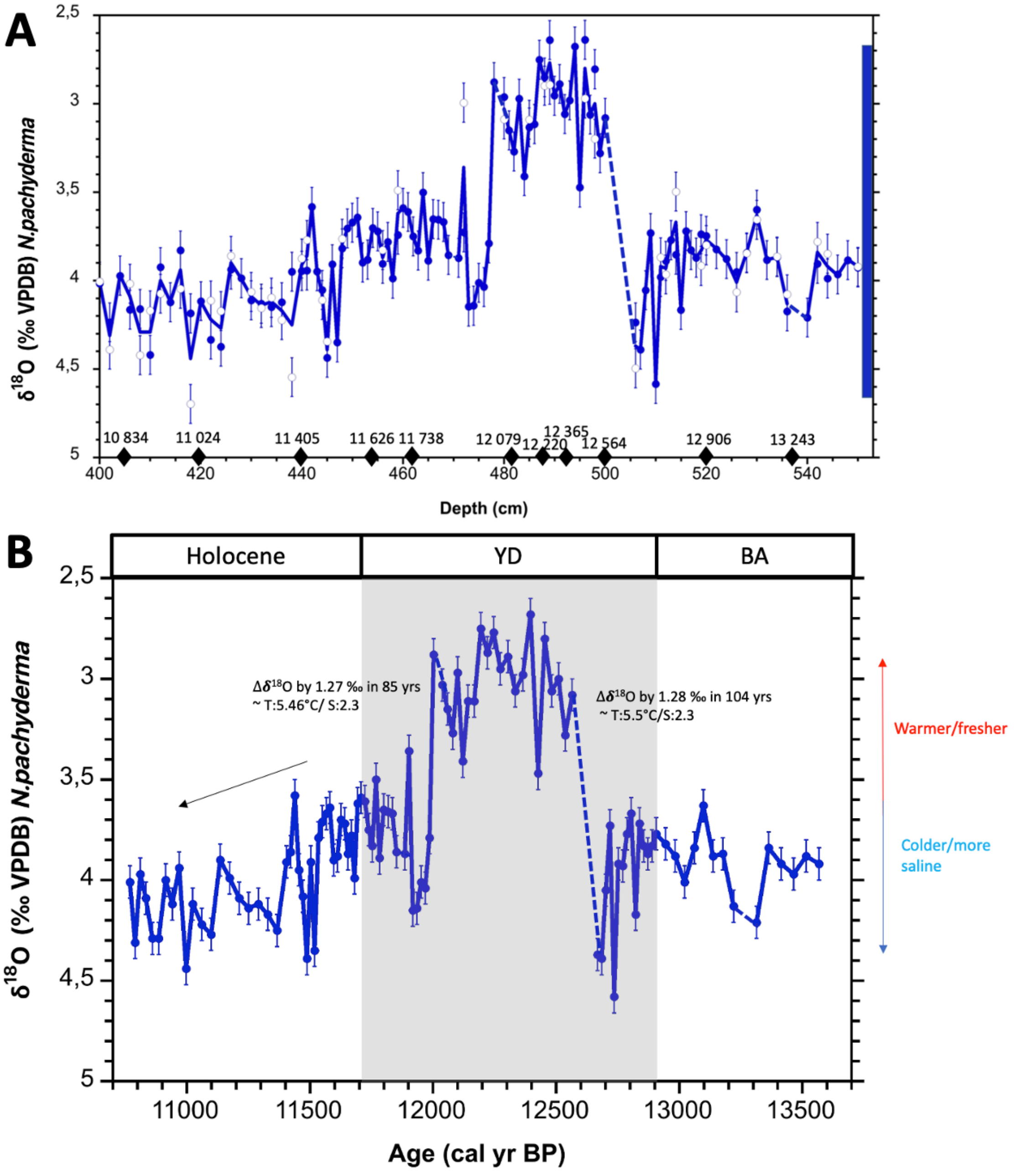

Figure 6.3 A) The δ^{18}O measurements of *N. pachyderma* from 400 to 550 cm in KH18-10-14GC-1. The filled circles represent the first run results, and the open circles are the replicates. The dark blue curve connects the mean δ^{18}O values through the record and the blue bar on the right shows the range of this curve (1.9‰). The error bars represent the overall standard deviation of the replicates (SD = ± 0.11‰). The black diamonds on the x-axis denote the calibrated AMS ^{14}C dates. B) The mean δ^{18}O values of *N. pachyderma* versus age. The dark blue line joins the mean values of the replicates at each depth. The error bars show the standard error of the mean (SEM = ±0.08‰). The labeled blocks represent the early Holocene, Younger Dryas (YD) and Bølling-Allerød (B/A). For both curves the y-scale is inverted and the dashed blue lines mark intervals where *N. pachyderma* is absent.

During the B/A (550 – 511 cm), δ^{18}O values alternate between 3.63 and 4.17‰. At the onset of the YD there is an increase in δ^{18}O to 4.58‰ at ~12 700 cal yr BP (510 cm). This is followed by a brief decrease and increase again with magnitudes of ~ 0.5‰. Subsequently there is an ~ 86 year period (505 – 500 cm) where *N. pachyderma* is absent entirely. This barren interval during the YD is followed by a period of very low δ^{18}O values (2.68 – 3.28‰) between ~12 600 and 12 000 cal yr BP (500 - 478 cm). At the onset of this distinctly low δ^{18}O interval, δ^{18}O values decrease by 1.28‰ in 104 years, although it could be even faster since it spans the interval where no foraminifera are present. The 1.28‰ decrease is equivalent to an increase in temperature of as much as 5.5°C or a decrease in salinity of 2.3. The YD δ^{18}O minimum reaches its lowest value of 2.68‰ at ~12 400 cal yr BP (494 cm) and remains low for ~ 500 years; representing a total $\Delta\delta^{18}$O decrease of up to ~1.9‰ relative to pre YD values. This maximum change represents a warming of 8.17°C or decrease in salinity of 3.45.

Towards the end of the YD, the peak in δ^{18}O is followed by a sharp increase in δ^{18}O at ~12 000 cal yr BP (477 cm) where values rise by 1.27‰ in 85 years reaching 4.15‰ by 11 918 cal yr BP. This could mean there was a decrease in temperature of 5.46°C or an increase in salinity of 2.3 in the late YD. This decrease is followed by a brief return to lower values (3.36‰ at 11 900 cal yr BP), whereafter the last ~1000 years of the record (spanning ~11 700 to 10 700 cal yr BP) display an overall increasing trend. Between 11 700 and 10 700 cal yr BP δ^{18}O fluctuates between 4.44 and 3.35‰.

6.2.2 Benthic oxygen isotope results

The two benthic foraminiferal species which were used for stable isotope analysis in this thesis are *C. neoteretis* and *N. labradorica*. While *C. neoteretis* provides an almost continuous isotopic record, *N. labradorica* is absent for a large part of the interval. For this reason, there will be a greater focus on *C. neoteretis*. Changes in the δ^{18}O of these species are likely to indicate changes in bottom water and pore water characteristics. There is some discrepancy as to whether *C. neoteretis* should be corrected for vital effects or not. Some studies do not correct for disequilibrium effects since *C. neoteretis* calcifies close to equilibrium with sea water (Jansen et al., 1988; Kristensen et al., 2013; Ivanova et al., 2019), while others agree that *C. neoteretis* precipitates close to equilibrium but with a slight offset between 0.16‰ (Chauhan et al., 2016) and 0.504‰ (Lubinski et al., 2001). Due to the lack of consensus as to what value to use for the offset, *C. neoteretis* will not be corrected for vital effects in this thesis. The replicates of *C. neoteretis* δ^{18}O reproduce well (figure 6.4A). *C. neoteretis,* similarly to *N. pachyderma*, shows high variability in δ^{18}O values with a range of 2.49‰. A distinctly low interval of δ^{18}O is observed between 498 and 480 cm.

During the B/A (13 600 cal yr BP to 12 900 cal yr BP) δ^{18}O values alternate frequently between 4.39‰ and 5.29‰. At the beginning of the YD, values increase from 4.32‰ at 12 800 cal yr BP (512 cm) to 5.4‰ at 12 700 cal yr BP (506 cm). After this increase, *C. neoteretis* is absent until 501 cm in the core. The barren interval is followed by a sharp decline in δ^{18}O. Values decrease by 2.04‰ in 104 years reaching 3.36‰ by ~12 500 ca yr BP. This sharp transition is almost identical in timing and rate, but of even larger magnitude, to that seen in the *N. pachyderma* record (figure 6.3). This decrease in δ^{18}O could indicate an increase in water temperature of 8.77°C or decrease in salinity by 3.7 occurring concurrently with the warming seen in the planktic record. This is an extremely high temperature increase for bottom water temperatures. The δ^{18}O values remain low (alternating between 3.32 and 4.03‰) for ~500 years until 480 cm in the core.

During the late YD (ca. 12 000 cal yr BP) δ^{18}O values start to increase again, reaching a high of 5.05‰ by 11 900 cal yr BP. For the remainder of the YD δ^{18}O values remain relatively high, not going lower than 4.32‰. This indicates that during the late YD water temperatures could have decreased by 5.2°C or salinity could have increased by 2.21 (change in δ^{18}O of 1.22‰). During the early Holocene, values alternate between 4.23‰ and 5.81‰, showing an overall slightly increasing trend. The highest δ^{18}O value of 5.81‰ is reached at 11 000 cal yr BP (418 cm).

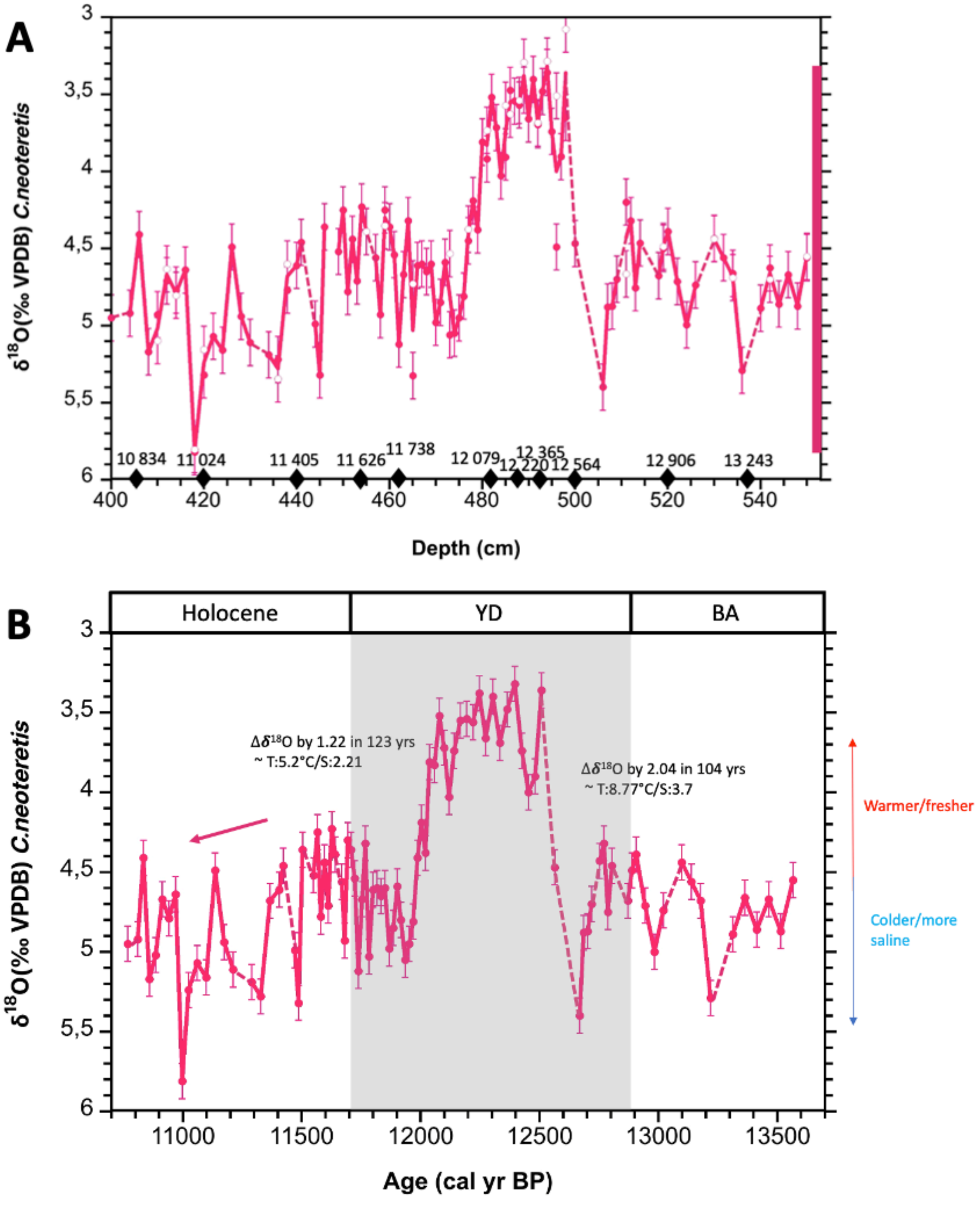

Figure 6.4 A) The δ^{18}O measurements of *C. neoteretis* versus depth for KH18-10-14GC-1. The solid pink circles represent the δ^{18}O values obtained from the first runs and the hollow pink circles show the replicate values. The solid pink curve traces the mean δ^{18}O values at each depth. The overall standard deviation calculated for all replicates is ± 0.15‰ (pink error bars). The pink bar shows the range of the mean δ^{18}O values. The black diamonds on the x-axis denote the AMS ^{14}C dates converted to calibrated radiocarbon ages. B) The mean δ^{18}O of *C. neoteretis* versus age for KH18-10-14GC-1. The pink line connects the mean δ^{18}O values at each depth. The pink error bars represent the SEM = 0.11. The labeled blocks represent the early Holocene, Younger Dryas (YD) and Bølling Allerød (B/A). For both curves the dashed pink lines show intervals where *N. pachyderma* is absent and the y-axis is inverted.

The δ^{18}O record of *N. labradorica* also displays high variability, although not quite as high as for the other two species, with a range of 1.58‰ (figure 6.5A). The variability is higher than the standard deviation of the replicates of ± 0.09‰. The record is not continuous since *N. labradorica* disappears entirely at the beginning of the Younger Dryas (12 944 cal yr BP) and makes an appearance again during the late Younger Dryas (12 220 cal yr BP). It was therefore not possible to obtain δ^{18}O measurements of *N. labradorica* for the interval of 522 and 488 cm. *N. labradorica* is also absent for numerous shorter intervals of the core and due to the lack of continuity of the record the trends in δ^{18}O cannot be easily seen and discussed. The outlier marked with a star at 436 cm (figure 6.5A) is a repeat value almost 2‰ higher than the original value and has therefore been excluded for the rest of the thesis.

During the B/A the *N. labradorica* δ^{18}O values alternate between 4.51 and 5.14‰. Just before the onset of the YD, *N. labradorica* disappears and is absent for a large part of the YD. Soon after its reappearance at 12 200 cal yr BP, δ^{18}O reaches a minimum of 4.11‰ at 12 000 cal yr BP (479 cm). Thereafter there is a rapid increase in δ^{18}O of 1.05‰, reaching 5.16‰ by 11 970 cal yr BP (476 cm). This could mean that towards the end of the YD there was a decrease in ocean temperatures of approximately 4.52°C or an increase in salinity of 1.9. The remainder of the YD has quite high variability in δ^{18}O but shows an overall decreasing trend towards lower values, reaching a minimum of 4.19‰ at 11 700 cal yr BP. The early Holocene displays an overall increasing trend in δ^{18}O. The highest value in the whole record of 5.69‰ is reached at 10 800 cal yr BP (402 cm).

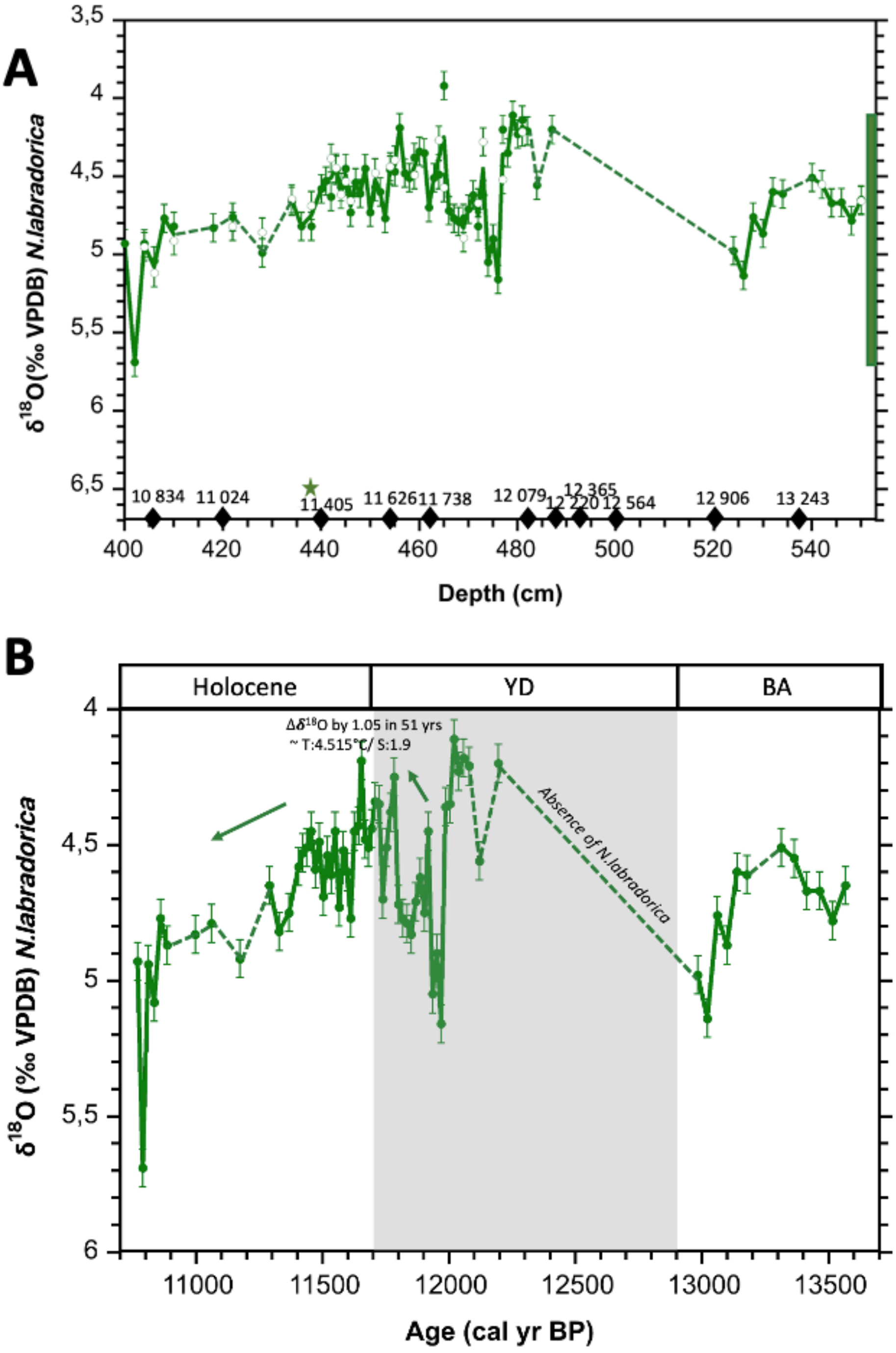

Figure 6.5 A) The $\delta^{18}O$ record of *N. labradorica* versus depth for core KH18-10-14GC-1. The solid green circles represent the $\delta^{18}O$ values obtained from the first runs and the hollow green circles are the repeat values. The solid green curve connects the average $\delta^{18}O$ values at each depth. The error bars represent the overall standard deviation of the replicates (SD = 0.09). The green bar shows the range of the mean $\delta^{18}O$ values. The green star is an outlier which is removed after this plot. The black diamonds on the x-axis denote the AMS ^{14}C dates converted to calibrated radiocarbon ages. B) The mean $\delta^{18}O$ of *N. labradorica* versus age from KH18-10-14GC-1. The green line connects the mean $\delta^{18}O$ values at each depth. The green error bars show the SEM which is equal to 0.07‰. The labeled blocks represent the early Holocene, Younger Dryas (YD) and Bølling Allerød (B/A). The arrows indicate general trends in $\delta\ ^{18}O$. For both curves the y-axis decreases vertically and the dashed green lines indicate intervals where *N. labradorica* is absent.

6.2.3 Interspecies comparison

The distinct minimum in δ^{18}O values associated with the YD interval of the core is evident in both planktic and benthic records from KH18-10-14GC-1. Both the *N. pachyderma* and *C. neoteretis* δ^{18}O records display a large decrease in δ^{18}O during the early YD lasting approximately 500 years. Both curves first show an increase in δ^{18}O at the beginning of the YD, around 12 600 - 12 700 cal yr BP, followed by a rapid decrease in δ^{18}O (of 1.28‰ and 2‰, for *N. pachyderma* and *C. neoteretis* respectively) in ~104 years. After 12 500 cal yr BP both the *N. pachyderma* and *C. neoteretis* δ^{18}O records remain low for ~500 years while *N. labradorica* is absent. The absence of *N. labradorica* combined with the low δ^{18}O records could point to a change in water masses/productivity in both the subsurface and deep water. All three records see a return to higher δ^{18}O around 12 000 cal yr BP. In figure 6.6 the mean ages for the calibrated AMS ^{14}C dates and error bars ($2\ \sigma = \sim 280$ years) from the Bacon gaussian age model are shown at the bottom of the plot for the dated intervals. The distinctly low δ^{18}O interval seen in this record clearly falls within the YD even within the 2 sigma error bars. This means that according to the uncertainty of our age model this period of low δ^{18}O could not have occurred during the B/A or Holocene. The end of the YD displays generally decreasing δ^{18}O values, followed by an increasing trend for the remainder of the early Holocene. Where *N. labradorica* is present its δ^{18}O values mostly overlap with the *C. neoteretis* δ^{18}O values. The *N. pachyderma* δ^{18}O values have a consistent average offset of ~ -0.89‰ relative to *C. neoteretis*, which is likely due to *N. pachyderma* in the Arctic Ocean having a constant offset from δ^{18}O of ~ 1‰ (Duplessy et al., 2001).

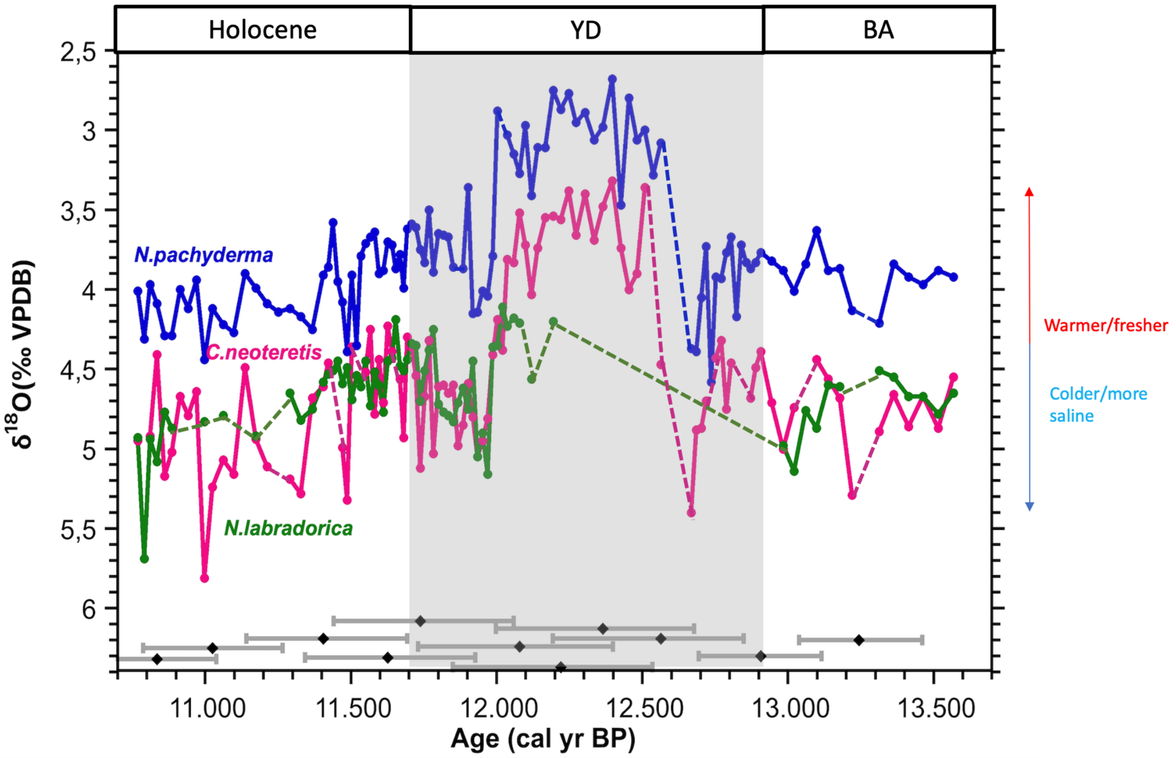

Figure 6.6 An interspecies comparison of the δ^{18}O records of *N. pachyderma, C. neoteretis* and *N. labradorica* versus age from KH18-10-14GC-1. The black diamonds show the mean ages for the calibrated AMS ^{14}C dates and error bars (2 σ) from the 'Bacon' gaussian age model. The solid lines show the average δ^{18}O values of *N. pachyderma* (blue), *C. neoteretis* (pink) and *N. labradorica* (green). The dashed lines show where the respective species are absent. The labeled blocks represent the early Holocene, Younger Dryas (YD) and Bølling Allerød (BA). The y-axis scale is inverted.

6.3 Carbon isotopes results

Carbon isotope values of foraminiferal calcite are good indicators of productivity in the ocean being a result of the balance between photosynthesis and remineralization of organic matter (section 4.3.2). Different water masses also have specific δ^{13}C values therefore making δ^{13}C a useful palaeoceanographic proxy. Stable isotope analysis on the MAT253 provides δ^{18}O and δ^{13}C results simultaneously and therefore the same number of δ^{13}C values were obtained as discussed in section 6.2. The δ^{13}C values have not been corrected for vital effects due to the lack of consensus of offset values. Additionally, it is not necessary to correct for vital effects when looking at relative (not absolute) changes, as these should not be affected by vital effects. In section 6.3.1 the planktic and benthic carbon isotope results have been plotted versus age.

6.3.1 Planktic carbon isotope results

The planktic carbon isotope record represents changes of near-surface water properties. The δ^{13}C measurements of *N. pachyderma* have a range of 0.6‰, alternating frequently above and below 0‰ without any clear trend. The oscillations in the δ^{13}C record are for the most part not much larger than the error bars (standard deviation of the replicates = ± 0.09‰), therefore making it difficult to tell if the variability is greater than the uncertainty. The highest mean δ^{13}C value of 0.22‰ is reached at approximately 12 000 cal yr BP while the lowest value of - 0.38‰ is reached 160 years later at 11 900 cal yr BP. This decrease in δ^{13}C corresponds with the sharp increase in *N. pachyderma* δ^{18}O values (figure 6.3).

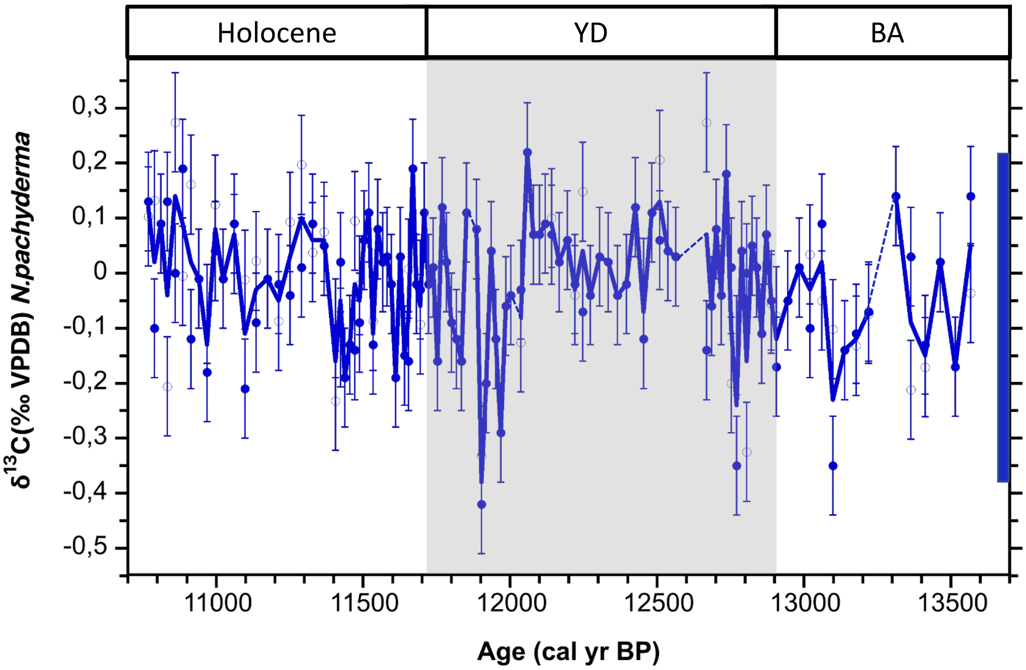

Figure 6.7 The δ^{13}C measurements of *N. pachyderma* versus age. The dark blue circles are the results from the first runs and the hollow circles are the repeat values. The dark blue line joins the mean values of the replicates at each depth and the dashed blue lines mark intervals where *N. pachyderma* is absent. The blue error bars represent the overall standard deviation of ±0.09‰. The dark blue bar indicates the range of the mean δ^{13}C measurements. The labeled blocks represent the early Holocene, Younger Dryas (YD) and Bølling-Allerød (BA).

6.3.2 Benthic carbon isotope results

Benthic carbon isotopic results are indicative of bottom water and pore water conditions. Two benthic foraminifera were used to perform stable isotope analysis in this thesis: *C. neoteretis* and *N. labradorica.* As both species are infaunal their δ^{13}C values are likely to reflect the δ^{13}C of the pore water which is more depleted in ^{13}C due to organic matter respiration in the sediment. In figure 6.8 *C. neoteretis* is plotted versus age. The average δ^{13}C values recorded by *C. neoteretis* lie within the range of - 0.11 to -1.05‰. There are two major peaks in δ^{13}C which are well above the uncertainty, one occurring during the B/A and one during the YD. During the B/A peak in δ^{13}C of - 0.22‰ occurs at 13 220 cal yr BP. This is followed by decrease in δ^{13}C until the onset of the YD. The YD displays a gradually increasing trend with values increasing from - 0.86‰ to a maximum of - 0.11‰ at 12 100 cal yr BP. The peak in δ^{13}C corresponds to the minimum values seen in the *C. neoteretis* δ^{18}O record (figure 6.4).

After 12 100 cal yr BP δ^{13}C begins to decrease rapidly reaching - 1.02‰ at 12 000 cal yr BP. This occurs simultaneously with the rapid increase in δ^{18}O values of *C. neoteretis* (figure 6.4), therefore displaying an inverse trend to δ^{18}O. For the remainder of the YD (12 000 to 11 700 cal yr BP), δ^{13}C does not show as much variability displaying an overall slightly decreasing trend, whereas from the onset of the Holocene δ^{13}C values show slightly higher amplitude variability with an overall increasing trend. From approximately 12 000 cal yr BP, the δ^{13}C and δ^{18}O *C. neoteretis* records display similar trends and no longer inverse relationships. There is outlier in the δ^{13}C record at 12 509 cal yr BP with a value of -1.28‰ (1.04‰ lighter than the other measurement at this depth) which has been marked with a star and has not been included in the mean or standard deviation calculations.

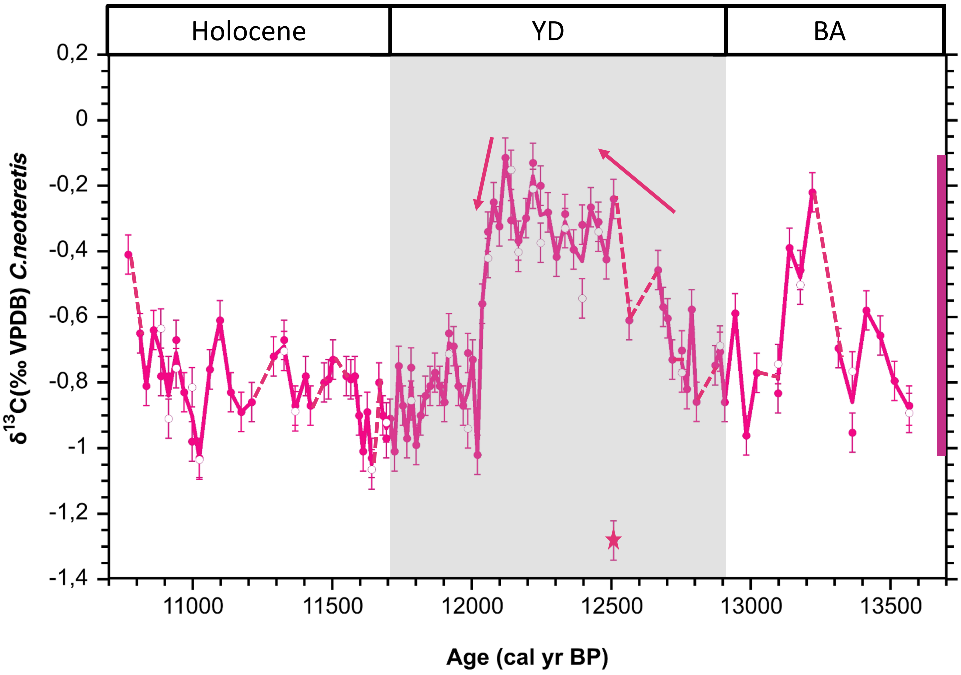

Figure 6.8 The δ^{13}C values of *C. neoteretis* versus age. The pink circles are the results from the first runs and the hollow circles are the repeat values. The pink line joins the mean value of the replicates at each depth and the dashed pink lines mark intervals where *C. neoteretis* is absent. The pink error bars show the overall standard deviation of the replicates of ±0.06‰. The pink bar indicates the range of the mean δ^{13}C measurements. The labeled blocks represent the early Holocene, Younger Dryas (YD) and Bølling-Allerød (BA). The arrows indicate general trends in δ^{13}C. The pink star represents an outlier.

The δ^{13}C record obtained for *N. labradorica* (for the intervals where it was present) shows similar trends to the *C. neoteretis* δ^{13}C record. During the B/A δ^{13}C values lie between - 0.93 and - 1.67‰. A peak in δ^{13}C of - 0.54‰ occurs during the YD at 12 000 cal yr BP which is followed by a rapid decrease in δ^{13}C after 11 970 cal yr BP. This peak once again displays an inverse profile to *N. labradorica* δ^{18}O profile (figure 6.5), similar to what is seen in the *C. neoteretis* record. This decreasing trend occurs later than that seen in the *C. neoteretis* δ^{13}C profile and continues until approximately the end of the YD (11 800 cal yr BP). During the Holocene the *N. labradorica* δ^{13}C values show high variability and around 11 300 cal yr BP δ^{13}C begins to decrease to the minimum of - 2.37‰, which is reached at 11 000 cal yr BP.

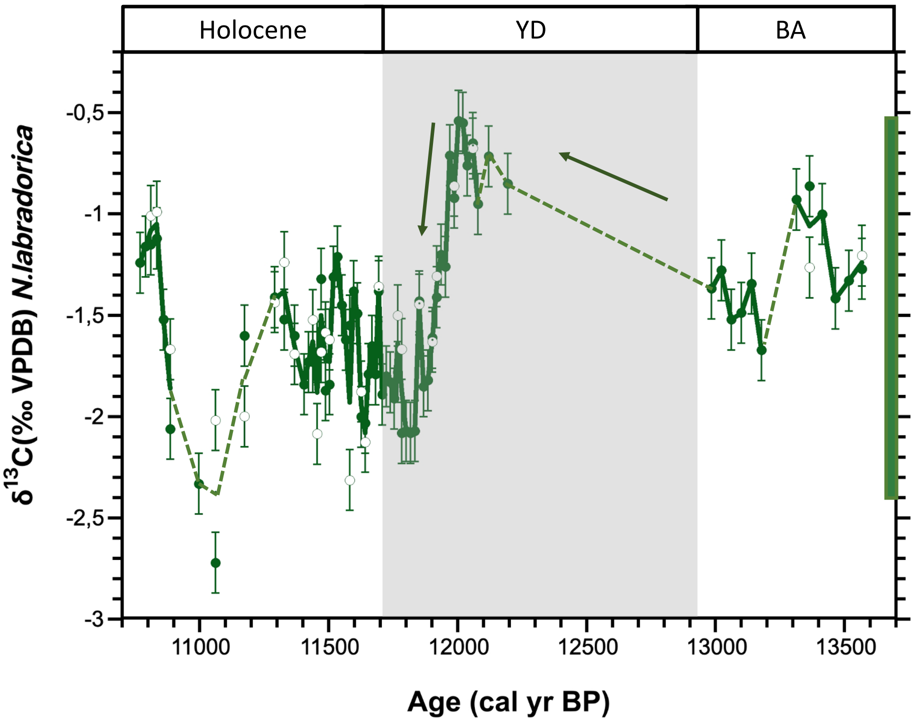

Figure 6.9 The δ^{13}C values of *N. labradorica* versus age for KH18-10-14GC-1. The green solid circles are the results from the first runs and the hollow circles are the repeat values. The green line joins the mean value of the replicates at each depth and the dashed green lines mark intervals where *C. neoteretis* is absent. The green error bars represent the overall standard deviation of the replicates of ±0.15‰. The green bar shows the range of the mean δ^{13}C values. The arrows indicate general trends in δ^{13}C. The labeled blocks represent the early Holocene, Younger Dryas (YD) and Bølling-Allerød (BA).

6.3.3 Interspecies comparison

Both of the benthic δ^{13}C records exhibit an increasing trend in δ^{13}C during the YD with values increasing by ~1‰ from 12 900 to 12 000 cal yr BP. The peak in benthic δ^{13}C is followed by a rapid decrease towards the end of the YD occurring simultaneously with the increase seen in the planktic and benthic δ^{18}O records (figure 6.6). The planktic *N. pachyderma* δ^{13}C isotopic record does not show the same clear trends seen in the benthic records. Both benthic records also have lower δ^{13}C values than *N. pachyderma,* with δ^{13}C values lying below 0‰. The lower δ^{13}C values of *N. labradorica* relative to *C. neoteretis* are likely due to *N. labradorica* being a deeper infaunal species.

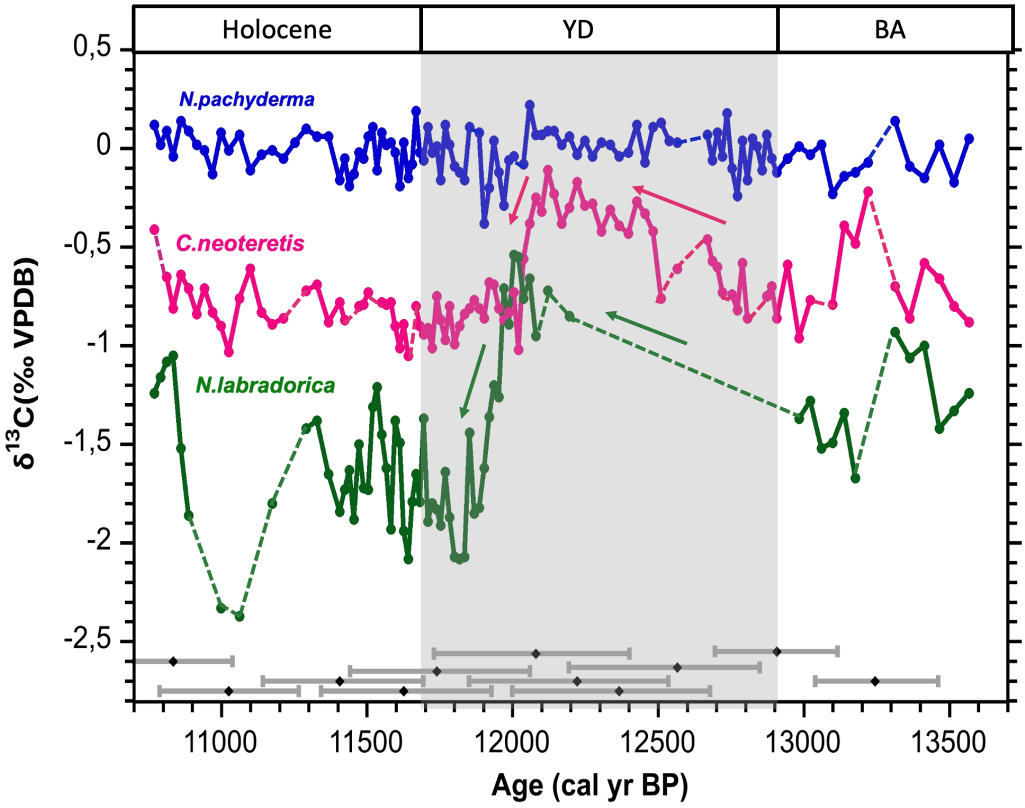

Figure 6.10 An interspecies comparison of the δ^{13}C values of *N. pachyderma, C. neoteretis* and *N. labradorica* versus age for KH18-10-14GC-1. The black diamonds show the mean ages for the calibrated AMS ^{14}C dates and error bars (2 σ) from the 'Bacon' gaussian age model. The solid lines show the average δ^{13}C values of *N. pachyderma* (blue), *C. neoteretis* (pink) and *N. labradorica* (green). The dashed lines show where the respective species are absent. The labeled blocks represent the early Holocene, Younger Dryas (YD) and Bølling Allerød (BA).

7. Discussion

This thesis set out to improve our understanding of how the inflow and properties of AW into the Arctic have varied since the deglaciation, with a focus on the the most recent high-magnitude, abrupt climate change event—the Younger Dryas (YD). The high variability seen in the stable carbon and oxygen isotope records from the Kvitøya Trough (core KH18-10-14GC-1) indicate significant changes in water mass properties (temperature, salinity, and productivity) during the B/A, YD and into the early Holocene. Although many of the studies investigating how AW influence changed during the deglaciation interpret the properties of AW to represent its strength (e.g., warmer AW is due to stronger inflow), it is important to distinguish that these are not the same thing. There are numerous sources of evidence in this thesis to suggest that AW was continuously inflowing into the Arctic during the deglaciation. These include the almost constant presence of *C. neoteretis* which is associated with AW, relatively constant δ^{13}C values throughout the interval indicating that water masses did not change significantly, as well as the relatively high δ^{18}O compared to Arctic Water suggesting a persistent AW influence. Due to this evidence, combined with previous studies suggesting continuous AW influence west of Svalbard (e.g., Rasmussen et al., 2007), I will focus the discussion mainly on the variability in AW properties instead of on AW inflow strength or distribution.

To my knowledge there is currently only one other stable isotope record which covers the whole YD from the Kvitøya Trough (Ivanova et al., 2019). Based on this previous information it has remained somewhat ambiguous how the properties of AW inflow changed during the YD in the Kvitøya Trough and surrounding areas. In particular, the nature and origin of subsurface temperature response of the North Atlantic during the YD, relative to that occurring during other stadial events (e.g., Heinrich stadial 1), remains debated (He et al., 2020). This site is appropriately located for documenting the changes in AW inflow into the Artic, making the high resolution stable isotope record obtained in this thesis vital for better understanding the properties of AW flowing into the Arctic during the deglaciation. In this chapter I interpret my results and discuss them in relation to other studies from the Kvitøya Trough and the broader region. In addition, the variability in carbon and oxygen stable isotopes will be compared to proxies for overturning circulation and sea ice, and the potential mechanisms giving rise to the changes will be explored, as well as their potential similarities to other abrupt climate events.

7.1 The significance of the oxygen isotope records

Variability in $\delta^{18}O$ of foraminifera ($\delta^{18}O_c$) indicates changes in ocean temperature (1‰ corresponds to ~ 4.3°C temperature change) as well as the $\delta^{18}O$ of seawater ($\delta^{18}O_{sw}$), which covaries with salinity (approximately 0.55‰ per 1 change in salinity) and global ice volume (subchapter 4.3.1). It has been shown using an oxygen-isotope enabled Earth System Climate Model that benthic $\delta^{18}O_c$ values from the North Atlantic are mainly affected by temperature, with meltwater and changes in circulation having only a small impact on $\delta^{18}O_c$ (Bagniewski et al., 2015). The only exception to this is during the recovery of the AMOC where $\delta^{18}O_c$ decreases at depth due to the entrainment and advection of low $\delta^{18}O$ values into the Arctic (Bagniewski et al., 2015) and newly formed deep waters. A modern analogue from the Franz Victoria and St. Anna troughs showed that benthic and planktic $\delta^{18}O_c$ values from these areas are more strongly controlled by temperature than by salinity (Lubinski et al., 2001) (figure 7.1). This is also because *N. pachyderma* generally calcifies below the surface water where temperature has a stronger influence on isotopic composition (Lubinski et al., 2001). In this region at depths of around 460 – 633 m, salinity varies over a relatively narrow range < 0.2 and regional temperatures vary more spanning a range of around 3°C. Thus, the regional temperature variability would drive much larger changes in equilibrium $\delta^{18}O_c$ than salinity (Lubinski et al., 2001). However, the $\delta^{18}O_c$-salinity relationship could have been significantly different during the deglaciation when large amounts of (low $\delta^{18}O$) fresh water were being released due to ice sheet melting (Lubinski et al., 2001) and ice sheets would likely have more negative $\delta^{18}O$ values than present day freshwater sources. If this strengthened the local halocline, the freshwater influence on planktonic foraminifera might have been stronger, as is observed in much of the Arctic away from AW influence (Spielhagen and Erlenkeuser, 1994). According to Lubinski et al. (2001), fresh water could have penetrated down to 100-200 m depths during this period. A striking feature in the record produced for this thesis, however, is that a similar reduction in $\delta^{18}O_c$ values is seen in the benthic species, representing a paleo depth of ~ 600 m during the YD (Lohne et al., 2007; Schomacker et al., 2019).

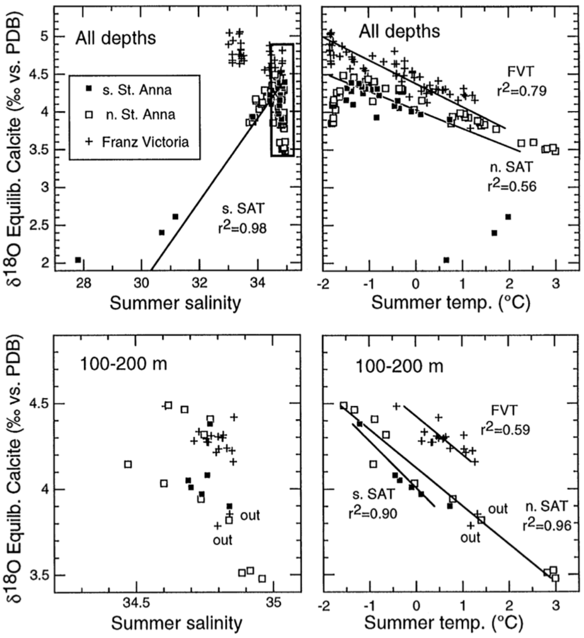

Figure 7.1 The modern relationship of $\delta^{18}O_c$ to summer salinity and temperature in the Franz Victoria and St. Anna troughs, showing that temperature has a stronger control on $\delta^{18}O_c$ than salinity (Lubinski et al., 2001).

In this thesis a change of up to ~2‰ is seen in both the planktic and benthic $\delta^{18}O_c$ records (figure 7.3). As *N. pachyderma* generally resides between 25 – 280 m (average depth of 100 m) (Carstens and Wefer, 1992; Greco et al., 2019) and usually calcifies between 100 and 200 m, it is most likely that this species records the properties of AW found between 100 and 600 m (Lubinski et al., 2001; Carstens and Wefer, 1992). It is, however, still possible that this species could calcify in the polar surface water which occupies the top 50 m of the water column in the modern ocean. The benthic $\delta^{18}O$ records are representative of hydrographical conditions of bottom water overlying the seafloor (Duplessy et al., 2005), which in this case is a depth of ~600 m. Therefore, both the planktic and benthic species used in this thesis are likely to be recording the properties of the upper and lower reaches of AW influence. Bottom water salinity in the Barents Sea is relatively constant and shows small lateral gradients such that benthic $\delta^{18}O$ variability is more likely to be due to changes in temperature (Kristensen et al., 2013 and references within).

To account for the whole ocean isotopic change related to ice volume and sea level changes Fairbanks (1989) showed that $\delta^{18}O_{sw}$ values need to be corrected by a maximum of 0.011‰ per meter of global glacial sea level change. The time interval covered in this thesis is ~3000 years, spanning the end of warm B/A period, though the YD and into the early Holocene.

Between 16 500 and 8200 cal yr BP global sea level rose at an average rate of 12 m per 1000 years (Lambeck et al., 2014). It is therefore possible that sea level changed by ~ 30 m during our interval of interest. In this thesis $\delta^{18}O_c$ has not been corrected for changes in ice volume/sea level, since this correction makes use of a global sea level curve while the $\delta^{18}O_{sw}$ signal due to ice volume changes is inherently transient, initially influencing the region where melting occurs much stronger than other regions until melting ceases and the signal can be mixed throughout the ocean. Thus, whole ocean averaging is only accomplished on global ocean mixing timescales. Therefore, by correcting for a common ice volume signal over short timescales and abrupt changes there is a risk of over/under-correcting, since very few areas will experience the global average $\delta^{18}O_{sw}$ change perfectly in phase with the sea level. In surface waters near the sites of melting ice sheets, the $\delta^{18}O_{sw}$ signal will be much larger before it is redistributed by ocean and atmospheric mixing. Additionally, a sea level change of around 30 m would lead to a global average increase in $\delta^{18}O_{sw}$ of around ~ 0.33‰ (Fairbanks, 1989) and therefore cannot be used to explain the high magnitude and abrupt nature of the $\delta^{18}O_c$ observed in my record . However, it should still be kept in mind when interpreting the results, and in particular, for comparing the absolute values during the deglacial to those observed in the Holocene or today.

To conclude, the abrupt $\delta^{18}O_c$ changes observed in this record cannot solely be explained by changes in global ice volume or meltwater and in this thesis will primarily be interpreted to reflect temperature, although the other influences cannot be ruled out entirely. This will be discussed at greater lengths in subchapter 7.4.

7.2 Natural variability in AW inflow/properties during the deglaciation

The flow of relatively warm and saline AW, with temperatures of above 0°C (Pérez-Hernández et al., 2017) and salinity of approximately 35 has a large impact on hydrographic conditions in the Arctic Ocean (Ślubowska et al., 2005). The changes in AW inflow through the Fram Strait during the last deglaciation are poorly constrained due to the lack of well-dated, high resolution records (Ślubowska et al., 2005), as a result of high dissolution of calcareous material (Ivanova et al., 2019). Numerous multiproxy paleo-oceanographic reconstructions for the deglaciation and early Holocene have been done in western and northern Svalbard including north of the Vestnesa Ridge (El bani Altuna et al., 2021), the

Hinlopen Trough (Ślubowska et al., 2005; Ślubowska-Woldengen et al., 2007), the Kvitøya Trough (Kristensen et al., 2013, Pieńkowski, 2021 #134; Ivanova et al., 2019) and the Franz Victoria Trough (Lubinski et al., 2001). These cores all lie within the path of AW inflow into the Arctic (figure 7.2). The only stable isotope record covering the whole YD from the Kvitøya Trough finds a decrease in planktic and benthic δ^{18}O during the YD, explaining this to be a result of freshwater/meltwater discharge and brine formation (Ivanova et al., 2019). Kristensen et al. (2013) also performed stable isotope analysis on a core in the Kvitøya Trough but did not obtain a stable isotope record for the YD due to a lack of foraminifera. Below, the stable isotope results for the Kvitøya Trough from this thesis will first be compared to proxy studies from the surrounding areas before being put into the greater climate context. It needs to be kept in mind that all comparisons are highly dependent on the uncertainty of the age models.

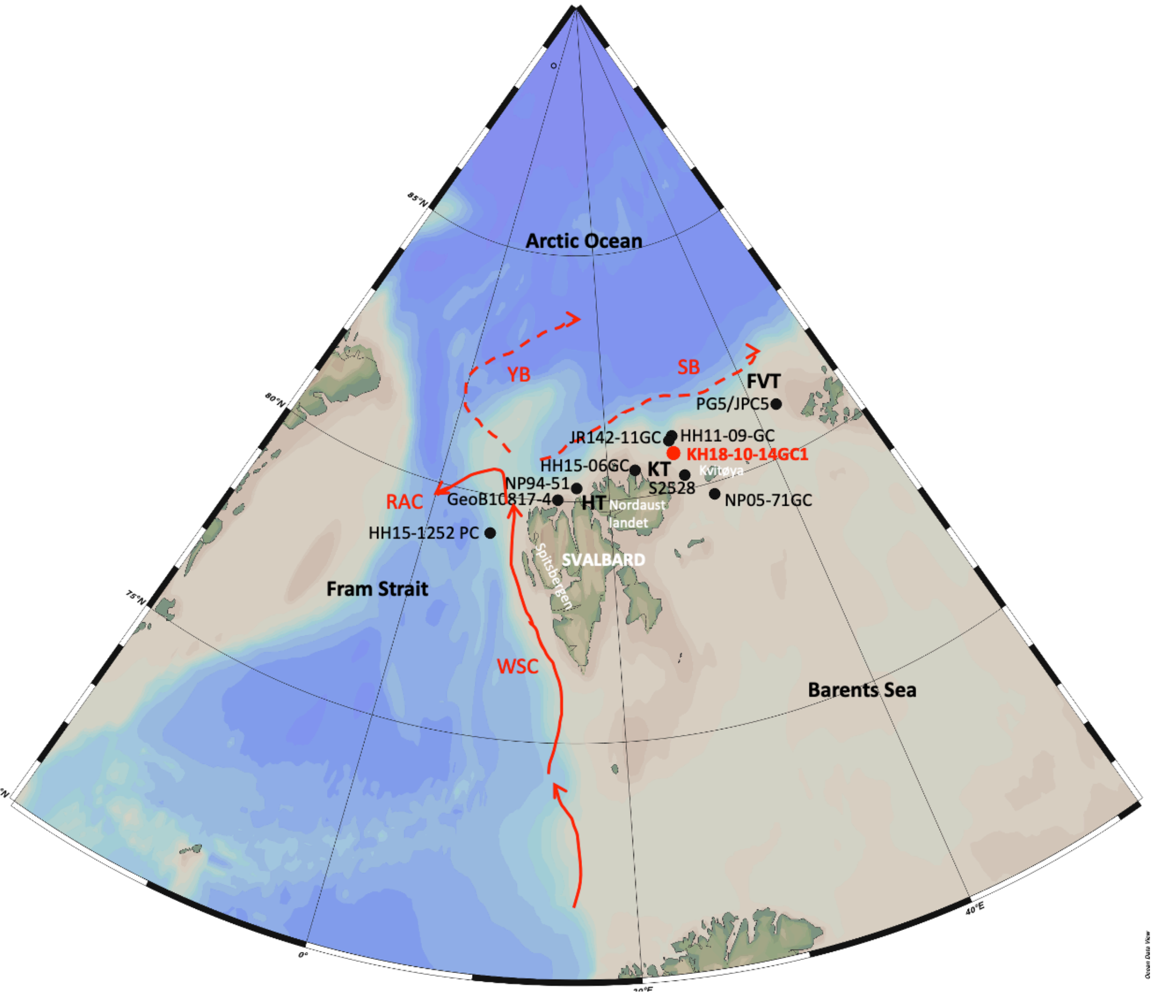

Core	Location	Depth	Reference
HH15-1252 PC	79.04° N, 6.89° E	1273 m	(El bani Altuna et al., 2021)
GeoB10817-4	79.80° N, 14.20° E	171 m	(Bartels et al., 2017)
NP94-51	80.21° N, 16.18° E	400m	(Ślubowska et al., 2005)
HH15-06GC	80.32° N, 23.31° E	320m	(Pieńkowski et al., 2021)
JR142-11GC	81.04° N, 28.55° E	369m	(Pieńkowski et al., 2021)
KH18-10-14GC1	80.69° N, 28.95° E	552 m	This thesis
HH11-09-GC	81.16° N, 29.13° E	488 m	(Chauhan et al., 2016)
S2528	80.40° N, 29.26° E	428 m	(Ivanova et al., 2019)
NP05-71GC	Not given	360 m	(Kristensen et al., 2013)
PG5/JPC5	81.07° N, 43.25° E	463 m	(Lubinski et al., 2001)

Figure 7.2 Map showing the location of the relevant cores discussed in the text (black solid dots) in relation to the core used in this thesis, KH18-10-14-GC1 (red solid dot). The red arrows show the Atlantic-sourced Western Spitsbergen current (WSC), Svalbard Branch (SB), Yermak Branch (YB) and Return Atlantic Current (RAC). The Hinlopen Trough (HT), Kvitøya Trough (KT) and the Franz Victoria Trough (FVT) are labeled on the map. The table provides the name, coordinates, depth and the reference for each core shown on the map (Map made in Ocean Data View).

7.2.1 The Bølling-Allerød (13 600 – 12 900 cal yr BP)

The oldest part of core KH18-10-14GC-1 used in this thesis covers the late B/A. This section has relatively high planktic δ^{18}O values, in comparison to the YD, with an average of 3.90‰ (figure 7.3). The benthic δ^{18}O values for this interval are even higher for *C. neoteretis* with an average of 4.74‰ and *N. labradorica* with an average of 4.73‰.

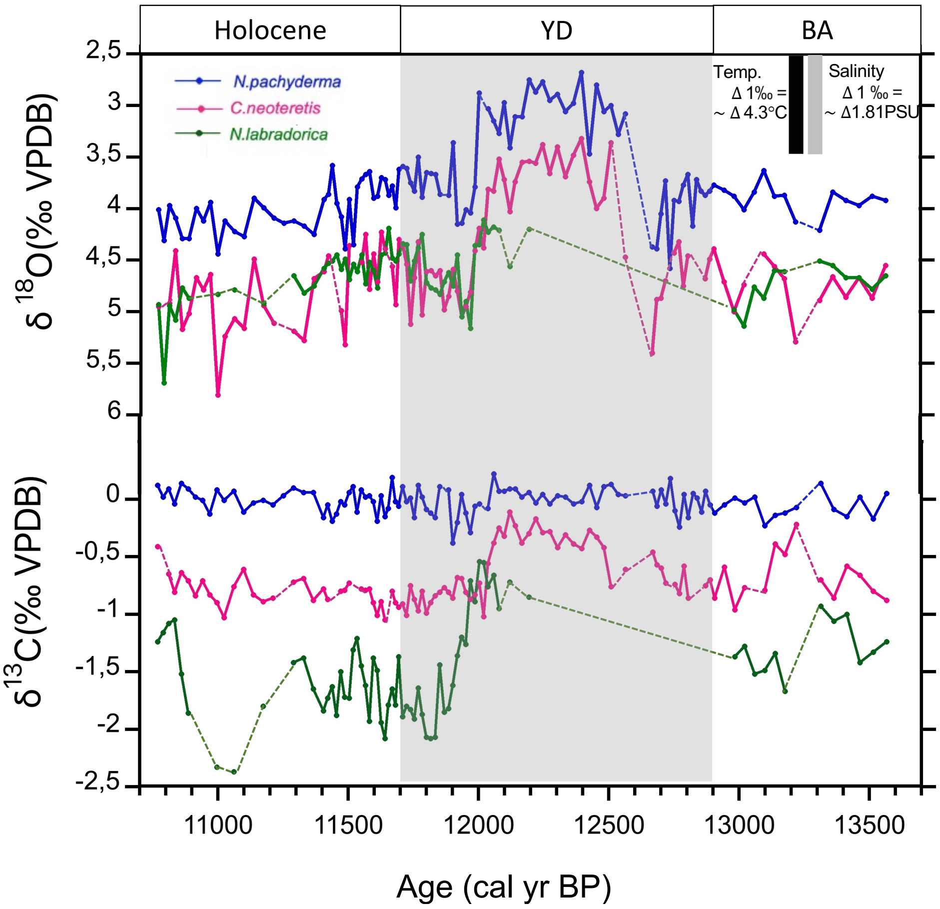

Figure 7.3 The δ^{18}O and δ^{13}C records for *N. pachyderma* (blue), *C. neoteretis* (pink) and *N. labradorica* (green) plotted versus age (cal yr BP). Periods where foraminifera are absent are indicated as dashed lines. The grey block highlights the YD. The y-axis for δ^{18}O is reversed.

It is generally thought that during the B/A there was constant influx of AW into the western and northern Svalbard shelf (Koç et al., 2002; Ślubowska et al., 2005; Kristensen et al., 2013; Ivanova et al., 2019). This inference is mainly supported by the presence of *C. neoteretis*, a species found in temperatures ranging from 0.5 - 3°C in the modern ocean (Wollenburg and Mackensen, 1998), often associated with chilled AW in the Barents Sea and Svalbard region (Ślubowska et al., 2005; Cage et al., 2021). An increased AW inflow is not immediately evident in our record upon first inspection. The average planktic and benthic δ^{18}O values for the B/A being at maximum 0.1‰ lower than the early Holocene. However, this slightly lower average of $\delta^{18}O$ during the B/A compared to the early Holocene could indicate slightly lower salinity/higher temperature bottom waters (Kristensen et al., 2013) but overall, similar to conditions in the early Holocene. The lack of change observed between the B/A and the Holocene in this record could be because only the end of the B/A is captured by our record. According to Kristensen et al. (2013) there was a declining AW inflow between 14 000 and 12 950 cal yr BP, although this is only based on three data points. However, when the $\delta^{18}O$ values are adjusted for the higher ice volumes at the time, by ~0.3‰ due to the change in sea level between 13 700 and 10 700 cal yr BP (Fairbanks, 1989), the $\delta^{18}O$ values may have been up to 0.4‰ lighter than in the early Holocene. If driven by temperature this could mean that subsurface temperatures were actually ~1.7°C warmer during the late B/A than in the early Holocene, which could support increased temperature and/or inflow of AW.

7.2.2 The Younger Dryas (12 900 – 11 700 cal yr BP)

Early Younger Dryas (12 900 – 12 000 cal yr BP)

At the onset of the Younger Dryas, according to our age model, $\delta^{18}O$ increases in both the planktics and the benthics (figure 7.3) indicating an initial decrease in ocean temperature. After this increase, both *N. pachyderma and C. neoteretis* disappear entirely from ~12 700 to 12 500 cal yr BP. This disappearance was likely due to harsh subsurface and bottom water environments (Ivanova et al., 2008) leading to dissolution of foraminifera in the sediment. Dissolution of $CaCO_3$ in the sediment can be due to increased export and respiration of organic matter leading to decreased $CO^{2-}{}_3$ and thus $CaCO_3$ dissolution (Battaglia et al., 2016). Dissolution of foraminiferal tests can also occur due to corrosive brines (Fossile et al., 2020). This dissolution is also evidenced by the relatively low Ca/Fe ratio during the early YD (figure 7.5). Another explanation for the disappearance could be a rapid pulse of sedimentation diluting the biogenic components during this period. Directly after this disappearance of foraminifera, an extreme warming (or freshening) event occurs in the subsurface and deep water, as indicated by a rapid decrease in $\delta^{18}O$. This is a significant finding because, if this is exclusively due to warming, it could have been on the order of between 5-8°C. This warming/freshening lasts for a long period of 500 years and ends abruptly at 12 000 cal yr BP. This low $\delta^{18}O$ interval clearly falls within the YD, even given the uncertainties of the age model.

This distinctly low interval in δ^{18}O in both the planktic and benthic records is also observed in core S2528, from Kvitøya trough, showing a decrease in δ^{18}O of over ~1‰ during the YD (Ivanova et al., 2019) (figure 7.4). This minimum in δ^{18}O in core S2528 shows similar characteristics to the δ^{18}O minimum in KH18-10-14GC-1 although, while it is under-resolved and its boundaries poorly defined, it may span a slightly longer time period in the YD interval. The slight offsets between the δ^{18}O minimum peaks from the different records could be due to the uncertainties of both of the age models as well as the lower resolution of the study done by Ivanova et al. (2019) (who sampled at a resolution 3-4 cm; equivalent to 18 – 340 years between samples in comparison to this study where each sample is equivalent to 16 - 40 years). Ivanova et al. (2019) interprets the peak in *N. pachyderma* and *C. neoteretis* δ^{18}O as a result of freshwater/meltwater discharge from the Laurentide icesheet or Lake Agassiz, explaining the depleted benthic δ^{18}O as a result of the light isotopes being transferred to the deeper water through brine release from ice formation. There is only one *N. labradorica* δ^{18}O record from the Kvitøya Trough from a recent paper by Pieńkowski et al. (2021). However, if the same reservoir ages and calibration is applied to that data, as used here, that record does not span the YD and it is therefore not possible to make an in-depth comparison for the YD (figure 7.3 light green curve) in this interval.

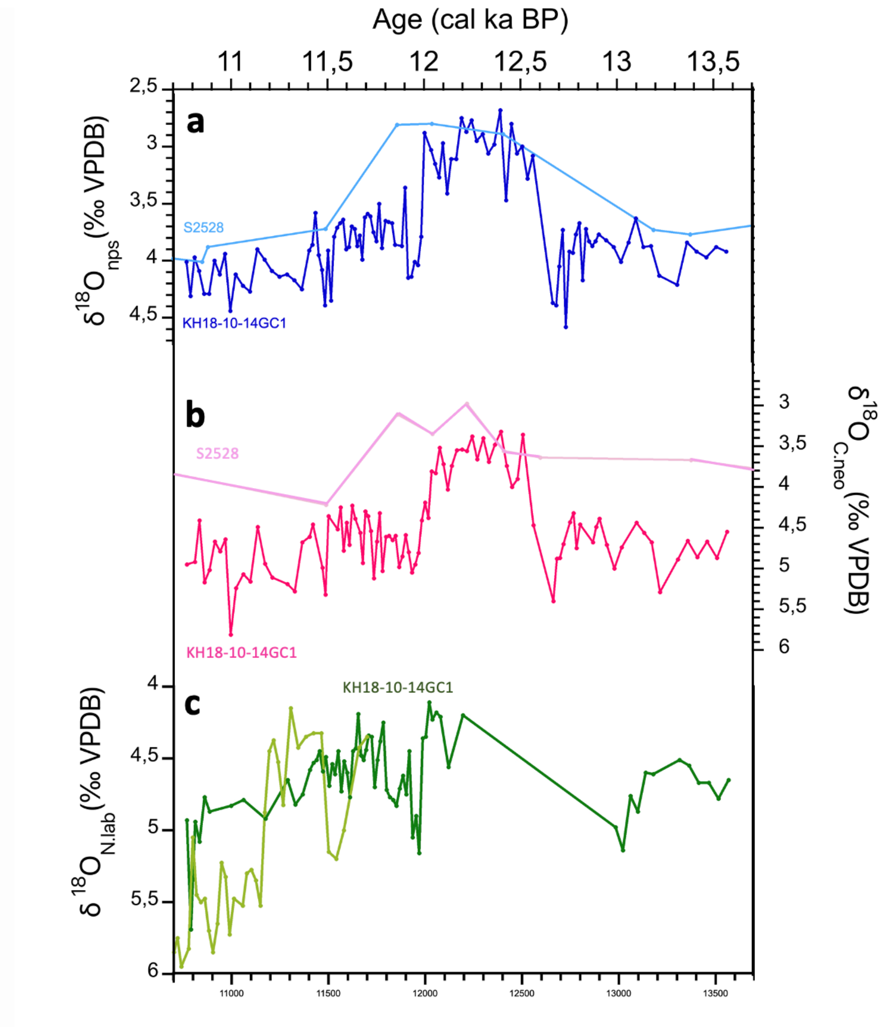

Figure 7.4 Stable isotope $\delta^{18}O$ records of a) *N. pachyderma* and b) *C. neoteretis* from KH18-10-14GC-1 compared to those obtained from a nearby core S2528 (Ivanova et al., 2019). The age model for core S2528 has not been redone as only the calibrated dates were available. c) $\delta^{18}O$ *N. labradorica* is plotted versus $\delta^{18}O$ data obtained from HH15-06GC (Pieńkowski et al., 2021). The age model of HH15-06GC has been recalibrated using the same calibration as used in this thesis.

These low $\delta^{18}O$ values during the YD can also be correlated with similar low $\delta^{18}O$ values seen in core geoB10817-4 from Woodfjorden (Bartels et al., 2017), PG5/JPC5 from the Franz Victoria Trough (Lubinski et al., 2001) and HH11-09GC from north of Nordauslandet (Chauhan et al., 2016) (locations shown in figure 7.3). The low $\delta^{18}O$ values are interpreted by Lubinski et al. (2001) and Chauhan et al. (2016) to represent low salinity due to freshwater/meltwater events. Numerous studies from northern and western Svalbard using foraminiferal assemblages as a proxy and/or stable oxygen isotopes also support this freshening/weaker AW influence. Kristensen et al. (2012) found polar water to be most prevalent at a depth of 360 m during the YD with decreased AW influence during the YD, supported by sparse fauna and sedimentological data. Slubowska et al. (2005) also found a reduction in AW in comparison to the BA based on foraminiferal assemblages. However, since these papers do not make use of the same proxy (stable isotopes) to deduct information of AW properties during the YD it is difficult to compare these results to ours. These studies claim that AW was weaker relative to the B/A but not necessarily absent. In fact, this δ^{18}O peak during the YD which has often been interpreted as a freshwater event has also been found to correspond to an increase in subsurface AW inflow—or at least greater geographic influence (Ślubowska et al., 2005; Ivanova et al., 2019).

Subsurface warming during the early YD?

The constant presence of *C. neoteretis* throughout the record in this thesis (except for a short interval of under 100 years where they are absent) is indicative of subsurface AW inflow into the Kvitøya Trough (Ivanova et al., 2019) below the low salinity surface layer (Ślubowska et al., 2005). Ivanova et al. (2019) found increased subsurface AW advection and associated buildup of subsurface heat during the YD and Ślubowska et al. (2005) also found an inflow of subsurface AW inflow during the YD based on the presence of *C. neoteretis*. AW was also found to still be advected as a subsurface water mass between 12 700 – 12 400 cal yr BP in Woodfjorden, leading to warming surface waters and increased iceberg melting (Bartels et al., 2017). These studies therefore provide evidence that the low δ^{18}O signal in both the planktic and benthic records could have instead been a result of warming, due to warm intermediate AW inflow during the YD. This potential warming during the YD stadial will be discussed further in subchapter 7.3.

Late Younger Dryas (12000 – 11 700 cal yr BP)

At approximately 12 000 cal yr BP there is a significant change in water properties seen in both the δ^{18}O and δ^{13}C records. At 12 000 cal yr BP a rapid increase in planktic and benthic δ^{18}O indicates a return to colder subsurface water conditions. This rapid increase in δ^{18}O was also found at end of the YD in core S2528 but is not discussed in that paper (figure 7.4) (Ivanova et al., 2019). The increase in δ^{18}O is seen in the late stages of the YD in core HH11-09GC from north of Nordauslandet (Chauhan et al., 2016) and core GeoB10817-4 from Woodfjorden (Bartels et al., 2017). Bartels et al. (2017) observes significant changes after 12 000 cal yr BP in their core too, including lower IRD and changing foraminiferal assemblages (decrease in *Elphidium clavatum*). They found that surface waters cooled during the late YD (12.4 – 11.7 ka), sea ice increased, and AW penetrated into the deeper waters (Bartels et al., 2017). This shift in water mass properties could be due to a change in stability towards the end of the YD.

Changes in productivity during the YD

The benthic $\delta^{13}C$ records for *N. labradorica* and *C. neoteretis* exhibit an increasing trend in $\delta^{13}C$ during the YD with values increasing by ~1‰ (figure 7.3). The peak in $\delta^{13}C$ is reached during the low $\delta^{18}O$ anomaly. If these high $\delta^{13}C$ values were seen in the planktic foraminiferal record it could indicate high productivity or well ventilated waters (Kristensen et al., 2013; El bani Altuna et al., 2021) but the $\delta^{13}C$ values of *C. neoteretis* and *N. labradorica* are however likely to be affected by pore water composition. The $\delta^{13}C$ offset, between the shallower infaunal and deeper infaunal species is, as discussed in section 4.3.2, a useful proxy for productivity. Large $\Delta\delta^{13}C$ ($\delta^{13}C_{neoteretis}$ - $\delta^{13}C_{labradorica}$) gradients therefore indicate higher productivity in the water column leading to higher flux of organic matter to the sediment, and respiration therein. Towards the end of the YD (12 000 cal yr BP) there is an increase in $\Delta\delta^{13}C$ occurring simultaneously with higher $\delta^{18}O_c$ values (figure 7.3). The lower offset of around 0.5‰ during the ealy YD could indicate lower productivity during this interval. This agrees with the findings of Ivanova et al. (2016) who inferred low productivity during the YD in the Kvitøya Trough based on low foraminiferal abundances, dinocyst concentrations and total organic content. This high offset of around 1‰ could indicate a change in productivity between the early and late YD, with enhanced export production towards the end of the YD, possibly when sea ice coverage began to decline. The reappearance of *N. labradorica* at 12 200 cal yr BP is alone a factor which supports an increase in productivity, as *N. labradorica* generally prefers frontal zones with high productivity (Ivanova et al., 2019; El bani Altuna et al., 2021).

Elemental changes during the YD

There is a rapid increase in manganese (cps) occurring concurrently with the rapid decrease in $\delta^{18}O$ at the beginning of the YD (figure 7.5). Manganese (Mn) is a highly redox sensitive element (Rothwell and Croudace, 2015) and precipitates in oxic conditions. Peaks in Mn are often seen during interglacial periods due to changes in ventilation and/or riverine input (Löwemark et al., 2016). This rapid increase in Mn during the YD could indicate oxidized bottom waters allowing for the formation of MnO_2. Mn peaks can be found during sub-oxic diagenesis where Mn is mobilized and migrates upwards through the water and precipitates where there are oxic conditions (Rothwell and Croudace, 2015). Mn peaks in the sediment can also be attributed to a migration of the manganese redox boundary, which can be due to changes in bottom water oxygen, fluxes of organic matter and changes in the rates of oxidation of organic matter (Burdige, 1993). When the redox boundary deepens it leaves behind a manganese oxide peak where it used to be (Burdige, 1993). This peak could therefore be a result of a decrease in productivity (and organic matter flux) at the beginning of the YD and thus a decrease in pore water oxygen consumption (respiration), deepening the manganese redox boundary. This peak corresponds to a change in environmental conditions seen in KH18-10-14GC-1 from laminated sediments (colorful laminations) to more homogenous sedimentation (colour scans in figure 6.1), which could possibly indicate increased bioturbation further supporting a shift to more oxygenated conditions. Since Mn peaks are found at the manganese-redox boundary and can also shift in the sediment with time (Burdige, 1993), the peak in KH18-10-14GC-1 likely represents bottom water and pore water conditions slightly offset (later) in time from the sediments in which it is found. However, since Mn redox fronts are often quite shallow in Arctic sediments (only a few centimeters (Katsev et al., 2006)) this time offset is likely quite short given the relatively high sedimentation rates (50 - 63 cm/kyr) at this location during the interval of this study.

The Ca/Fe is a ratio indicating the biogenic to terrestrially sourced sediments (Rothwell and Croudace, 2015). Calcium (Ca) can be interpreted as a biogenic indicator in this core as it covaries with strontium (Sr) (Appendix C), which is an element often fixed by calcifying organisms simultaneously with Ca (Rothwell and Croudace, 2015). The low Ca/Fe at the beginning of the YD could indicate high Ca dissolution during this period, potentially also explaining the absence of foraminifera during this period, or rapid terrigenous input with low Ca content. The peak in Ca/Fe occurring at the same time as the low δ^{18}O interval could be indicative of more biogenic material than detrital material during this period of the YD.

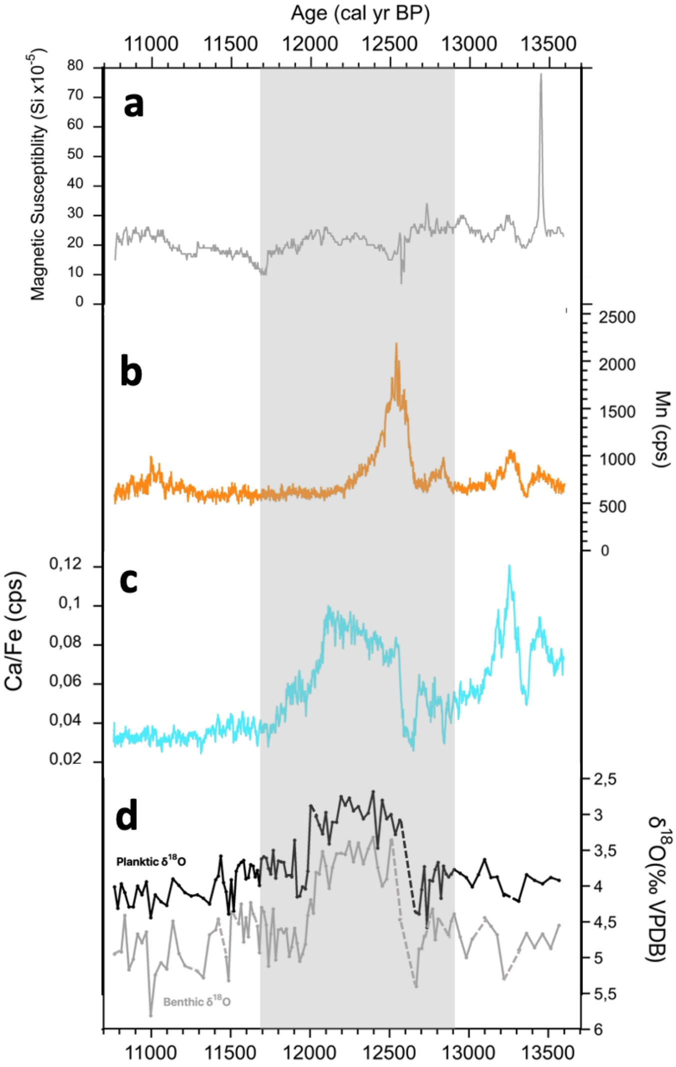

Figure 7.5 Physical parameters and elemental compositions of KH18-10-14GC-1 including a) the magnetic susceptibility b) the manganese content in counts per second c) the ratio of calcium to iron shown in relation to d) the δ^{18}O of *N. pachyderma* (planktic) and *C. neoteretis* (benthic).

7.2.3 The early Holocene (11 700 – 10 700 cal yr BP)

The early Holocene has the highest δ^{18}O averages for all three species compared to the rest of the record showing a gradually increasing trend throughout the first 1000 years of the Holocene (figure 7.3). This relatively high average and increasing trend indicate a decrease in water temperatures/increased salinity during this period. These findings concur with the increased cool and saline AW inflow found by Kristensen et al. (2013), supported by an increase in benthic δ^{18}O between 11 700 to 11 000 cal yr BP. A cooling at the onset of the Holocene has been found by many studies in the area (Lubinski et al., 2001; Ivanova et al., 2008; Kristensen et al., 2013). Ivanova et al. (2019) found severe polar conditions to exist up until 10 500 cal yr BP with cold, higher salinity AW flowing in below the Arctic Water. The rapid decrease in *C. neoteretis* content seen in core JPC-5 of Lubinski et al. (2001) indicates a rapid fall in subsurface and bottom water temperatures during the early Holocene. This abrupt decrease in temperature at the start of the Holocene was also seen in the BWT and δ^{18}O (increase) in Ezat et al. (2014). The presence of *C. neoteretis* seen in two cores obtained to the north of the KT (HH15-06GC and JR142-11GC) indicate that AW was still reaching around 81°N during the early Holocene (Pieńkowski et al., 2021). The offset in δ^{13}C between *C. neoteretis* and *N. labradorica* remains high during the early Holocene, possibly showing maintained high productivity. δ^{13}C drops to very low values around 11 061 cal yr BP reaching a minimum of -2.37‰. According to Piénkowski et al. (2021) the low endobenthic δ^{13}C of *N. labradorica* could represent increased productivity. In summary, the onset on the Holocene saw a shift to colder subsurface and bottom water temperatures and higher productivity from warmer water temperatures and low productivity during the YD.

7.3 Subsurface warming during cold stadials like the YD

A major finding of this thesis as discussed above is the distinctly low δ^{18}O interval which starts in the early YD and ends at 12 000 ± 280 cal yr BP. Studies from the northern Barents Sea have shown a depletion in benthic δ^{18}O values during the YD (Lubinski et al., 2001; Bartels et al., 2017; Ivanova et al., 2019) but the source of this anomaly, and the relative roles of temperature and salinity changes, remain ambiguous. Indeed, a number of studies (Lubinski et al., 2001; Chauhan et al., 2016) have argued as recently as in 2019 (Ivanova et al., 2019) for a major role of freshwater/meltwater to explain these anomalies. However, a growing number of studies document decreases in benthic δ^{18}O of between ~ 0.5‰ – 2‰ during cold "stadial" periods (Rasmussen and Thomsen, 2004; Ezat et al., 2014)—similar in magnitude to those found here for the YD.

Due to the ambiguity of the δ^{18}O proxy the possibility of brine rejection transporting low δ^{18}O waters to great depths needs to be considered. Low benthic δ^{18}O values during cold stadials have sometimes been explained by the rejection of dense, low δ^{18}O brines produced during sea ice formation transporting isotopically low δ^{18}O waters to greater depths (Dokken and Jansen, 1999). In the Barents Sea, low δ^{18}O brines are not dense enough to penetrate AW and the only brines responsible for deep water formation have high salinities and δ^{18}O values (Rasmussen and Thomsen, 2009; Mackensen and Schmiedl, 2016). According to Rasmussen et al. (2009) the low δ^{18}O values cannot be explained by brine formation. Additionally, the

$\delta^{18}O$ values of *N. pachyderma* in this thesis (between 2,6 and 4,6‰) are significantly higher than those interpreted to be fresh halocline water such as those found in the western Arctic Ocean with values between 1.5 and 0.5‰ (Hall and Chan, 2004). The relatively stable planktic $\delta^{13}C$ record (with a range of only 0.6‰) (figure 7.3) suggests that the *N. pachyderma* tended to calcify in a water mass with similar chemical characteristics throughout the study period—tentatively consistent with a steady influence of AW in the region and arguing against intermittent periods with dominance of riverine or other (carbon isotopically) depleted halocline influences. Thus, no modern analogues provide evidence for the low planktic and benthic $\delta^{18}O$ values observed during the YD being due to brine formation, and KH18-10-14GC1 was most likely constantly affected by AW during this period.

Proxy records for the North Atlantic have shown that during stadials there was reduced deep water formation (Henry et al., 2016) and AW occupied intermediate depths beneath a strong halocline (Rasmussen and Thomsen, 2004; Ezat et al., 2014; El bani Altuna et al., 2021). A recent study by El bani Altuna et al. (2021) demonstrate how widespread subsurface warming is typical during stadial events throughout the North Atlantic and Nordic Seas, with subsurface water temperatures increasing by up to 5°C (figure 7.6). This warming is evidenced by high bottom water temperatures (BWT) indicated by benthic Mg/Ca as well as low benthic $\delta^{18}O$ values (similar to the values observed in my record during the YD). El bani Altuna et al. (2021) found that there was a deepening of AW during stadials when there was less deep water formation. The warming of the subsurface layers was due to a strong halocline preventing convection and heat loss to the atmosphere from the subsurface AW (El bani Altuna et al., 2021). This increase in BWT has also been seen in cores further south in the Nordic seas, to the north of the Faroe Islands (Ezat et al., 2014; Sessford et al., 2019). Core JM11-FI-19PC (Ezat et al., 2014), for example, shows a similar trend to KH18-10-14GC-1 with a decrease in benthic $\delta^{18}O$ during the YD (figure 7.7). This low $\delta^{18}O$ corresponds with an increase in BWT (calculated from Mg/Ca) and reduced overturning circulation (higher $^{231}Pa/^{230}Th$), similar to what is observed during the Heinrich stadials.

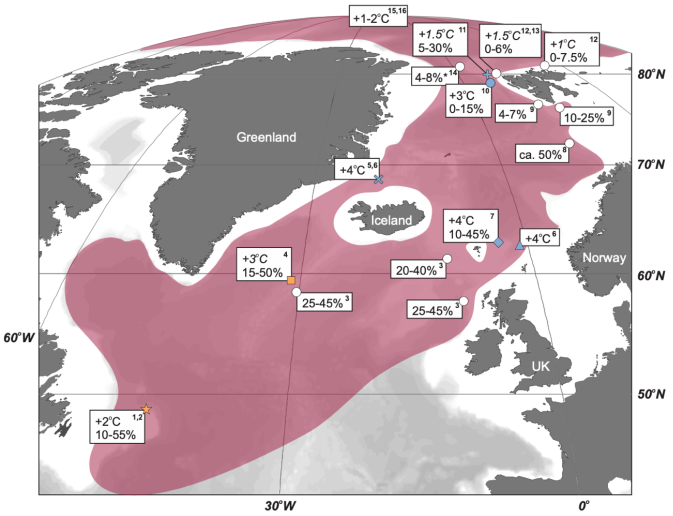

Figure 7.6 A compilation of sediment core records showing the percentage of "Atlantic species" and difference in absolute BWT between Heinrich stadials and Greenland Stadials compared to the previous interstadial period. The red shaded areas indicate the presence of northward Atlantic subsurface intermediate water flow. The BWT written in italics were obtained from benthic foraminiferal transfer functions (El bani Altuna et al., 2021) .

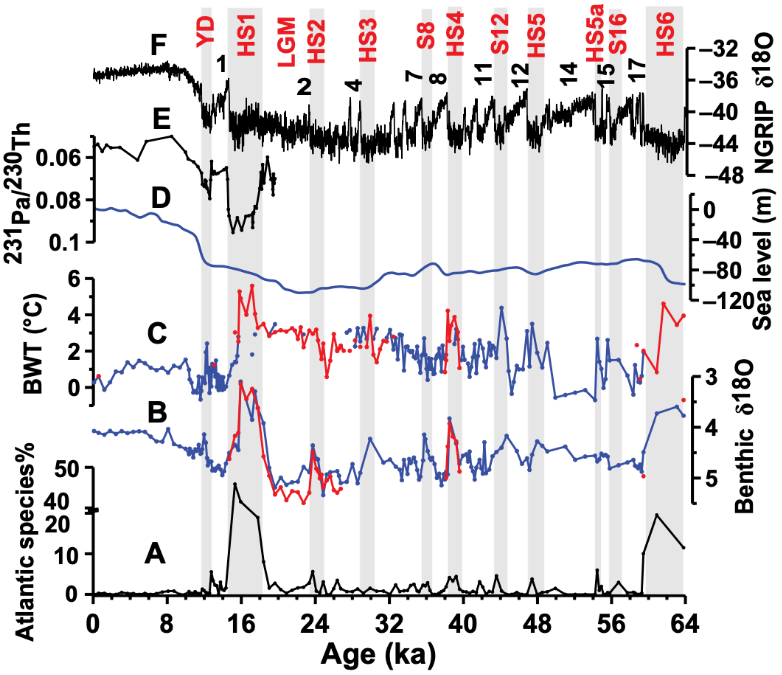

Figure 7.7 Various proxies from core JM11-F1-19PC versus the North Greenland Ice Core Project (NGRIP) Greenland Ice Core Chronology 2005. (A) Percentage of Atlantic species (B) Benthic δ^{18}O values of *Melonis barleeanus* (blue) and *Cassidulina neoteretis* (red) (C) Mg/Ca-based bottom-water temperature (BWT) measured on *M. barleeanus* (blue) and *C. neoteretis* (red). (D) Sea-level record. (E) ^{231}Pa/^{230}Th record from Bermuda Rise (F) NGRIP ice core δ^{18}O values. The numbers are interstadials and gray bars include Heinrich stadials (HS), stadials (S), the Last Glacial Maximum (LGM), and Younger Dryas (YD) (Ezat et al., 2014 and references therein).

This intermediate warming during stadials is further supported by modelling papers which have shown that a strong enough surface freshening can lead to warming of intermediate waters (Mignot et al., 2007; Brady and Otto-Bliesner, 2010; He et al., 2020). He et al. (2020) showed that when there is a weak surface freshening, weakened AMOC leads to less heat transport and therefore cooling, while in the case of a strong surface freshening, warming due to suppressed vertical mixing overwhelms the cooling effect of reduced heat transport, leading to net warming of subsurface waters. The freshwater induced warming agrees with the results of Mignot et al. (2007), who use a coupled climate model to show that a freshwater forcing in the high latitudes (at deep water formation sites) can lead to extreme warming of intermediate water of up to 8 Kelvin (figure 7.8). Interestingly, the degree, or even the sign of subsurface warming in response to fresh water forcing, stratification and sea ice expansion, can vary depending on the model and the forcing applied. For example, He et al. (2020) argued that strong subsurface warming may be a consequence of strong fresh water forcing such as that associated with Heinrich events while weaker forcing, such as what might have occurred during the YD, does not result in high subsurface warming. This is, however, highly dependent on the freshwater flux estimated for the YD and the threshold of fresh water set for subsurface warming in the model. It is thus highly plausible that the surface freshening and increased sea ice during the YD could have driven a decrease in ocean to atmosphere heat flux causing intermediate warming.

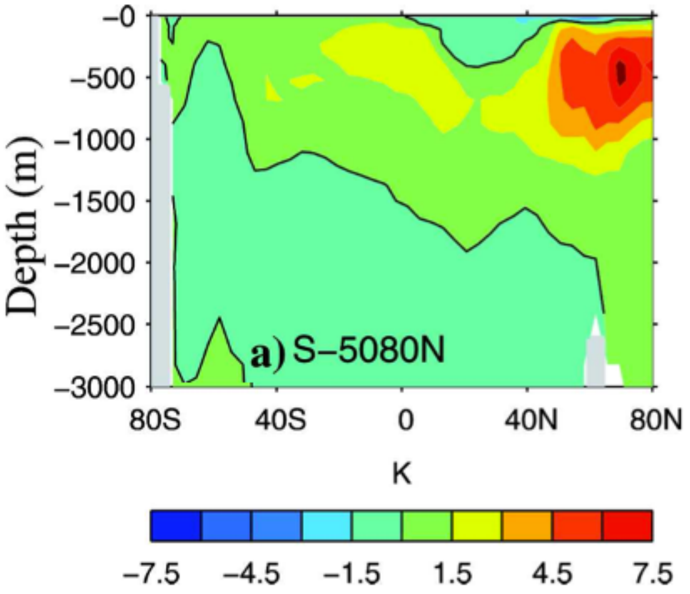

Figure 7.8 The zonally averaged temperature anomaly compared to the control run in the Atlantic Ocean due following a 100-year fresh water forcing (corresponding to 0.35 Sv) between 50 to 80 °N. This shows a distinct warming in the North Atlantic. Modified from Mignot et al. (2007).

In summary, the YD minimum in $\delta^{18}O$ (in KH18-10-14GC-1) is consistent in sign and magnitude to the warming of subsurface water as has been shown to occur during stadials by numerous proxy and modeling studies. The major difference between the proxy studies interpreting the low benthic $\delta^{18}O$ as a meltwater spike, versus the studies supporting a temperature increase during cold stadials, is the use of the additional proxy, Mg/Ca. The studies which make use of Mg/Ca, as well as the modeling studies concur that a warming of magnitude 2.5°C to > 8°C can occur due to a strong halocline and decline of AMOC during stadials (Mignot et al., 2007; Ezat et al., 2014; Sessford et al., 2019; El bani Altuna et al., 2021). Although some freshwater influences cannot be excluded, the negative $\delta^{18}O$ anomaly of 1.28‰ (near surface) and 2.04‰ (bottom water) (figure 7.3) is consistent with a similar warming of 5 - 8°C occurring during the YD.

7.4 AW warming in the greater context

It is complicated to establish the history of ocean-cryosphere-sea-ice-atmospheric interactions and feedbacks. The uncertainty of the age model for KH18-10-14GC-1 (± 280 years) (and the other age models of the proxies used for comparisons) prevents reliable interpretation of any detailed lead-lag relationships between proxies generated from different sites. Thus, although the exact timing and duration of YD changes cannot be determined, our age model does confirm that a rapid and high magnitude decrease in oxygen isotopes occurs. A likely explanation is a large subsurface to intermediate ocean warming during the YD. A thickening and deepening of AW has been proposed to occur during some Greenland Stadials and Heinrich stadials during periods of reduced deep water production (El bani Altuna et al., 2021). A thick halocline due to increased meltwater and increased sea ice coverage during the YD could have contributed to reducing the loss of heat from the subsurface layers (El bani Altuna et al., 2021). It has long been known that a large portion of the buoyancy loss, cooling and densification necessary to form deep water, occurs along the horizontal circulation path as warm AW advects northward (Mauritzen, 1996). In a recent paper Zhang and Thomas (2021) re-emphasize the importance of the horizontal circulation and point out that the northernmost regions where AW is in contact with the atmosphere are particularly important for deep-water formation (buoyancy loss). In this sense, the Arctic Ocean is in fact the northern terminus for deep water formation (Zhang and Thomas, 2021). As a result, one of the largest contributors to AMOC is the AW that has continued to travel into the Arctic Ocean increasing in density due to heat loss along the way (Zhang and Thomas, 2021).

During periods when the Nordic Sea was fully covered in ice, AW was found deeper in the water column, isolated from the atmosphere, thus retaining its heat (Rasmussen and Thomsen, 2004; Jensen et al., 2018). It is likely that during the YD the Nordic Seas were completely covered by sea ice in winter, the season when most buoyancy (heat) loss occurs, due to high amounts of ice export and freshwater export from the Arctic Ocean (Hoff et al., 2016). Bradley and England (2008) have suggested that sea ice had a greater extent during the YD reaching as far as ~ 60°N. The increased sea ice extent during the YD (Bradley and England, 2008) is supported by high IP_{25} and $IPSO_{25}$ (sea ice biomarkers) from core JR142-11GC, located in close proximity to our site, between 12 200 and 12 000 cal yr BP (figure 7.9 d). Increased reservoir ages during this period (figure 7.9 b) also support increased sea ice coverage and decreased AMOC because these processes both result in less exchange of $^{14}CO_2$ between the ocean and atmosphere (Austin et al., 2011). The increase in sea ice extent likely resulted in a southward shift in the sea ice edge during the YD, effectively reducing the path length for AW to lose heat and buoyancy and therefore having a strong impact on deep water formation. Intermediate water warming is supported by models showing that when intermediate depth ventilation is suppressed due to sea ice or fresh water, the subsurface waters are isolated from the cold atmosphere and therefore warm (Knutti et al., 2004; Mignot et al., 2007; Sessford et al., 2019). Models also show that a fresh water forcing can lead to a partial or complete shutdown of AMOC due to decreased deep water formation (Knutti et al., 2004; Mignot et al., 2007).

Changes in the geometry of AW distribution in the Nordic Seas and Arctic Ocean can have a significant effect on AMOC and vice versa. The strength of AMOC has been highly variable between stadials and interstadials (e.g., Henry et al., 2016; Ng et al., 2018). Proxy based reconstructions suggest that AMOC was strong during interstadials, with strong NADW formation and that it was reduced (nearly shut down) during stadials (Heinrich events), with NADW shoaling (Rasmussen and Thomsen, 2004). This is the same as what is seen to occur during the YD, with radiocarbon data (a proxy for water mass age and ventilation (Stern and Lisiecki, 2013)) showing an inverse trend to $\delta^{18}O$, with a peak in reservoir age concurrent to the minimum in $\delta^{18}O$ (figure 7.9 b; radiocarbon after Skinner at al. 2019). If this $\delta^{18}O$ peak is interpreted as a warming of the subsurface waters, it therefore means that the increased subsurface temperatures corresponded to weaker AMOC. The composite ^{231}Pa/^{230}Th record from Ng et al. (2018) from the North Atlantic display's higher values during the YD also indicating reduced transport/export of deep water in/from the Atlantic (Ng et al., 2018). A recent Master thesis using sortable silt (SS) as a proxy from a core very close to our core site (81.57° N, 31,61° E) found a gradual decline in grain size, and thus decreasing bottom water flow speed, during the YD followed by a resumption towards the end of the YD (~12 000 cal yr BP) (Lefèvere, 2021) thus providing further support for a reduction in AMOC (upper branch flow) during the YD stadial. Taken together, these findings suggest that AMOC was weakened during the YD at the same time that AW was thickening, warming (low δ^{18}O), and experienced weaker northward flow (from sortable silt). It is possible that the warmer AW and weaker transport of AW were caused by a southward expansion of sea ice during the YD which reduced the latitudinal extent of AW exposure to the atmosphere.

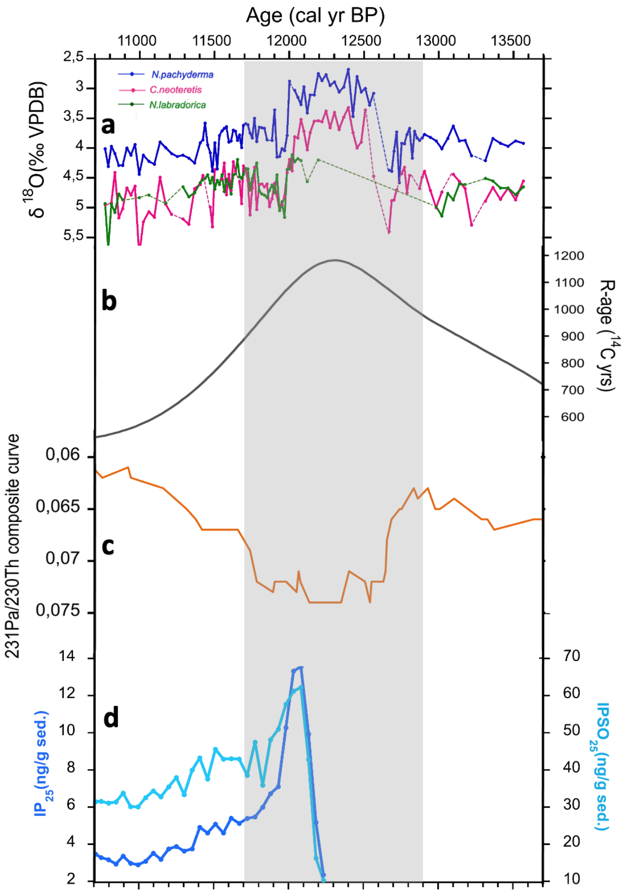

Figure 7.9 a) The δ^{18}O of *N. pachyderma, C. neoteretis and N. labradorica* in relation to the b) best fit cubic spline for high latitude NA reservoir ages (in ^{14}C years) (Skinner et al., 2019) c) ^{231}Pa/^{230}Th composite curve from the North Atlantic Cores (Ng et al., 2018) and d) the concentrations of biomarkers IP$_{25}$ (dark blue) and IPSO$_{25}$ (lighter blue) from core JR142-11GC (Pieńkowski et al., 2021). The ages for core JR142-11GC have been recalibrated using the Local20 curve used to produce the age model for KH18-10-14GC-1.

Mignot et al. (2007) have shown that if convection and ventilation are suppressed in the high latitudes, this is followed by a rapid resumption of AMOC and an increase in air temperature after the freshwater forcing is removed. This is similar to what is observed in my record, where an abrupt decrease in intermediate ocean temperatures (rapid increase in δ^{18}O) towards the end of the YD is concurrent with a rapid resumption of AMOC, decreasing sea ice coverage and increasing productivity. The shift from relatively stable to unstable (or more variable) conditions during the later YD, when the cold reversal started to lose strength, has been found to occur possibly as early as 12 300 to 12 200 cal yr BP (Bakke et al., 2009; Pearce et al., 2013; Bartels et al., 2017). The decrease of sea ice, indicated by the lower abundance of biomarkers towards the late YD (figure 7.9 d), corresponds to decreased ocean temperatures and could indicate that the loss of sea ice caused intermediate waters to come to the surface and lose their heat to the atmosphere, similar to what is shown in figure 7.10 b (Sessford et al., 2019). The increase in open water/seasonal ice free areas in the Nordic Seas would also have promoted air-sea exchange helping to explain the gradual decline seen in reservoir ages (figure 7.9 b). The decrease in ocean temperatures could have led to increased density of northern sourced deep waters and also explain the greater penetration of well-ventilated and low nutrient NADW through the Atlantic (Boyle and Keigwin, 1987; Skinner et al., 2021) before and after the YD. The reappearance of *N. labradorica* around 12 200 cal yr BP in core KH18-10-14GC-1 could indicate that the Polar Front moved closer to our core site at this time, since *N. labradorica* correlates positively with the PF (Ślubowska et al., 2005). This pronounced increase in *N. labradorica* was seen earlier during the YD in core NP94-51 from the Hinlopen Trough to the south of our core site (Ślubowska et al., 2005). This could indicate that there was a northward shift of the PF as conditions evolved within the YD and polar conditions retreated northward. A northward shift in the frontal zone during the late YD has also been suggested by Ślubowska et al. (2005) and Pearce et al. (2013), related to an increase in AMOC and highly variable sea ice conditions, as is also supported by the IP_{25} record.

In summary, an increase in intermediate ocean temperatures during the YD was likely due to an increase in sea ice extent leading to reduced convection and heat loss (Rasmussen and Thomsen, 2004; Ezat et al., 2014; Sessford et al., 2019). This scenario is similar to Mode A proposed by Sessford et al. (2019) which describes stadial conditions to have full winter sea ice coverage, associated with low benthic δ^{18}O values and warm subsurface temperatures (figure 7.10 a). Thus, as winter sea ice extends southward, and with it the point at which AW is subducted beneath the fresh halocline, the ability of AW to lose heat (buoyancy) would also decline. This can currently be observed north of Svalbard (81°N) where periods of extensive sea ice cover cause increased stratification and suppressed vertical heat flux (Renner et al., 2018). Regardless of deep convection which is the focus of most previous studies (Lumpkin and Speer, 2003; Rahmstorf, 2006), Mauritzen (1996) and Zhang and Thomas (2021) both argue that the extensive heat loss occurring during the (winter) advective transit of AW to the high northern latitudes is the critical process for dense water formation in the North Atlantic. Restricting the latitudinal extent of AW's contact with the atmosphere, e.g. by advancing winter sea ice, could have resulted in the concurrent decrease in the density and formation rate of deep water, and thus AMOC, as seen in the high reservoir ages and ^{231}Pa/^{230}Th during this period. Extending winter sea ice further south during stadial events would result in the subduction of AW before it could lose much subtropical heat—resulting in the strong subsurface warming observed in models (Mignot et al., 2007; Brady and Otto-Bliesner, 2010; He et al., 2020). These models achieve subsurface warming if fresh water forcing (and related sea ice advance) is strong enough to isolate AW from the atmosphere at lower latitudes (He et al., 2020). The fact that strong subsurface warming occurs during the YD, with its comparatively limited freshwater forcing, suggests this state may be more easily achieved than many (but not all) models currently predict.

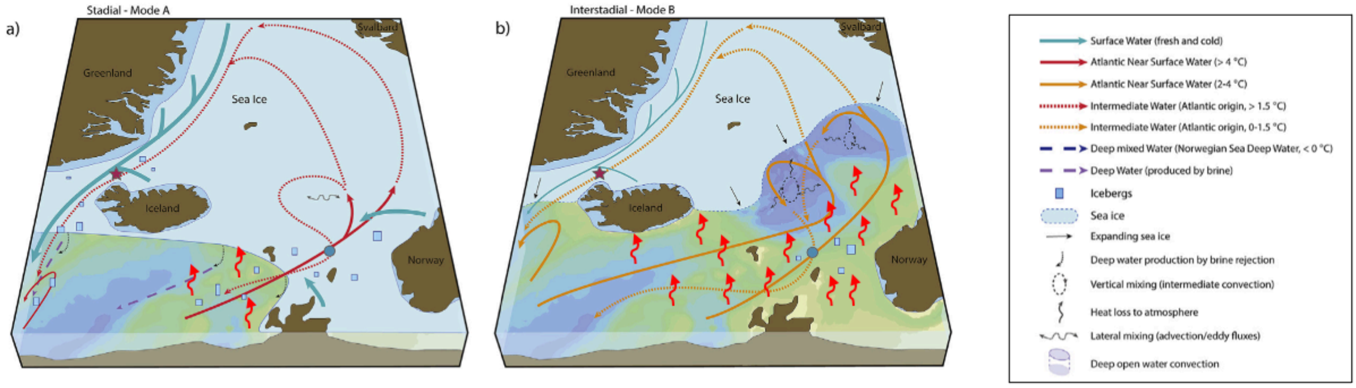

Figure 7.10 Schematic of water masses in the Nordic seas showing a) Mode A (stadial) with increased winter sea ice cover, little convection in the Nordic Seas and high intermediate water temperatures and b) Mode B (interstadial) where sea ice extent decreases, convection and heat loss increases and there is cooler AW inflow. Heat loss to the atmosphere is indicated by red arrow. Modified from Sessford et al. (2019).

It is worth reflecting on how this link between sea ice, ocean heat transport and circulation compares to recent changes. The pattern observed during the YD seems to follow that for abrupt climate changes more generally through the glacial period, with sea ice extensions associated with warmer AW. Although this pattern is mechanistically consistent with oceanographic studies documenting the importance of heat loss for AMOC (Furevik et al., 2007; Zhang and Thomas, 2021), it stands in stark contrast to the pattern found during recent decades. The recent decline of sea ice has largely been attributed to increased import of heat due to AW warming (Årthun et al., 2019). This pattern is opposite to that observed during past natural variability when sea ice advances were associated with AW warming. Although such comparisons are fraught with complications, this at least suggests that the types of changes occurring today are quite distinct from typical natural variations of the past and represent a different set of processes and drivers. Alternatively, it could be that the sign of cryosphere-ocean (circulation/heat transport) coupling varies with background climate, with ice forcing the ocean during glacial periods and vice versa during interglacials. Regardless, these results provide valuable new results for constraining models and the sensitivity of climate to coupled ice-ocean transitions.

8. Conclusion

The stable isotope δ^{18}O and δ^{13}C records obtained in this thesis provide high resolution records for an area with few continuous stable isotope records, therefore providing new information about the properties of AW inflow during a period of the last deglaciation—and specifically through the YD.

- The low benthic and planktic δ^{18}O interval during the YD between ~ 12 500 and 12 000 cal yr BP, also observed in other records in the area (Lubinski et al., 2001; Bartels et al., 2017; Ivanova et al., 2019), is interpreted in this thesis as a warming of intermediate waters in the Kvitøya Trough. The magnitude of the inferred warming (5-8°C) agrees with models (Mignot et al., 2007; He et al., 2020) and proxy studies (Ezat et al., 2014; El bani Altuna et al., 2021) showing warming of intermediate waters during other cold stadial periods.
- Brine formation is likely to have only had a small/no influence on the low δ^{18}O signal since the planktic δ^{18}O is significantly higher than the typical values of fresh water in the Arctic and the relatively constant *N. pachyderma* δ^{13}C record indicates that no significant change in surface water properties occurred during the YD. There are additionally no modern analogues in the Arctic which support this (Rasmussen and Thomsen, 2009).
- The low δ^{18}O during the YD is concurrent with high local sea ice cover (higher IP_{25}) (Pieńkowski et al., 2021) and a weakened AMOC (increased R-ages and ^{231}Pa/^{230}Th) (Ng et al., 2018; Skinner et al., 2021), possibly indicating that increased sea ice extent during the YD, reduced the path length of AW heat loss, in turn increasing AW buoyancy and reducing deep water formation and thus resulting in a weakened AMOC, as has been seen to occur in models during stadial periods (Mignot et al., 2007).
- During the late YD (~12 000 cal yr BP) the increase in productivity (δ^{13}C pore water gradient), decrease in sea ice coverage (decreased IP_{25}), northward shift of the Polar Front, increase an AMOC and rapid decrease in ocean temperatures (increased δ^{18}O) together indicate destabilization of the cold stadial (Bakke et al., 2009). When

sea ice started to decline heat flux increased, cooling the intermediate water and deep water formation recovered.

- The early Holocene sees a shift to more saline and colder ocean temperatures, with increased overturning circulation and reduced influence of sea ice, which agrees with the findings from other records from the area (Kristensen et al., 2013; Ivanova et al., 2019).

Future Outlook?

This thesis therefore provides new information on how the properties of AW inflow in the north-western Barents Sea has varied since the last deglaciation and its possible relationship to sea ice and overturning circulation, showing that it is similar to other stadial periods. This is consistent with recent work suggesting that the overall pattern of changes during the YD is statistically indistinguishable from the millennial events preceding it (Nye and Condron, 2021). To confirm that intermediate ocean temperatures increased during the YD, independent temperature proxies such as Mg/Ca or clumped isotope analysis on these samples should be a high priority for further research. A pilot Mg/Ca project has been done in this thesis (see Appendix D). Unfortunately, the results preliminary results are inconclusive due to the low sensitivity and high calibration errors of this proxy (and species available) at low temperatures combined with the small number of data points resulting from the scarcity of foraminifera. Additionally, sea ice proxies for the Nordic Seas with precise dating (e.g., tephra and co-registered proxy signals from within the same core) would enable better establishment of the lead-lag relationships of sea ice, ocean circulation and ocean temperatures during this period.

9. References

ALVES, E. Q., MACARIO, K., ASCOUGH, P. & BRONK RAMSEY, C. 2018. The Worldwide Marine Radiocarbon Reservoir Effect: Definitions, Mechanisms, and Prospects. *Reviews of Geophysics,* 56**,** 278-305.

ALVES, E. Q., MACARIO, K. D., URRUTIA, F. P., CARDOSO, R. P. & BRONK RAMSEY, C. 2019. Accounting for the marine reservoir effect in radiocarbon calibration. *Quaternary Science Reviews,* 209**,** 129-138.

ÅRTHUN, M., ELDEVIK, T., SMEDSRUD, L., SKAGSETH, Ø. & INGVALDSEN, R. 2012. Quantifying the influence of Atlantic heat on Barents Sea ice variability and retreat. *Journal of Climate,* 25**,** 4736-4743.

ÅRTHUN, M., ELDEVIK, T. & SMEDSRUD, L. H. 2019. The role of Atlantic heat transport in future Arctic winter sea ice loss. *Journal of Climate,* 32**,** 3327-3341.

AUSTIN, W. E. N., TELFORD, R. J., NINNEMANN, U. S., BROWN, L., WILSON, L. J., SMALL, D. P. & BRYANT, C. L. 2011. North Atlantic reservoir ages linked to high Younger Dryas atmospheric radiocarbon concentrations. *Global and Planetary Change,* 79**,** 226-233.

BAGNIEWSKI, W., MEISSNER, K. J., MENVIEL, L. & BRENNAN, C. E. 2015. Quantification of factors impacting seawater and calcite δ18O during Heinrich Stadials 1 and 4. *Paleoceanography,* 30**,** 895-911.

BAKKE, J., LIE, Ø., HEEGAARD, E., DOKKEN, T., HAUG, G. H., BIRKS, H. H., DULSKI, P. & NILSEN, T. 2009. Rapid oceanic and atmospheric changes during the Younger Dryas cold period. *Nature Geoscience,* 2**,** 202-205.

BARD, E. 1988. Correction of accelerator mass spectrometry 14C ages measured in planktonic foraminifera: Paleoceanographic implications. *Paleoceanography,* 3**,** 635-645.

BARRIENTOS, N., LEAR, C. H., JAKOBSSON, M., STRANNE, C., O'REGAN, M., CRONIN, T. M., GUKOV, A. Y. & COXALL, H. K. 2018. Arctic Ocean benthic foraminifera Mg/Ca ratios and global Mg/Ca-temperature calibrations: New constraints at low temperatures. *Geochimica et Cosmochimica Acta,* 236**,** 240-259.

BARTELS, M., TITSCHACK, J., FAHL, K., STEIN, R., SEIDENKRANTZ, M.-S., HILLAIRE-MARCEL, C. & HEBBELN, D. 2017. Atlantic Water advection vs. glacier dynamics in northern Spitsbergen since early deglaciation. *Climate of the Past,* 13**,** 1717-1749.

BARTON, B. I., LENN, Y.-D. & LIQUE, C. 2018. Observed Atlantification of the Barents Sea Causes the Polar Front to Limit the Expansion of Winter Sea Ice. *Journal of Physical Oceanography,* 48**,** 1849-1866.

BATTAGLIA, G., STEINACHER, M. & JOOS, F. 2016. A probabilistic assessment of calcium carbonate export and dissolution in the modern ocean. *Biogeosciences,* 13**,** 2823-2848.

BÉ, A. 1980. Gametogenic calcification in a spinose planktonic foraminifer, Globigerinoides sacculifer (Brady). *Marine Micropaleontology,* 5**,** 283-310.

BELLA, F., ALESSIO, M. & FRATELLI, P. 1968. A determination of the half-life of 14 C. *Il Nuovo Cimento B (1965-1970),* 58**,** 232-246.

BLAAUW, M. & CHRISTEN, J. A. 2011. Flexible paleoclimate age-depth models using an autoregressive gamma process. *Bayesian Analysis,* 6.

BLAAUW, M. & CHRISTEN, J. A. 2013. Bacon Manual v2.2.

BÖHM, E., LIPPOLD, J., GUTJAHR, M., FRANK, M., BLASER, P., ANTZ, B., FOHLMEISTER, J., FRANK, N., ANDERSEN, M. B. & DEININGER, M. 2015. Strong and deep Atlantic meridional overturning circulation during the last glacial cycle. *Nature,* 517**,** 73-6.

BOND, G., HEINRICH, H., BROECKER, W., LABEYRIE, L., MCMANUS, J., ANDREWS, J., HUON, S., JANTSCHIK, R., CLASEN, S. & SIMET, C. 1992. Evidence for massive discharges of icebergs into the North Atlantic ocean during the last glacial period. *Nature,* 360**,** 245-249.

BOWMAN, S. 1990. *Radiocarbon dating*, Univ of California Press.

BOYLE, E. A. & KEIGWIN, L. 1987. North Atlantic thermohaline circulation during the past 20,000 years linked to high-latitude surface temperature. *Nature,* 330**,** 35-40.

BRADLEY, R. S. 2015. Chapter 2 - Climate and Climatic Variation. *In:* BRADLEY, R. S. (ed.) *Paleoclimatology (Third Edition).* San Diego: Academic Press.

BRADLEY, R. S. & ENGLAND, J. H. 2008. The Younger Dryas and the Sea of Ancient Ice. *Quaternary Research,* 70**,** 1-10.

BRADY, E. C. & OTTO-BLIESNER, B. L. 2010. The role of meltwater-induced subsurface ocean warming in regulating the Atlantic meridional overturning in glacial climate simulations. *Climate Dynamics,* 37**,** 1517-1532.

BROECKER, W. S., DENTON, G. H., EDWARDS, R. L., CHENG, H., ALLEY, R. B. & PUTNAM, A. E. 2010. Putting the Younger Dryas cold event into context. *Quaternary Science Reviews,* 29**,** 1078-1081.

BROECKER, W. S. & MAIER-REIMER, E. 1992. The influence of air and sea exchange on the carbon isotope distribution in the sea. *Global Biogeochemical Cycles,* 6**,** 315-320.

BURDIGE, D. J. 1993. The biogeochemistry of manganese and iron reduction in marine sediments. *Earth-Science Reviews,* 35**,** 249-284.

BUTZIN, M., KÖHLER, P. & LOHMANN, G. 2017. Marine radiocarbon reservoir age simulations for the past 50,000 years. *Geophysical Research Letters,* 44**,** 8473-8480.

CAGE, A. G., PIEŃKOWSKI, A. J., JENNINGS, A., KNUDSEN, K. L. & SEIDENKRANTZ, M.-S. 2021. Comparative analysis of six common foraminiferal species of the genera Cassidulina, Paracassidulina, and Islandiella from the Arctic–North Atlantic domain. *Journal of Micropalaeontology,* 40**,** 37-60.

CARSTENS, J. & WEFER, G. 1992. Recent distribution of planktonic foraminifera in the Nansen Basin, Arctic Ocean. *Deep Sea Research Part A. Oceanographic Research Papers,* 39**,** S507-S524.

CHAUHAN, T., RASMUSSEN, T. L. & NOORMETS, R. 2016. Palaeoceanography of the Barents Sea continental margin, north of Nordaustlandet, Svalbard, during the last 74 ka. *Boreas,* 45**,** 76-99.

CHAVE, K. E. 1954. Aspects of the biogeochemistry of magnesium 1. Calcareous marine organisms. *The Journal of Geology,* 62**,** 266-283.

CHENG, H., ZHANG, H., SPOTL, C., BAKER, J., SINHA, A., LI, H., BARTOLOME, M., MORENO, A., KATHAYAT, G., ZHAO, J., DONG, X., LI, Y., NING, Y., JIA, X., ZONG, B., AIT BRAHIM, Y., PEREZ-MEJIAS, C., CAI, Y., NOVELLO, V. F., CRUZ, F. W., SEVERINGHAUS, J. P., AN, Z. & EDWARDS, R. L. 2020. Timing and structure of the Younger Dryas event and its underlying climate dynamics. *Proc Natl Acad Sci U S A,* 117**,** 23408-23417.

CONSOLARO, C., RASMUSSEN, T. L. & PANIERI, G. 2018. Palaeoceanographic and environmental changes in the eastern Fram Strait during the last 14,000 years based on benthic and planktonic foraminifera. *Marine Micropaleontology,* 139**,** 84-101.

CRONIN, T. M., SEIDENSTEIN, J., KELLER, K., MCDOUGALL, K., RUEFER, A. & GEMERY, L. 2019. The benthic foraminifera Cassidulina from the Arctic Ocean: application to paleoceanography and biostratigraphy. *Micropaleontology,* 65**,** 105-125.

CROUDACE, I. W., RINDBY, A. & ROTHWELL, R. G. 2006. ITRAX: description and evaluation of a new multi-function X-ray core scanner. *Geological Society, London, Special Publications,* 267**,** 51-63.

CURRY, W. B., DUPLESSY, J. C., LABEYRIE, L. D. & SHACKLETON, N. J. 1988. Changes in the distribution of δ13C of deep water ΣCO2 between the Last Glaciation and the Holocene. *Paleoceanography,* 3**,** 317-341.

CURRY, W. B. & OPPO, D. W. 2005. Glacial water mass geometry and the distribution of δ13C of ΣCO2in the western Atlantic Ocean. *Paleoceanography,* 20**,** n/a-n/a.

DARLING, K. F., KUCERA, M., KROON, D. & WADE, C. M. 2006. A resolution for the coiling direction paradox in Neogloboquadrina pachyderma. *Paleoceanography,* 21.

DAVIS, C. V., FEHRENBACHER, J. S., HILL, T. M., RUSSELL, A. D. & SPERO, H. J. 2017. Relationships Between Temperature, pH, and Crusting on Mg/Ca Ratios in Laboratory-GrownNeogloboquadrinaForaminifera. *Paleoceanography,* 32**,** 1137-1152.

DOKKEN, T. M. & JANSEN, E. 1999. Rapid changes in the mechanism of ocean convection during the last glacial period. *Nature,* 401**,** 458-461.

DOKKEN, T. M., NISANCIOGLU, K. H., LI, C., BATTISTI, D. S. & KISSEL, C. 2013. Dansgaard-Oeschger cycles: Interactions between ocean and sea ice intrinsic to the Nordic seas. *Paleoceanography,* 28**,** 491-502.

DOWDESWELL, J. A., HOGAN, K. A., EVANS, J., NOORMETS, R., Ó COFAIGH, C. & OTTESEN, D. 2010. Past ice-sheet flow east of Svalbard inferred from streamlined subglacial landforms. *Geology,* 38**,** 163-166.

DUPLESSY, J., SHACKLETON, N., FAIRBANKS, R., LABEYRIE, L., OPPO, D. & KALLEL, N. 1988. Deepwater source variations during the last climatic cycle and their impact on the global deepwater circulation. *Paleoceanography,* 3**,** 343-360.

DUPLESSY, J.-C., CORTIJO, E., IVANOVA, E., KHUSID, T., LABEYRIE, L., LEVITAN, M., MURDMAA, I. & PATERNE, M. 2005. Paleoceanography of the Barents Sea during the Holocene. *Paleoceanography,* 20.

DUPLESSY, J.-C., IVANOVA, E., MURDMAA, I., PATERNE, M. & LABEYRIE, L. 2001. Holocene paleoceanography of the northern Barents Sea and variations of the northward heat transport by the Atlantic Ocean. *Boreas,* 30**,** 2-16.

EIDE, M., OLSEN, A., NINNEMANN, U. S. & JOHANNESSEN, T. 2017. A global ocean climatology of preindustrial and modern ocean δ13C. *Global Biogeochemical Cycles,* 31**,** 515-534.

EL BANI ALTUNA, N., EZAT, M. M., GREAVES, M. & RASMUSSEN, T. L. 2021. Millennial-Scale Changes in Bottom Water Temperature and Water Mass Exchange Through the Fram Strait 79°N, 63-13 ka. *Paleoceanography and Paleoclimatology,* 36.

ELVERHØI, A. & LAURITZEN, Ø. 1984. Bedrock geology of the northern Barents Sea (west of 35 E) as inferred from the overlying Quaternary deposits. *Skrifter-Norsk Polarinstitutt***,** 5-16.

EMILIANI, C. 1955. Pleistocene temperatures. *The Journal of geology,* 63**,** 538-578.

EPSTEIN, S., BUCHSBAUM, R., LOWENSTAM, H. & UREY, H. C. 1951. CARBONATE-WATER ISOTOPIC TEMPERATURE SCALE. Boulder, Colo.

EZAT, M. M., RASMUSSEN, T. L. & GROENEVELD, J. 2014. Persistent intermediate water warming during cold stadials in the southeastern Nordic seas during the past 65 k.y. *Geology,* 42**,** 663-666.

FAIRBANKS, R. G. 1989. A 17,000-year glacio-eustatic sea level record: influence of glacial melting rates on the Younger Dryas event and deep-ocean circulation. *Nature,* 342**,** 637-642.

FALARDEAU, J., DE VERNAL, A. & SPIELHAGEN, R. F. 2018. Paleoceanography of northeastern Fram Strait since the last glacial maximum: Palynological evidence of large amplitude changes. *Quaternary Science Reviews,* 195**,** 133-152.

FIRESTONE, R. B., WEST, A., KENNETT, J. P., BECKER, L., BUNCH, T. E., REVAY, Z. S., SCHULTZ, P. H., BELGYA, T., KENNETT, D. & ERLANDSON, J. 2007. Evidence for an extraterrestrial impact 12,900 years ago that contributed to the megafaunal extinctions and the Younger Dryas cooling. *Proceedings of the National Academy of Sciences,* 104**,** 16016-16021.

FOSSILE, E., NARDELLI, M. P., JOUINI, A., LANSARD, B., PUSCEDDU, A., MOCCIA, D., MICHEL, E., PÉRON, O., HOWA, H. & MOJTAHID, M. 2020. Benthic foraminifera as tracers of brine production in the Storfjorden "sea ice factory". *Biogeosciences,* 17**,** 1933-1953.

FUREVIK, T., MAURITZEN, C. & INGVALDSEN, R. 2007. The flow of Atlantic water to the Nordic Seas and Arctic Ocean. *Arctic alpine ecosystems and people in a changing environment.* Springer.

GRECO, M., JONKERS, L., KRETSCHMER, K., BIJMA, J. & KUCERA, M. 2019. Depth habitat of the planktonic foraminifera Neogloboquadrina pachyderma in the northern high latitudes explained by sea-ice and chlorophyll concentrations. *Biogeosciences,* 16**,** 3425-3437.

GUNN, D. E. & BEST, A. I. 1998. A new automated nondestructive system for high resolution multi-sensor core logging of open sediment cores. *Geo-Marine Letters,* 18**,** 70-77.

HALD, M. & KORSUN, S. 1997. Distribution of modern benthic foraminifera from fjords of Svalbard, European Arctic. *The Journal of Foraminiferal Research,* 27**,** 101-122.

HALL, J. M. & CHAN, L. H. 2004. Ba/Ca inNeogloboquadrina pachydermaas an indicator of deglacial meltwater discharge into the western Arctic Ocean. *Paleoceanography,* 19.

HE, C., LIU, Z., ZHU, J., ZHANG, J., GU, S., OTTO-BLIESNER, B. L., BRADY, E., ZHU, C., JIN, Y. & SUN, J. 2020. North Atlantic subsurface temperature response controlled by effective freshwater input in "Heinrich" events. *Earth and Planetary Science Letters,* 539.

HEATON, T. J., KÖHLER, P., BUTZIN, M., BARD, E., REIMER, R. W., AUSTIN, W. E. N., BRONK RAMSEY, C., GROOTES, P. M., HUGHEN, K. A., KROMER, B., REIMER, P. J., ADKINS, J., BURKE, A., COOK, M. S., OLSEN, J. & SKINNER, L. C. 2020. Marine20—The Marine Radiocarbon Age Calibration Curve (0–55,000 cal BP). *Radiocarbon,* 62**,** 779-820.

HEMMING, S. R. 2004. Heinrich events: Massive late Pleistocene detritus layers of the North Atlantic and their global climate imprint. *Reviews of Geophysics,* 42.

HENRY, L., MCMANUS, J., CURRY, W., ROBERTS, N., PIOTROWSKI, A. & KEIGWIN, L. 2016. North Atlantic ocean circulation and abrupt climate change during the last glaciation. *Science,* 353**,** 470-474.

HOFF, U., RASMUSSEN, T. L., STEIN, R., EZAT, M. M. & FAHL, K. 2016. Sea ice and millennial-scale climate variability in the Nordic seas 90 kyr ago to present. *Nature communications,* 7**,** 1-10.

HOGAN, K. A., DOWDESWELL, J. A., NOORMETS, R., EVANS, J., Ó COFAIGH, C. & JAKOBSSON, M. 2010. Submarine landforms and ice-sheet flow in the Kvitøya Trough, northwestern Barents Sea. *Quaternary Science Reviews,* 29**,** 3545-3562.

HUGHES, A. L. C., GYLLENCREUTZ, R., LOHNE, Ø. S., MANGERUD, J. & SVENDSEN, J. I. 2015. The last Eurasian ice sheets – a chronological database and time-slice reconstruction, DATED-1. *Boreas,* 45**,** 1-45.

HUNT, A. S. & CORLISS, B. H. 1993. Distribution and microhabitats of living (stained) benthic foraminifera from the Canadian Arctic Archipelago. *Marine Micropaleontology,* 20**,** 321-345.

HUSUM, K., NINNEMANN, U., RYDNINGEN, T. A., ALVE, E., ALTUNA, N. E. B., BRAATEN, A. H., EILERTSEN, V., GAMBOA, V., KJØLLER, M. R., ORME, L., RUTLEDAL, S., TESSIN, A. & ZINDORF, M. 2020. Paleo Cruise 2018: Cruise Report. The Nansen Legacy Report Series 3/2020.

INGÓLFSSON, Ó. & LANDVIK, J. Y. 2013. The Svalbard–Barents Sea ice-sheet–Historical, current and future perspectives. *Quaternary Science Reviews,* 64**,** 33-60.

IVANOVA, E., MURDMAA, I., DE VERNAL, A., RISEBROBAKKEN, B., PEYVE, A., BRICE, C., SEITKALIEVA, E. & PISAREV, S. 2019. Postglacial paleoceanography and paleoenvironments in the northwestern Barents Sea. *Quaternary Research,* 92**,** 430-449.

IVANOVA, E. V., OVSEPYAN, E. A., RISEBROBAKKEN, B. & VETROV, A. A. 2008. Downcore distribution of living calcareous foraminifera and stable isotopes in the western Barents Sea. *The Journal of Foraminiferal Research,* 38**,** 337-356.

JANSEN, E., BLEIL, U., HENRICH, R., KRINGSTAD, L. & SLETTEMARK, B. 1988. Paleoenvironmental changes in the Norwegian Sea and the northeast Atlantic during the last 2.8 my: Deep Sea Drilling Project/Ocean Drilling Program sites 610, 642, 643 and 644. *Paleoceanography,* 3**,** 563-581.

JENSEN, M. F., NISANCIOGLU, K. H. & SPALL, M. A. 2018. Large Changes in Sea Ice Triggered by Small Changes in Atlantic Water Temperature. *Journal of Climate,* 31**,** 4847-4863.

KATSEV, S., SUNDBY, B. & MUCCI, A. 2006. Modeling vertical excursions of the redox boundary in sediments: Application to deep basins of the Arctic Ocean. *Limnology and Oceanography,* 51**,** 1581-1593.

KLEIBER, H., KNIES, J. & NIESSEN, F. 2000. The Late Weichselian glaciation of the Franz Victoria Trough, northern Barents Sea: ice sheet extent and timing. *Marine Geology,* 168**,** 25-44.

KNUTTI, R., FLÜCKIGER, J., STOCKER, T. & TIMMERMANN, A. 2004. Strong hemispheric coupling of glacial climate through freshwater discharge and ocean circulation. *Nature,* 430**,** 851-856.

KOÇ, N., KLITGAARD-KRISTENSEN, D., HASLE, K., FORSBERG, C. F. & SOLHEIM, A. 2002. Late glacial palaeoceanography of Hinlopen Strait, northern Svalbard. *Polar Research,* 21**,** 307-314.

KOHFELD, K. E., FAIRBANKS, R. G., SMITH, S. L. & WALSH, I. D. 1996. Neogloboquadrina pachyderma (sinistral coiling) as paleoceanographic tracers in polar oceans: Evidence from Northeast Water Polynya plankton tows, sediment traps, and surface sediments. *Paleoceanography,* 11**,** 679-699.

KOZDON, R., EISENHAUER, A., WEINELT, M., MELAND, M. Y. & NÜRNBERG, D. 2009. Reassessing Mg/Ca temperature calibrations ofNeogloboquadrina pachyderma(sinistral) using pairedδ44/40Ca and Mg/Ca measurements. *Geochemistry, Geophysics, Geosystems,* 10**,** n/a-n/a.

KOZDON, R., USHIKUBO, T., KITA, N. & VALLEY, J. 2008. Intratest oxygen isotope variability in planktonic foraminifera: New insights from in situ measurements by ion microprobe. *Geochimica et Cosmochimica Acta Supplement,* 72**,** A496.

KRISTENSEN, D. K., RASMUSSEN, T. L. & KOÇ, N. 2013. Palaeoceanographic changes in the northern Barents Sea during the last 16 000 years - new constraints on the last deglaciation of the Svalbard-Barents Sea Ice Sheet. *Boreas,* 42**,** 798-813.

KRISTJÁNSDÓTTIR, G. B., LEA, D. W., JENNINGS, A. E., PAK, D. K. & BELANGER, C. 2007. New spatial Mg/Ca-temperature calibrations for three Arctic, benthic foraminifera and reconstruction of north Iceland shelf temperature for the past 4000 years. *Geochemistry, Geophysics, Geosystems,* 8**,** n/a-n/a.

KUHLBRODT, T., GRIESEL, A., MONTOYA, M., LEVERMANN, A., HOFMANN, M. & RAHMSTORF, S. 2007. On the driving processes of the Atlantic meridional overturning circulation. *Reviews of Geophysics,* 45.

LAMBECK, K., ROUBY, H., PURCELL, A., SUN, Y. & SAMBRIDGE, M. 2014. Sea level and global ice volumes from the Last Glacial Maximum to the Holocene. *Proc Natl Acad Sci U S A,* 111**,** 15296-303.

LAZAR, K. B., POLYAK, L. & DIPRE, G. R. 2016. Re-examination of the use of Cassidulina neoteretis as a Pleistocene biostratigraphic marker in the Arctic Ocean. *The Journal of Foraminiferal Research,* 46**,** 115-123.

LEFÈVERE, S. 2021. Natural variability of the Atlantic Water inflow to the Arctic during the last deglaciation. Masters Thesis.

LEGRANDE, A. N. & SCHMIDT, G. A. 2006. Global gridded data set of the oxygen isotopic composition in seawater. *Geophysical Research Letters,* 33.

LIVSEY, C. M., KOZDON, R., BAUCH, D., BRUMMER, G. J. A., JONKERS, L., ORLAND, I., HILL, T. M. & SPERO, H. J. 2020. High-Resolution Mg/Ca and δ18O Patterns in Modern Neogloboquadrina pachyderma From the Fram Strait and Irminger Sea. *Paleoceanography and Paleoclimatology,* 35.

LOHNE, Ø. S., BONDEVIK, S., MANGERUD, J. & SVENDSEN, J. I. 2007. Sea-level fluctuations imply that the Younger Dryas ice-sheet expansion in western Norway commenced during the Allerød. *Quaternary Science Reviews,* 26**,** 2128-2151.

LÖWEMARK, L., JAKOBSSON, M., MÖRTH, M. & BACKMAN, J. 2016. Arctic Ocean manganese contents and sediment colour cycles. *Polar Research,* 27**,** 105-113.

LUBINSKI, D., POLYAK, L. & FORMAN, S. 2001. Freshwater and Atlantic water inflows to the deep northern Barents and Kara seas since ca 13 14C ka:: foraminifera and stable isotopes. *Quaternary Science Reviews,* 20**,** 1851-1879.

LUMPKIN, R. & SPEER, K. 2003. Large-scale vertical and horizontal circulation in the North Atlantic Ocean. *Journal of Physical Oceanography,* 33**,** 1902-1920.

LYNCH-STIEGLITZ, J., ADKINS, J. F., CURRY, W. B., DOKKEN, T., HALL, I. R., HERGUERA, J. C., HIRSCHI, J. J.-M., IVANOVA, E. V., KISSEL, C. & MARCHAL, O. 2007. Atlantic meridional overturning circulation during the Last Glacial Maximum. *science,* 316**,** 66-69.

MACKENSEN, A. & SCHMIEDL, G. 2016. Brine formation recorded by stable isotopes of Recent benthic foraminifera in Storfjorden, Svalbard: palaeoceanographical implications. *Boreas,* 45**,** 552-566.

MACKENSEN, A. & SCHMIEDL, G. 2019. Stable carbon isotopes in paleoceanography: atmosphere, oceans, and sediments. *Earth-Science Reviews,* 197**,** 102893.

MANGERUD, J. 2021. The discovery of the Younger Dryas, and comments on the current meaning and usage of the term. *Boreas,* 50**,** 1-5.

MANGERUD, J., BONDEVIK, S., GULLIKSEN, S., KARIN HUFTHAMMER, A. & HØISÆTER, T. 2006. Marine 14C reservoir ages for 19th century whales and molluscs from the North Atlantic. *Quaternary Science Reviews,* 25**,** 3228-3245.

MANGERUD, J. & GULLIKSEN, S. 1975. Apparent radiocarbon ages of recent marine shells from Norway, Spitsbergen, and Arctic Canada. *Quaternary Research,* 5**,** 263-273.

MAURITZEN, C. 1996. Production of dense overflow waters feeding the North Atlantic across the Greenland-Scotland Ridge. Part 1: Evidence for a revised circulation scheme. *Deep Sea Research Part I: Oceanographic Research Papers,* 43**,** 769-806.

MCCORKLE, D. C. & EMERSON, S. R. 1988. The relationship between pore water carbon isotopic composition and bottom water oxygen concentration. *Geochimica et Cosmochimica Acta,* 52**,** 1169-1178.

MCCORKLE, D. C., EMERSON, S. R. & QUAY, P. D. 1985. Stable carbon isotopes in marine porewaters. *Earth and Planetary Science Letters,* 74**,** 13-26.

MCMANUS, J. F., FRANCOIS, R., GHERARDI, J.M., KEIGWIN, L.D. AND BROWN-LEGER, S. 2004. Collapse and rapid resumption of Atlantic meridional circulation linked to deglacial climate changes. *Nature*.

MENZE, S., INGVALDSEN, R. B., NIKOLOPOULOS, A., HATTERMANN, T., ALBRETSEN, J. & GJØSÆTER, H. 2020. Productive detours – Atlantic water inflow and acoustic backscatter in the major troughs along the Svalbard shelf. *Progress in Oceanography,* 188.

MIGNOT, J., GANOPOLSKI, A. & LEVERMANN, A. 2007. Atlantic Subsurface Temperatures: Response to a Shutdown of the Overturning Circulation and Consequences for Its Recovery. *Journal of Climate,* 20**,** 4884-4898.

NG, H. C., ROBINSON, L. F., MCMANUS, J. F., MOHAMED, K. J., JACOBEL, A. W., IVANOVIC, R. F., GREGOIRE, L. J. & CHEN, T. 2018. Coherent deglacial changes in western Atlantic Ocean circulation. *Nat Commun,* 9**,** 2947.

NUERNBERG, D. 1995. Magnesium in tests of Neogloboquadrina pachyderma sinistral from high northern and southern latitudes. *The Journal of Foraminiferal Research,* 25**,** 350-368.

NYE, H. & CONDRON, A. 2021. Assessing the statistical uniqueness of the Younger Dryas: a robust multivariate analysis. *Climate of the Past,* 17**,** 1409-1421.

ÖSTLUND, H. G., POSSNERT, G. & SWIFT, J. H. 1987. Ventilation rate of the deep Arctic Ocean from carbon 14 data. *Journal of Geophysical Research,* 92.

PACHAURI, R. K., ALLEN, M. R., BARROS, V. R., BROOME, J., CRAMER, W., CHRIST, R., CHURCH, J. A., CLARKE, L., DAHE, Q. & DASGUPTA, P. 2014. *Climate change 2014: synthesis report. Contribution of Working Groups I, II and III to the fifth assessment report of the Intergovernmental Panel on Climate Change*, Ipcc.

PEARCE, C., SEIDENKRANTZ, M. S., KUIJPERS, A., MASSE, G., REYNISSON, N. F. & KRISTIANSEN, S. M. 2013. Ocean lead at the termination of the Younger Dryas cold spell. *Nat Commun,* 4**,** 1664.

PEARSON, P. N. 2012. Oxygen isotopes in foraminifera: Overview and historical review. *Paleontological Society Papers,* 18**,** 1-38.

PÉREZ-HERNÁNDEZ, M. D., PICKART, R. S., PAVLOV, V., VÅGE, K., INGVALDSEN, R., SUNDFJORD, A., RENNER, A. H. H., TORRES, D. J. & EROFEEVA, S. Y. 2017. The Atlantic Water boundary current north of Svalbard in late summer. *Journal of Geophysical Research: Oceans,* 122**,** 2269-2290.

PIEŃKOWSKI, A. J., HUSUM, K., BELT, S. T., NINNEMANN, U., KÖSEOĞLU, D., DIVINE, D. V., SMIK, L., KNIES, J., HOGAN, K. & NOORMETS, R. 2021. Seasonal sea ice persisted through the Holocene Thermal Maximum at 80°N. *Communications Earth & Environment,* 2.

POLYAKOV, I. V., PNYUSHKOV, A. V., ALKIRE, M. B., ASHIK, I. M., BAUMANN, T. M., CARMACK, E. C., GOSZCZKO, I., GUTHRIE, J., IVANOV, V. V. & KANZOW, T. 2017. Greater role for Atlantic inflows on sea-ice loss in the Eurasian Basin of the Arctic Ocean. *Science,* 356**,** 285-291.

QUARTA, G., MARUCCIO, L., D’ELIA, M. & CALCAGNILE, L. 2021. Radiocarbon Dating of Marine Samples: Methodological Aspects, Applications and Case Studies. *Water,* 13.

RAHMSTORF, S. 2006. Thermohaline ocean circulation. *Encyclopedia of quaternary sciences,* 5.

RAHMSTORF, S. & ALLEY, R. 2002. Stochastic resonance in glacial climate. *Eos, Transactions American Geophysical Union,* 83**,** 129-135.

RASMUSSEN, T. L. & THOMSEN, E. 2004. The role of the North Atlantic Drift in the millennial timescale glacial climate fluctuations. *Palaeogeography, Palaeoclimatology, Palaeoecology,* 210**,** 101-116.

RASMUSSEN, T. L. & THOMSEN, E. 2009. Stable isotope signals from brines in the Barents Sea: Implications for brine formation during the last glaciation. *Geology,* 37**,** 903-906.

RASMUSSEN, T. L., THOMSEN, E., LABEYRIE, L. & VAN WEERING, T. C. 1996. Circulation changes in the Faeroe-Shetland Channel correlating with cold events during the last glacial period (58–10 ka). *Geology,* 24**,** 937-940.

RASMUSSEN, T. L., THOMSEN, E., ŚLUBOWSKA, M. A., JESSEN, S., SOLHEIM, A. & KOÇ, N. 2007. Paleoceanographic evolution of the SW Svalbard margin (76 N) since 20,000 14C yr BP. *Quaternary Research,* 67**,** 100-114.

RAVELO, A. C. & HILLAIRE-MARCEL, C. 2007. Chapter eighteen the use of oxygen and carbon isotopes of foraminifera in paleoceanography. *Developments in marine geology,* 1**,** 735-764.

REIMER, P. J., AUSTIN, W. E., BARD, E., BAYLISS, A., BLACKWELL, P. G., RAMSEY, C. B., BUTZIN, M., CHENG, H., EDWARDS, R. L. & FRIEDRICH, M. 2020. The IntCal20 Northern Hemisphere radiocarbon age calibration curve (0–55 cal kBP). *Radiocarbon,* 62**,** 725-757.

REIMER, R. W. & REIMER, P. J. 2017. An online application for ΔR calculation. *Radiocarbon,* 59**,** 1623-1627.

RENNER, A. H. H., SUNDFJORD, A., JANOUT, M. A., INGVALDSEN, R. B., BESZCZYNSKA-MÖLLER, A., PICKART, R. S. & PÉREZ-HERNÁNDEZ, M. D. 2018. Variability and Redistribution of Heat in the Atlantic Water Boundary Current North of Svalbard. *Journal of Geophysical Research: Oceans,* 123**,** 6373-6391.

RENSSEN, H., MAIRESSE, A., GOOSSE, H., MATHIOT, P., HEIRI, O., ROCHE, D. M., NISANCIOGLU, K. H. & VALDES, P. J. 2015. Multiple causes of the Younger Dryas cold period. *Nature Geoscience,* 8**,** 946-949.

ROHLING, E. J. & COOKE, S. 2003. Stable oxygen and carbon isotopes in foraminiferal carbonate shells. *Modern Foraminifera.* Dordrecht: Springer Netherlands.

ROSENTHAL, Y., BOYLE, E. A. & SLOWEY, N. 1997. Temperature control on the incorporation of magnesium, strontium, fluorine, and cadmium into benthic foraminiferal shells from Little Bahama Bank: Prospects for thermocline paleoceanography. *Geochimica et Cosmochimica Acta,* 61**,** 3633-3643.

ROTHWELL, R. G. & CROUDACE, I. W. 2015. Twenty Years of XRF Core Scanning Marine Sediments: What Do Geochemical Proxies Tell Us? *Micro-XRF Studies of Sediment Cores.*

RUDDIMAN, W. F. 2001. *Earth's Climate: past and future*, Macmillan.

RUDELS, B. 2009. Arctic ocean circulation.

RUDELS, B., ANDERSON, L., ERIKSSON, P., FAHRBACH, E., JAKOBSSON, M., JONES, E. P., MELLING, H., PRINSENBERG, S., SCHAUER, U. & YAO, T. 2012. Observations in the Ocean. *Arctic Climate Change.*

SCHMIEDL, G. & MACKENSEN, A. 2006. Multispecies stable isotopes of benthic foraminifers reveal past changes of organic matter decomposition and deepwater oxygenation in the Arabian Sea. *Paleoceanography,* 21.

SCHOMACKER, A., FARNSWORTH, W. R., INGOLFSSON, O., ALLAART, L., HAKANSSON, L., RETELLE, M., SIGGAARD-ANDERSEN, M. L., KORSGAARD, N. J., ROUILLARD, A. & KJELLMAN, S. E. 2019. Postglacial relative sea level change and glacier activity in the early and late Holocene: Wahlenbergfjorden, Nordaustlandet, Svalbard. *Sci Rep,* 9**,** 6799.

SEIDENKRANTZ, M.-S. 1995. Cassidulina teretis Tappan and Cassidulina neoteretis new species (Foraminifera): stratigraphic markers for deep sea and outer shelf areas. *Journal of Micropalaeontology,* 14**,** 145-157.

SEN GUPTA, B. K. 1999. *Modern foraminifera,* Dordrecht, Kluwer.

SESSFORD, E., TISSERAND, A. A., RISEBROBAKKEN, B., ANDERSSON, C., DOKKEN, T. & JANSEN, E. 2018. High-Resolution Benthic Mg/Ca Temperature Record of the Intermediate

Water in the Denmark Strait Across D-O Stadial-Interstadial Cycles. *Paleoceanography and Paleoclimatology,* 33, 1169-1185.

SESSFORD, E. G., JENSEN, M. F., TISSERAND, A. A., MUSCHITIELLO, F., DOKKEN, T., NISANCIOGLU, K. H. & JANSEN, E. 2019. Consistent fluctuations in intermediate water temperature off the coast of Greenland and Norway during Dansgaard-Oeschger events. *Quaternary Science Reviews,* 223.

SHACKLETON, N. J. & OPDYKE, N. D. 1973. Oxygen Isotope and Palaeomagnetic Stratigraphy of Equatorial Pacific Core V28-238: Oxygen Isotope Temperatures and Ice Volumes on a 105 Year and 106 Year Scale. *Quaternary Research,* 3, 39-55.

SHAKUN, J. D., CLARK, P. U., HE, F., MARCOTT, S. A., MIX, A. C., LIU, Z., OTTO-BLIESNER, B., SCHMITTNER, A. & BARD, E. 2012. Global warming preceded by increasing carbon dioxide concentrations during the last deglaciation. *Nature,* 484, 49-54.

SKINNER, L. C., FREEMAN, E., HODELL, D., WAELBROECK, C., VAZQUEZ RIVEIROS, N. & SCRIVNER, A. E. 2021. Atlantic Ocean Ventilation Changes Across the Last Deglaciation and Their Carbon Cycle Implications. *Paleoceanography and Paleoclimatology,* 36.

SKINNER, L. C., MUSCHITIELLO, F. & SCRIVNER, A. E. 2019. Marine Reservoir Age Variability Over the Last Deglaciation: Implications for Marine CarbonCycling and Prospects for Regional Radiocarbon Calibrations. *Paleoceanography and Paleoclimatology,* 34, 1807-1815.

ŚLUBOWSKA, M. A., KOÇ, N., RASMUSSEN, T. L. & KLITGAARD-KRISTENSEN, D. 2005. Changes in the flow of Atlantic water into the Arctic Ocean since the last deglaciation: Evidence from the northern Svalbard continental margin, 80°N. *Paleoceanography,* 20, n/a-n/a.

ŚLUBOWSKA-WOLDENGEN, M., RASMUSSEN, T. L., KOÇ, N., KLITGAARD-KRISTENSEN, D., NILSEN, F. & SOLHEIM, A. 2007. Advection of Atlantic Water to the western and northern Svalbard shelf since 17,500calyr BP. *Quaternary Science Reviews,* 26, 463-478.

SPIELHAGEN, R. F. & ERLENKEUSER, H. 1994. Stable oxygen and carbon isotopes in planktic foraminifers from Arctic Ocean surface sediments: Reflection of the low salinity surface water layer. *Marine Geology,* 119, 227-250.

STERN, J. V. & LISIECKI, L. E. 2013. North Atlantic circulation and reservoir age changes over the past 41,000 years. *Geophysical Research Letters,* 40, 3693-3697.

STØREN, E. N., DAHL, S. O., NESJE, A. & PAASCHE, Ø. 2010. Identifying the sedimentary imprint of high-frequency Holocene river floods in lake sediments: development and application of a new method. *Quaternary Science Reviews,* 29, 3021-3033.

SUNDFJORD, A., ASSMANN, K., LUNDESGAARD, Ø., RENNER, A. H. H., SIGRID, L. & INGVALDSEN, R. B. 2020. Suggested water mass definitions for the central and northern Barents Sea, and the adjacent Nansen Basin: Workshop Report. *The Nansen Legacy Report Series 8/2020.*

TALLEY, L. D. 2013. Closure of the global overturning circulation through the Indian, Pacific, and Southern Oceans: Schematics and transports. *Oceanography,* 26, 80-97.

THERMOFINNIGAN 2002. MAT253 Operating Manual. Germany.

THIAGARAJAN, N., SUBHAS, A. V., SOUTHON, J. R., EILER, J. M. & ADKINS, J. F. 2014. Abrupt pre-Bølling–Allerød warming and circulation changes in the deep ocean. *Nature,* 511, 75-78.

THOMSON, J., CROUDACE, I. W. & ROTHWELL, R. G. 2006. A geochemical application of the ITRAX scanner to a sediment core containing eastern Mediterranean sapropel units. *Geological Society, London, Special Publications,* 267, 65-77.

VAN DER BILT, W. G. M., CEDERSTRØM, J. M., STØREN, E. W. N., BERBEN, S. M. P. & RUTLEDAL, S. 2021. Rapid Tephra Identification in Geological Archives With Computed Tomography: Experimental Results and Natural Applications. *Frontiers in Earth Science,* 8.

WAGNER, T. & HERRLE, J. O. 2016. Carbon Isotopes. *In:* HARFF, J., MESCHEDE, M., PETERSEN, S. & THIEDE, J. (eds.) *Encyclopedia of Marine Geosciences.* Dordrecht: Springer Netherlands.

WALCZOWSKI, W. & PIECHURA, J. 2011. Influence of the West Spitsbergen Current on the local climate. *International Journal of Climatology,* 31**,** 1088-1093.

WANNER, H., MERCOLLI, L., GROSJEAN, M. & RITZ, S. P. 2015. Holocene climate variability and change; a data-based review. *Journal of the Geological Society,* 172**,** 254-263.

WERNER, R. A. & BRAND, W. A. 2001. Referencing strategies and techniques in stable isotope ratio analysis. *Rapid Communications in Mass Spectrometry,* 15**,** 501-519.

WHITE, W. M. 2013. *Geochemistry,* Chichester, Wiley-Blackwell.

WOLLENBURG, J. E. & MACKENSEN, A. 1998. Living benthic foraminifers from the central Arctic Ocean: faunal composition, standing stock and diversity. *Marine Micropaleontology,* 34**,** 153-185.

YU, J., ELDERFIELD, H. & PIOTROWSKI, A. M. 2008. Seawater carbonate ion-δ13C systematics and application to glacial–interglacial North Atlantic ocean circulation. *Earth and Planetary Science Letters,* 271**,** 209-220.

ZHANG, R. & THOMAS, M. 2021. Horizontal circulation across density surfaces contributes substantially to the long-term mean northern Atlantic Meridional Overturning Circulation. *Communications Earth & Environment,* 2.

Appendices

Appendix A: Stable isotope data

Appendix B: Statistics

Appendix C: XRF based calcium and strontium data

Appendix D: Pilot Mg/Ca analysis

Appendix A: Stable isotope data

Table A.1 *N. pachyderma*: δ^{18}O and δ^{13}C

Depth (cm)	δ^{18}O	δ^{18}O repeat	δ^{18}O average	δ^{13}C	δ^{13}C repeat	δ^{13}C average
400	4,016	4,006	4,011	0,131	0,103	0,117
402	4,236	4,390	4,313	-0,098	0,132	0,017
404	3,972		3,972	0,091		0,091
406	4,164	4,017	4,091	0,133	-0,206	-0,037
408	4,160	4,421	4,291	0,002	0,274	0,138
410	4,420	4,169	4,294	0,189	-0,005	0,092
412	3,924	4,074	3,999	-0,124	0,161	0,019
414	4,122		4,122	-0,006		-0,006
416	3,830	4,046	3,938	-0,176	-0,074	-0,125
418	4,185	4,697	4,441	0,040	0,125	0,083
420	4,116		4,116	-0,005		-0,005
422	4,333	4,113	4,223	0,085	0,053	0,069
424	4,374	4,173	4,273	-0,205	-0,012	-0,109
426	3,938	3,860	3,899	-0,088	0,022	-0,033
428	3,987		3,987	-0,014		-0,014
430	4,111	4,064	4,087	-0,021	-0,087	-0,054
432	4,131	4,155	4,143	-0,037	0,093	0,028
434	4,150	4,097	4,123	0,011	0,197	0,104
436	4,122	4,223	4,173	0,089	0,038	0,064
438	3,950	4,546	4,248	0,048	0,075	0,062
440	3,945	3,875	3,910	-0,097	-0,232	-0,165
441	3,943	3,771	3,857	0,022	-0,117	-0,048
442	3,583		3,583	-0,194		-0,194
443	3,948		3,948	-0,128		-0,128
444	4,053	4,110	4,082	-0,143	0,095	-0,024
445	4,436	4,343	4,390	-0,086	-0,022	-0,054
446	3,907		3,907	0,058		0,058
447	4,349		4,349	0,108		0,108
448	3,818	3,763	3,790	-0,130	-0,087	-0,109
449	3,706		3,706	0,083		0,083
450	3,672		3,672	0,020		0,020
451	3,643		3,643	0,030		0,030
452	3,897		3,897	-0,022		-0,022
453	3,881		3,881	-0,194		-0,194
454	3,703		3,703	0,027		0,027

455	3,722		3,722	-0,145		-0,145
456	3,905	3,828	3,866	-0,161	0,008	-0,077
457	3,782		3,782	0,186		0,186
458	3,989		3,989	-0,022		-0,022
459	3,742	3,489	3,615	-0,030	-0,093	-0,062
460	3,589		3,589	0,105		0,105
461	3,612		3,612	-0,023		-0,023
462	3,750		3,750	0,012		0,012
463	3,831		3,831	-0,164		-0,164
464	3,501		3,501	0,122		0,122
465	3,886		3,886	0,019		0,019
466	3,653		3,653	-0,086		-0,086
467	3,656		3,656	-0,121		-0,121
468	3,669		3,669	-0,158		-0,158
469	3,855		3,855	0,113		0,113
471	3,871		3,871	0,076		0,076
472	3,727	2,994	3,361	-0,418	-0,332	-0,375
473	4,147		4,147	-0,204		-0,204
474	4,142		4,142	0,041		0,041
475	4,012		4,012	-0,118		-0,118
476	4,036		4,036	-0,293		-0,293
477	3,789		3,789	-0,060		-0,060
478	2,878		2,878	-0,037		-0,037
480	2,962	3,088	3,025	-0,029	-0,126	-0,078
481	3,151		3,151	0,223		0,223
482	3,271		3,271	0,073		0,073
483	2,972		2,972	0,069		0,069
484	3,409		3,409	0,093		0,093
485	3,134	3,090	3,112	0,074	0,100	0,087
486	3,115		3,115	0,019		0,019
487	2,751		2,751	0,061		0,061
488	2,851	2,898	2,875	-0,021	-0,040	-0,031
489	2,640	2,892	2,766	-0,072	0,148	0,038
490	2,955		2,955	-0,040		-0,040
491	2,888		2,888	0,026		0,026
492	3,059		3,059	0,020		0,020
493	2,981		2,981	-0,037		-0,037
494	2,676		2,676	-0,020		-0,020
495	3,473		3,473	0,124		0,124
496	2,639	2,971	2,805	-0,120	-0,027	-0,074
497	3,062		3,062	0,114		0,114

498	2,805	3,198	3,001	0,058	0,206	0,132
499	3,280		3,280	0,041		0,041
500	3,080		3,080	0,030		0,030
506	4,236	4,495	4,366	-0,136	0,274	0,069
507	4,390		4,390	-0,057		-0,057
508	4,055		4,055	0,082		0,082
509	3,730		3,730	-0,041		-0,041
510	4,584		4,584	0,177		0,177
511	3,980	3,868	3,924	0,010	-0,200	-0,095
512	3,888	3,965	3,927	-0,346	-0,131	-0,239
513	3,771		3,771	0,038		0,038
514	3,853	3,497	3,675	0,001	-0,325	-0,162
515	4,166		4,166	0,052		0,052
516	3,719		3,719	0,006		0,006
517	3,828		3,828	-0,106		-0,106
518	3,870		3,870	0,066		0,066
519	3,738	3,917	3,827	-0,051	-0,056	-0,054
520	3,747	3,799	3,773	-0,169	-0,078	-0,124
522	3,823		3,823	-0,051		-0,051
524	3,878		3,878	0,012		0,012
526	3,951	4,066	4,008	-0,096	0,034	-0,031
528	3,842	3,845	3,843	0,094	-0,050	0,022
530	3,599	3,656	3,627	-0,353	-0,102	-0,228
532	3,883		3,883	-0,137		-0,137
534	3,867	3,864	3,866	-0,109	-0,132	-0,121
536	4,174	4,077	4,125	-0,071	-0,074	-0,073
540	4,209		4,209	0,136		0,136
542	3,905	3,781	3,843	0,034	-0,212	-0,089
544	3,988	3,848	3,918	-0,134	-0,171	-0,153
546	3,965		3,965	0,019		0,019
548	3,884		3,884	-0,170		-0,170
550	3,926	3,922	3,924	0,135	-0,036	0,050

*The depths for which no isotope data was obtained due to the absence of foraminifera have been removed.

Table A.2 *C. neoteretis*: δ^{18}O and δ^{13}C

Depth (cm)	δ^{18}O	δ^{18}O repeat	δ^{18}O average	δ^{13}C	δ^{13}C repeat	δ^{13}C average
400	4,955		4,955	-0,413		-0,413
404	4,923		4,923	-0,653		-0,653
406	4,414		4,414	-0,812		-0,812
408	5,168		5,168	-0,639		-0,639
410	4,935	5,098	5,016	-0,782	-0,635	-0,709
412	4,706	4,633	4,670	-0,776	-0,910	-0,843
414	4,769	4,804	4,787	-0,673	-0,756	-0,715
416	4,641		4,641	-0,827		-0,827
418	5,818	5,804	5,811	-0,976	-0,814	-0,895
420	5,316	5,154	5,235	-1,033	-1,035	-1,034
422	5,071		5,071	-0,763		-0,763
424	5,160		5,160	-0,610		-0,610
426	4,493		4,493	-0,829		-0,829
428	4,944		4,944	-0,890		-0,890
430	5,112		5,112	-0,860		-0,860
434	5,190		5,190	-0,722		-0,722
436	5,220	5,346	5,283	-0,672	-0,704	-0,688
438	4,767	4,601	4,684	-0,870	-0,888	-0,879
440	4,610		4,610	-0,775		-0,775
441	4,458		4,458	-0,871		-0,871
444	4,985		4,985	-0,798		-0,798
445	5,321		5,321	-0,788		-0,788
446	4,364		4,364	-0,727		-0,727
449	4,520		4,520	-0,778		-0,778
450	4,253		4,253	-0,788		-0,788
451	4,775		4,775	-0,784		-0,784
452	4,440		4,440	-0,900		-0,900
453	4,712		4,712	-1,009		-1,009
454	4,229		4,229	-0,890		-0,890
455	4,386	4,391	4,388	-1,030	-1,065	-1,048
457	4,559		4,559	-0,798		-0,798
458	4,932		4,932	-0,900		-0,900
459	4,251	4,352	4,302	-0,965	-0,922	-0,944
460	4,360		4,360	-0,910		-0,910
461	4,536		4,536	-1,011		-1,011
462	5,116		5,116	-0,749		-0,749

463	4,666		4,666	-0,870		-0,870
464	4,325		4,325	-0,966		-0,966
465	5,325	4,729	5,027	-0,754	-0,855	-0,805
466	4,615		4,615	-0,992		-0,992
467	4,598		4,598	-0,899		-0,899
468	4,645		4,645	-0,837		-0,837
469	4,601		4,601	-0,810		-0,810
470	4,976		4,976	-0,771		-0,771
471	4,854		4,854	-0,812		-0,812
472	4,591		4,591	-0,857		-0,857
473	5,063	4,534	4,798	-0,648	-0,712	-0,680
474	5,051		5,051	-0,691		-0,691
475	4,951		4,951	-0,807		-0,807
476	4,812		4,812	-0,874		-0,874
477	4,448	4,375	4,411	-0,711	-0,940	-0,826
478	4,191		4,191	-0,734		-0,734
479	4,377		4,377	-1,016		-1,016
480	3,806		3,806	-0,560		-0,560
481	3,917	3,733	3,825	-0,341	-0,420	-0,381
482	3,516		3,516	-0,254		-0,254
483	3,716		3,716	-0,323		-0,323
484	4,028		4,028	-0,114		-0,114
485	3,907	3,572	3,740	-0,305	-0,151	-0,228
486	3,475	3,630	3,553	-0,367	-0,402	-0,385
487	3,544		3,544	-0,298		-0,298
488	3,572	3,543	3,558	-0,128	-0,213	-0,171
489	3,473	3,293	3,383	-0,200	-0,374	-0,287
490	3,660		3,660	-0,281		-0,281
491	3,403		3,403	-0,417		-0,417
492	3,697	3,685	3,691	-0,286	-0,329	-0,308
493	3,482		3,482	-0,394		-0,394
494	3,359	3,285	3,322	-0,319	-0,543	-0,431
495	3,741		3,741	-0,265		-0,265
496	4,486	3,510	3,998	-0,312	-0,340	-0,326
497	3,905		3,905	-0,424		-0,424
498	3,653	3,077	3,365	-0,236	-1,281	-0,236
500	4,468		4,468	-0,610		-0,610
506	5,399		5,399	-0,457		-0,457
507	4,879		4,879	-0,570		-0,570
508	4,874		4,874	-0,604		-0,604
509	4,699		4,699	-0,730		-0,730

511	4,199	4,665	4,432	-0,702	-0,770	-0,736
512	4,319		4,319	-0,822		-0,822
513	4,754		4,754	-0,577		-0,577
514	4,465		4,465	-0,859		-0,859
518	4,676		4,676	-0,747		-0,747
519	4,499	4,487	4,493	-0,706	-0,687	-0,697
520	4,389		4,389	-0,862		-0,862
522	4,714		4,714	-0,589		-0,589
524	4,995		4,995	-0,961		-0,961
526	4,737		4,737	-0,771		-0,771
530	4,434	4,437	4,436	-0,832	-0,744	-0,788
532	4,560		4,560	-0,389		-0,389
534	4,661	4,690	4,675	-0,457	-0,502	-0,480
536	5,285		5,285	-0,221		-0,221
540	4,887		4,887	-0,695		-0,695
542	4,626	4,701	4,663	-0,952	-0,766	-0,859
544	4,860		4,860	-0,580		-0,580
546	4,670		4,670	-0,657		-0,657
548	4,874		4,874	-0,795		-0,795
550	4,556	4,552	4,554	-0,870	-0,893	-0,882

*Depths at which no isotope data was obtained have been left out. The red value is an outlier and has been excluded in SD calculations.

Table A.3 *N. labradorica*: δ^{18}O and δ^{13}C

Depth (cm)	δ^{18}O	δ^{18}O repeat	δ^{18}O average	δ^{13}C	δ^{13}C repeat	δ^{13}C average
400	4,929		4,929	-1,242		-1,242
402	5,686		5,686	-1,163		-1,163
404	4,930	4,950	4,940	-1,150	-1,009	-1,080
406	5,043	5,119	5,081	-1,118	-0,989	-1,054
408	4,773		4,773	-1,523		-1,523
410	4,821	4,912	4,867	-2,058	-1,667	-1,863
418	4,825		4,825	-2,331		-2,331
422	4,755	4,820	4,788	-2,720	-2,017	-2,369
428	4,992	4,857	4,925	-1,598	-1,998	-1,798
434	4,663	4,645	4,654	-1,408	-1,435	-1,422
436	4,816	6,518	4,816	-1,515	-1,237	-1,376
438	4,817	4,688	4,752	-1,602	-1,690	-1,646
440	4,580		4,580	-1,837		-1,837
441	4,532		4,532	-1,726		-1,726
442	4,630	4,385	4,508	-1,729	-1,522	-1,626
443	4,460	4,447	4,454	-1,683	-2,084	-1,884
444	4,573	4,616	4,594	-1,323	-1,681	-1,502
445	4,447	4,534	4,490	-1,865	-1,584	-1,725
446	4,731	4,656	4,694	-1,841	-1,619	-1,730
447	4,541		4,541	-1,308		-1,308
448	4,614		4,614	-1,205		-1,205
449	4,450		4,450	-1,445		-1,445
450	4,727		4,727	-1,617		-1,617
451	4,568	4,478	4,523	-1,554	-2,312	-1,933
452	4,602		4,602	-1,378		-1,378
453	4,770		4,770	-1,490		-1,490
454	4,461	4,439	4,450	-2,003	-1,876	-1,940
455	4,467	4,397	4,432	-2,027	-2,124	-2,076
456	4,185		4,185	-1,786		-1,786
457	4,481		4,481	-1,652		-1,652
458	4,513		4,513	-1,791		-1,791
459	4,380	4,491	4,435	-1,382	-1,358	-1,370
460	4,343		4,343	-1,887		-1,887
461	4,347		4,347	-1,796		-1,796
462	4,697		4,697	-1,830		-1,830
463	4,507		4,507	-1,911		-1,911

464	4,487	4,269	4,378	-1,781	-1,498	-1,640
465	3,923	4,573	4,248	-2,080	-1,666	-1,873
466	4,724		4,724	-2,070		-2,070
467	4,773		4,773	-2,080		-2,080
468	4,790		4,790	-2,067		-2,067
469	4,774	4,893	4,833	-1,433	-1,446	-1,440
470	4,715		4,715	-1,854		-1,854
471	4,625		4,625	-1,823		-1,823
472	4,823	4,670	4,747	-1,613	-1,633	-1,623
473	4,623	4,279	4,451	-1,410	-1,307	-1,359
474	5,046		5,046	-1,199		-1,199
475	4,902		4,902	-1,262		-1,262
476	5,162		5,162	-0,708		-0,708
477	4,201	4,521	4,361	-0,917	-0,861	-0,889
478	4,346		4,346	-0,539		-0,539
479	4,110		4,110	-0,547		-0,547
480	4,235		4,235	-0,763		-0,763
481	4,145	4,216	4,180	-0,650	-0,676	-0,663
482	4,214		4,214	-0,952		-0,952
484	4,558		4,558	-0,715		-0,715
487	4,201		4,201	-0,850		-0,850
524	4,975		4,975	-1,367		-1,367
526	5,135		5,135	-1,277		-1,277
528	4,763		4,763	-1,521		-1,521
530	4,867		4,867	-1,487		-1,487
532	4,600		4,600	-1,343		-1,343
534	4,613		4,613	-1,671		-1,671
540	4,508		4,508	-0,928		-0,928
542	4,553	4,553	4,553	-0,862	-1,264	-1,063
544	4,672		4,672	-0,997		-0,997
546	4,668		4,668	-1,416		-1,416
548	4,784		4,784	-1,328		-1,328
550	4,647	4,655	4,651	-1,271	-1,205	-1,238

*Depths for which no isotope data was obtained have been left out. *N.labradorica* is absent for the interval of 488 and 523 cm. The red value is an outlier and has been excluded in the SD calculations.

Appendix B: Statistics

To evaluate the reliability of the trends seen in the stable isotope records the standard deviation needed to be calculated. The standard deviation for each species was calculated using the Equation B.1:

The mean value of the replicates at each depth interval

Value of single measurement at each depth interval

$$STD = \sqrt{\frac{\sum(\bar{x} - x)^2}{n - k}}$$

Total number of replicates

Number of depth intervals with replicates

Equation B.1

The n and k value change for each species depending on the number of replicates that were done for that species and the number of depth intervals of these replicates.

Table B.1 The n and k values used for calculating SD.

N. pachyderma		*C. neoteretis*		*N. labradorica*	
$\delta^{18}O$	$\delta^{13}C$	$\delta^{18}O$	$\delta^{13}C$	$\delta^{18}O$	$\delta^{13}C$
n = 88	n = 88	n = 54	n = 52	n = 50	n = 52
k = 44	k = 44	k = 27	k = 26	k = 25	k = 26

The standard error of the mean (SEM) is used when a statistic is for a sample mean. ‘n’ is equal to the number of replicates at each depth, which in this thesis is 2. As replicates increase, SEM decreases. SEM was calculated using the Equation B.2 where:

$$\mathrm{SEM} = \frac{STD}{\sqrt{n}}$$

Equation B.2

Appendix C: XRF based calcium and strontium data

Calcium (Ca) found in the sediment can be associated with biogenic or terrestrial sediment sources (e.g., limestones and clays). Strontium (Sr) is a useful biogenic marker as foraminifera often fix Sr at the same time as Ca (Rothwell and Croudace, 2015). The co-variation of Ca and Sr therefore indicates the biogenic origin of Ca.

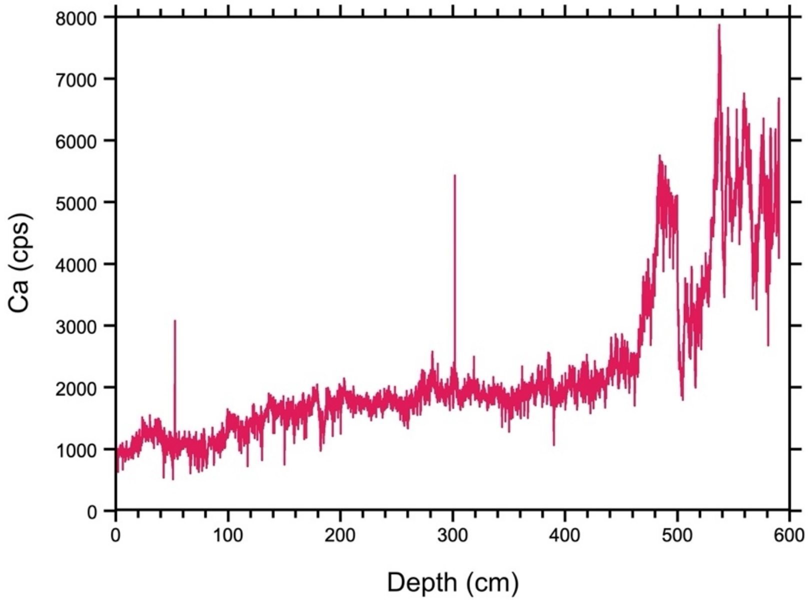

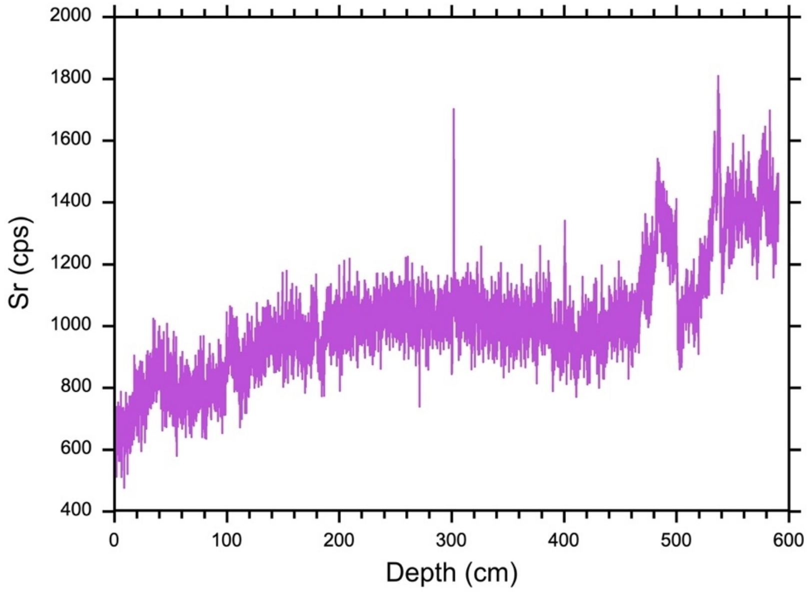

Figure C.1 XRF profiles of calcium (Ca) (top) and strontium (Sr) (bottom) indicating the co-variation of these two elements.

Appendix D: Pilot Mg/Ca analysis

After foraminifera had been picked and run for stable isotope analysis, I repicked 18 interesting depth intervals chosen based on the stable isotope results and that had enough material to do a pilot Mg/Ca work. *N. pachyderma* was picked from a size fraction of 150 – 250 μm and *C. neoteretis* and *N. labradorica* were picked from all size fractions above 150 μm. A total of 33 samples with weights ranging between 87 to 525 μg were sent to the University of Southampton (National Oceanography Centre Southampton lab) for Mg/Ca analysis. The foraminiferal tests were gently crushed to facilitate chemical treatment, and visible infilled siliciclastic material was removed when possible. Before the analysis, samples were cleaned following the clay removal, reductive, oxidative and final acid leaching step (Rosenthal et al., 1997). The foraminiferal tests were gently crushed to facilitate chemical treatment, and visible infilled siliciclastic material was removed when possible. Trace element analyses was done on a Thermo Scientific Element XR Sector Field Inductively Coupled Plasma Mass Spectrometer (SF-ICP-MS) at the National Oceanography Centre Southampton. The low Al/Ca and no observable correlation between Mn, Fe, Zn with Mg/Ca indicate that there was little contamination. The long-term uncertainty for Mg/Ca at the National Oceanography Centre Southampton lab is 2%.

Table D.1 Depths picked for Mg/Ca analysis and the Mg/Ca ratios obtain for these depths

ICP ID	**Species**	**Depth (cm)**	**Mg/Ca**
KH18 10 14 GC1 Cneo454	*C.neoteretis*	454	1,45
KH18 10 14 GC1 Cneo467	*C.neoteretis*	467	1,27
KH18 10 14 GC1 Cneo470	*C.neoteretis*	470	1,30
KH18 10 14 GC1 Cneo473	*C.neoteretis*	473	1,11
KH18 10 14 GC1 Cneo481	*C.neoteretis*	481	1,11
KH18 10 14 GC1 Cneo486	*C.neoteretis*	486	1,14
KH18 10 14 GC1 Cneo489	*C.neoteretis*	489	1,17
KH18 10 14 GC1 Cneo492	*C.neoteretis*	492	1,04
KH18 10 14 GC1 Cneo494	*C.neoteretis*	494	1,12
KH18 10 14 GC1 Cneo506	*C.neoteretis*	506	0,98
KH18 10 14 GC1 Cneo508	*C.neoteretis*	508	1,11
KH18 10 14 GC1 Cneo511	*C.neoteretis*	511	1,29
KH18 10 14 GC1 Cneo526	*C.neoteretis*	526	1,95
KH18 10 14 GC1 Cneo534	*C.neoteretis*	534	1,15
KH18 10 14 GC1 Nlab454	*N.labradorica*	454	1,71

KH18_10_14_GC1_Nlab467	*N.labradorica*	467	1,69
KH18_10_14_GC1_Nlab470	*N.labradorica*	470	1,98
KH18_10_14_GC1_Nlab481	*N.labradorica*	481	1,81
KH18_10_14_GC1_Nlab530	*N.labradorica*	530	2,01
KH18_10_14_GC1_Nlab540	*N.labradorica*	540	1,95
KH18_10_14_GC1_Nlab542	*N.labradorica*	542	1,78
KH18_10_14_GC1_NPS449&450	*N.pachyderma*	449	1,05
KH18_10_14_GC1_NPS454	*N.pachyderma*	454	1,03
KH18_10_14_GC1_NPS481	*N.pachyderma*	481	0,99
KH18_10_14_GC1_NPS486	*N.pachyderma*	486	0,98
KH18_10_14_GC1_NPS489	*N.pachyderma*	489	0,81
KH18_10_14_GC1_NPS492	*N.pachyderma*	492	0,96
KH18_10_14_GC1_NPS494	*N.pachyderma*	494	1,06
KH18_10_14_GC1_NPS506	*N.pachyderma*	506	0,73
KH18_10_14_GC1_NPS508	*N.pachyderma*	508	0,82
KH18_10_14_GC1_NPS511	*N.pachyderma*	511	0,78
KH18_10_14_GC1_NPS526	*N.pachyderma*	526	0,82
KH18_10_14_GC1_NPS534	*N.pachyderma*	534	0,81

The Mg/Ca ratio of foraminifera is a useful palaeoceanographic proxy due to the positive relationship between magnesium content of $CaCO_3$ shells and the temperature at which they grew in (Chave, 1954; Nuernberg, 1995). As can be seen in figures D.1, D.2 and D.3 below, the Mg/Ca and related temperature data obtained for the interval of focus in this thesis do not show any meaningful trend for *N. pachyderma* or *C. neoteretis*. Additionally, the lack of material for *N.labradorica* means that Mg/Ca data was not obtained for most of the YD interval for this species. The variability observed in all four temperature calibrations for *N. pachyderma* is not greater than the difference between the calibrations, indicating a large calibration error (figure D.2).

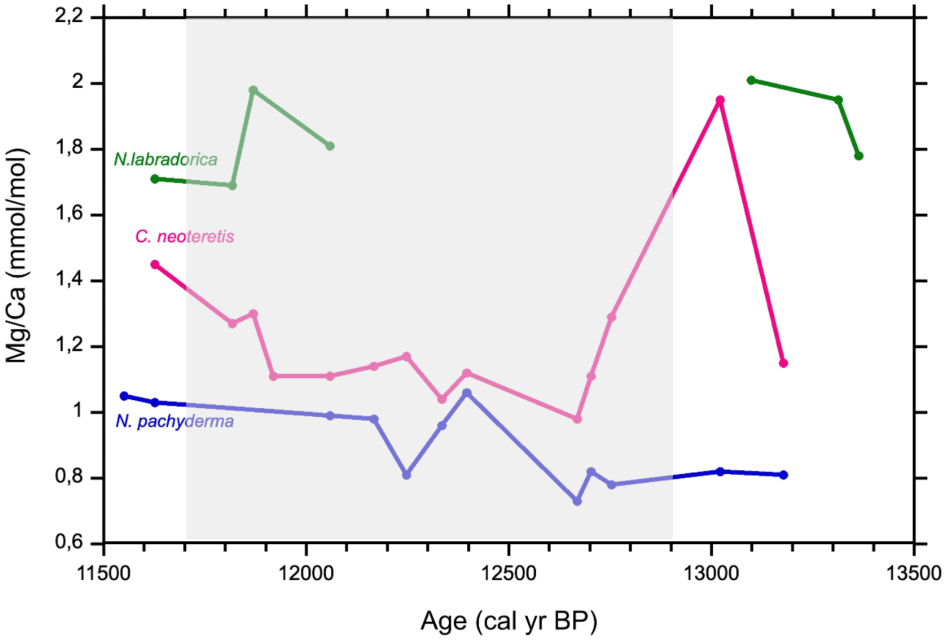

Figure D.1 Mg/Ca (mmol/mol) of *N.pachyderma*, *C.neoteretis* and *N.labradorica*. The YD is highlighted in grey.

Table D.2 Equations used to obtain surface (*N. pachyderma*) and bottom (*C. neoteretis*) water temperatures from the Mg/Ca values.

Reference	**Equation**	**Temperature range**
N. pachyderma		
(Kozdon et al., 2009)	Mg/Ca = 0.13 * T + 0.35	3 – 6 °C
(Nuernberg, 1995)	Mg/Ca = 0.41 * e(0.083 *T)	0 – 15 °C
(Livsey et al., 2020)	Mg/Ca = 0.93 * e(0.086 * T)	-2 – 12 °C
(Davis et al., 2017)	Mg/Ca = 0.71*T-2.49	6 – 12 °C
C. neoteretis		
(Kristjánsdóttir et al., 2007)	Mg/Ca = 0.864 *e(0.082* T)	1 – 6 °C
(Barrientos et al., 2018)	Mg/Ca = 1.009 *e(0.042*T)	0 – 6 °C
(Sessford et al., 2018)	Mg/Ca = 0.832 *e(0.091*T)	-2 – 6 °C

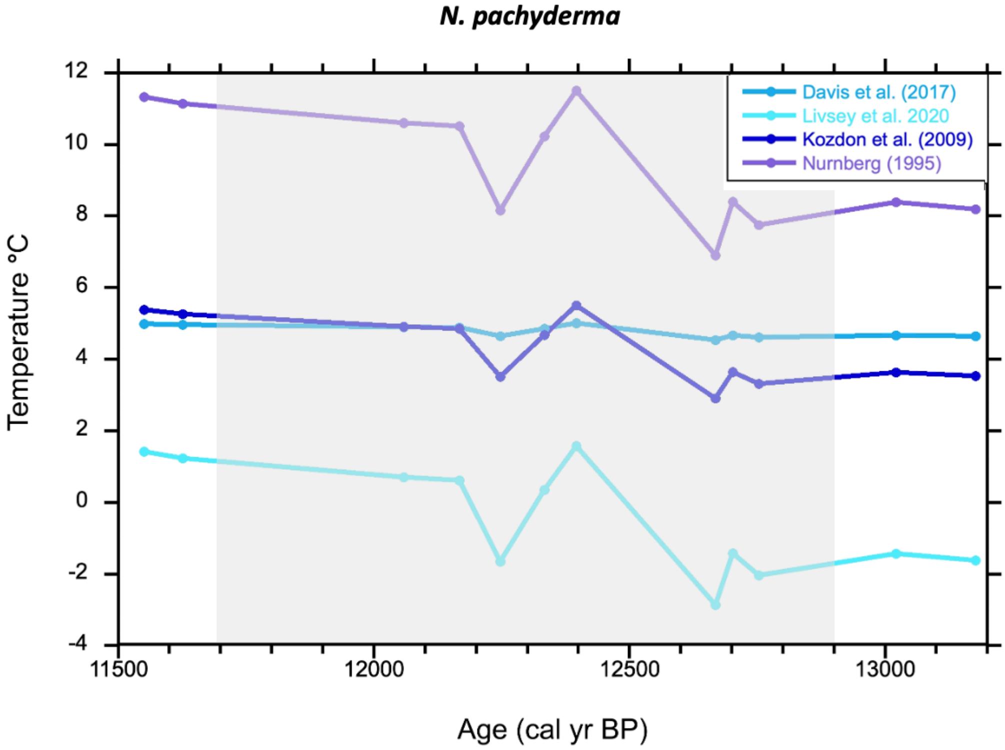

Figure D.2 Water temperatures calibrated from *N.pachyderma* Mg/Ca values using four different calibration equations. The YD is highlighted in grey.

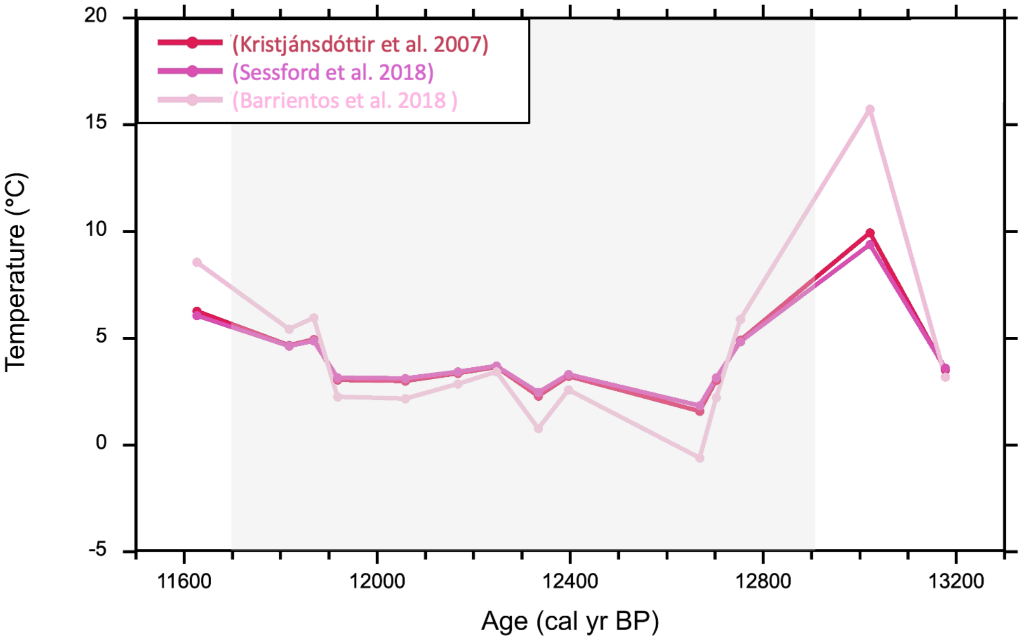

Figure D.3 Bottom water temperatures calibrated from Mg/Ca of *C. neoteretis* using three different calibration equations. The YD is highlighted in grey.

The bottom water temperatures (BWT) obtained for *C. neoteretis* (figure D.3) display an unrealistically high peak of between 10 – 15 ℃ prior to the YD followed by a rapid decrease until 12 700 cal yr BP. This peak only consists of one data point and could therefore be an outlier. For the remainder of the YD, BWTs vary slightly but do not show any significant trend. The discordance between the benthic and planktic Mg/Ca trends (figure D.1) is unexpected as these three species displayed similar trends in δ^{18}O during the YD and were likely affected by the same water mass. The lack of temperature signal seen in the Mg/Ca data compared to the δ^{18}O data was expected as foraminiferal Mg/Ca incorporation is not as sensitive at low temperatures (figure D.4) (Kozdon et al., 2009). This means that a large change in temperature at the colder end of the calibration scale could have resulted only in a small change in Mg/Ca. Due to the low sensitivity of this proxy at low temperatures, this data has not been included in this Master thesis.

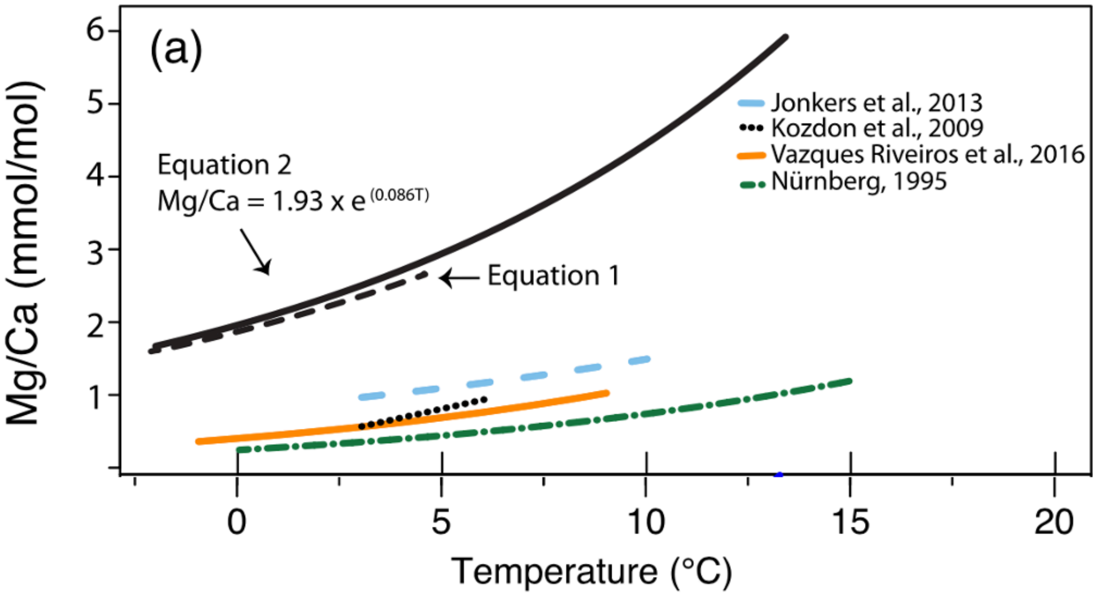

Figure D.4 Figure showing 6 different temperature calibration equations for Mg/Ca. The curve displays that there is lower sensitivity of Mg/Ca at lower temperatures (Livsey et al., 2020)